SAPIENZA
UNIVERSITÀ DI ROMA

Aging Investigations of Laponite Systems

Dottorato di Ricerca in Fisica – XXV Ciclo

Candidate

Flavio Augusto de Melo Marques
ID number 1184056

Thesis Advisors

Dr. Barbara Ruzicka
Prof. Giancarlo Ruocco

A thesis submitted in partial fulfillment of the requirements
for the degree of Doctor of Philosophy in Physics

December 2012

Thesis defended on 7 February 2013
in front of a Board of Examiners composed by:

Prof. Claudio Castellani (chairman)

Prof. Sergio Caracciolo

Prof. Maurizio Sasso

Flavio Augusto de Melo Marques. *Aging Investigations of Laponite Systems.*
Ph.D. thesis. Sapienza – University of Rome

EMAIL: flaviofisica@gmail.com

Acknowledgments

I would like to express my sincere gratitude to Barbara Ruzicka who patiently and expertly guided me during this PhD. I am really honored to have the opportunity to study with her group together with such experienced researchers.

I would like to extend my gratefully acknowledge to Giancarlo Ruocco for his experienced supervision and support throughout my PhD.

My truthful thank to Roberta Angelini for her effective advice in this project. I also wish to thank Bela Farago and Beatrice Ruta for their fruitful discussions and collaboration during Neutron Spin Echo and X-ray Photon Correlation Spectroscopy experiments in Grenoble.

I would also like to thank Silvia De Sio and Laura Zulian for their contribution to my scientific knowledge. And also to all the past and current office mates for their companionship throughout my PhD.

To my parents, Manuel and Cristina, for their never-ending support and incentive who provided me a harmonious and healthy life fundamental for the successful completion of this project. To my brother Claudio for all the smart discussions about science and technology. To my wife, Valeria, my daily source of strength and love who accompanied me during this PhD.

Lastly, to the Foreign Nationals Educated Abroad (FNEA) program of the University of Rome to provide me the scholarship.

Contents

Chapter 1

Introduction

1.1 Colloids

The term *colloid* was coined by Thomas Graham in the 19^{th} century. Graham attempted to distinguish materials in aqueous solution just taking into account particles that pass or not through a membrane. Glue was a material stopped from the membrane, and then its Greek name "$\kappa o\lambda\lambda\alpha$" was used for colloid, that do not diffuse though a membrane, because the dissolved species are too large to pass the pores. Before Graham, in the 1820's, the botanist Robert Brown observed irregular motions of pollen grains, that have colloidal size, in water. This motion, today referred as Brownian motion, is the result of random collisions of solvent molecules with the colloidal particles.

The simplest definition of a colloidal dispersion is that of a system composed by two separated phases, where particles with colloidal size (1 nm up to 1 μm) of any nature (*e.g.* solid, liquid or gas) are dispersed in a continuous phase of a different composition (or state) [1].

The dispersed particles can be in a solid, liquid or gas state and are called particles, droplets and bubbles respectively. They can be dispersed in a solid, liquid or gas with exception of gas-gas because all gases are mutually miscible. Thus a liquid may be dispersed in a gas to form a liquid aerosol (*e.g.* fog and liquid sprays), in a solid to form a solid emulsion (*e.g.* opal and gelatin), or in another liquid to form an emulsion (*e.g.* homogenized milk, mayonnaise and crude oil). A solid may be dispersed in a gas to form a solid aerosol (*e.g.* smoke and dust), in a liquid to form a sol (*e.g.* pigmented ink and muddy water), or in another solid to form a solid sol (*e.g.* pigmented plastics and cranberry glass). Finally a gas may be dispersed in a liquid to form foam (*e.g.* beaten egg white and fire-extinguisher foam), or in a solid to form a solid foam (*e.g.* aerogel and pumice).

Most common colloidal dispersion is a *sol*, a dispersion of solid particles in a liquid solvent. They are found in a wide variety of systems such as blood, and play an important role in scientific research. An interesting characteristic of this system is that colloidal particles are always suspended inside the solvent. It happens mainly because of the diminute size of particles that are constantly bombarded by surrounding molecules of the medium. Because of the stochastic movement of the molecules in a liquid, colloidal particles perform random walk or Brownian motion.

The stability of the colloidal suspension can be destroyed by agglomeration. Generally, if two particles collide, they will stick together becoming a bigger particle, usually favored by energy. When it happens particles get larger than the critical size to be suspended by the bombardment of surrounding molecules and settle. This phenomenon is called sedimentation and is avoided by electric repulsion interactions due to electric charge of the same sign generally acquired by particles. In nature particles are charged mainly because they adsorb ions in the environment. For example, particles in aqueous dispersion can adsorb OH^- or H^+ ions generally present in water to become negatively or positively charged. Since most of the colloidal systems are made up of particles of the same type, they acquire the same charge sign and then repel each other avoiding coagulation.

The overwhelmingly important feature of colloids is that the dispersed particles have a large area-to-volume ratio. This makes the characteristic surface properties, at interfaces between the dispersed particles and solvent, to be strongly evident and to play a very important role in describing physical properties of the system as a whole. These characteristic surface properties can be of any nature, such as adsorption and electric double layer effects. In spite of this large area-to-volume ratio, some modifications in the interface and a significant molecular coverage of the dispersed particles may be reached with only small amount of material, and a strong modification of the whole bulk properties of a colloidal dispersion can be observed [2, 3]. For example, the addition of salt releases ions in the solution that completely modify the initial interaction potential between dispersed particles.

Nowadays colloidal systems have been widely exploited due to their interesting properties and large number of applications. The applicability of such systems can vary from medical-biological purposes to rheological modifiers. For example, lipid based colloids are generally used as drug delivery [4] and silica suspensions are used to the development of new materials with improving insulating properties [5].

Another important characteristic of colloids is that their typical dimensions and relaxation times make them experimentally more accessible respect to atomic or molecular liquids. Submicron particles sizes allows for the use of visible light source in experimental techniques such as microscopy and Dynamic and Static Light Scattering (DLS and SLS). It makes these techniques to be very powerful on the study of the dynamics and static properties of colloidal systems.

1.2 Clay as Colloidal Systems

The term clay is used to describe a group of silicate minerals that are composed by grains of diameter generally lower than 2 μm. The differences between clays and others small particles present in soils such as silt are smaller size of grains, presence of flake or layered shape and a large affinity of water that give rise to a characteristic plasticity. Despite of its use in bricks and ceramic, clays are widely used in several industrials applications such as paper making, chemical filtering and cement production.

Colloidal clays have recently emerged as complex model systems with a very rich phase diagram, encompassing fluid, gel and glassy states. Often these disordered states interfere with ordered ones, like nematic and columnar phases [6, 7]. However

most of natural clays have a large dispersion in size and shape, that makes their study difficult for large polidispersity. Between 1965 and 1970 the Laporte industries developed and introduced within international market a synthetic hectorite for industrial applications [8]. This product, called Laponite, is considered structurally identical to the natural hectorite-Na and have the same technological properties. There are many advantages of making synthetic clays such as low cost, reduced impurities and controlled physical properties of the particles (*e.g.* shape, size and charge). Thanks to the carefully controlled concentration rates of reagents and temperatures during the synthesis process, Laponite has a good size and shape polydispersion that makes possible its scientific research investigation [9].

Laponite in aqueous solvent forms a colloidal dispersion of discs with ∼25 nm of diameter and ∼1 nm of thickness with inhomogeneous charge distribution: a negative charge on the faces and a positive charge on the rims. Due to a competition between long range electric double layer repulsion and long range attraction, Laponite suspensions evolve towards different arrested states, that depend on the clay concentration C_w (weight concentration) and ionic strength of the medium I. These different arrested states originate an intriguing "phase" diagram that has been a focus of intense controversies in the past years [10, 11, 12, 13, 14]. However, recent works joining experiments, theory and simulations gave a large contribution to the understanding of the arrested structures [15, 16]. In salt free water (low ionic strength $I \sim 10^{-4}$ M) and high Laponite concentrations ($2.0\% \leq C_w < 3.0\%$) a complex arrested structure denominated Wigner glass is quickly reached (hours/days), characterized by repulsive interactions between the particles. For low Laponite concentrations ($1.0\% < C_w < 2.0\%$) aggregates of discs start to grow in a slow process (days/months) forming network structures mainly described by attractive forces. This structure is an equilibrium gel characteristic of "patchy" particles, *i.e.* particles with intrinsic anisotropy [15, 16, 17]. In both cases the evolution from an initial suspension of particles to the final arrested states is signaled by a strong increasing of the viscosity which describe an ergodic to non-ergodic transition. This process is denominated aging, characterized by a slowing down of the dynamics up to the formation of gel and glass arrested states. In this context Laponite has attracted the attention of the soft matter community for its complex phase diagram as well as for its possible technological applications.

To give further contributions to the understanding of charged colloidal suspensions we present in this work a detailed investigation of static and dynamic properties of several Laponite concentrations dispersed both in H_2O and D_2O. In particular the Q dependence of the aging dynamics has been addressed. Until now most of studies in Laponite systems have been performed in aqueous solvent by changing the ionic strength of the solution and clay concentration. In order to comprehend the effects of H/D isotopic substitutions in the physical properties of the system during aging we present in this work, for the first time, a complete and systematic investigation of static and dynamic properties of several Laponite concentrations dispersed in both H_2O and D_2O. This study has a crucial importance not only for the improvement on the understanding of Laponite systems but also to open the way for neutron scattering and nuclear magnetic resonance techniques that need the use of D_2O to gain contrast.

To accomplish this experimental work several conventional (light), synchrotron

radiation (X-ray) and neutron scattering techniques have been used to explore a very large Q and delay time ranges. In particular, a five angle dynamic light scattering setup has been developed and employed as main technique to follow the translational and rotational degrees of freedom during the aging of the system. To probe the system in a wider Q-range and slower delay times X-ray Photon Correlation Spectroscopy (XPCS) has been used. This technique permitted to investigate the slow dynamic properties of the system during the non-ergodic regime, not accessible by conventional DLS. To complement the dynamic study, Neutron Spin Echo (NSE) measurements were performed. Joining all these three techniques we could access a wide range of Q and delay-times which permitted to obtain dynamic informations in both ergodic and non-ergodic regimes in a wide length-scale, suitable for Laponite suspensions. Finally, the static properties of Laponite system in both H_2O and D_2O solvents have been followed by Small Angle X-ray Scattering (SAXS) during aging, up to the formation of arrested states for samples in both glass and gel regions and the possible effect of H/D isotopic substitutions in the arresting mechanisms has been studied.

1.3 Structure of the Thesis

- Chapter 2 presents the Laponite system and the main characteristics of a charged colloidal suspension. A description of Laponite and the formation of the charged disc-shaped colloidal suspension are described. The main interactions present in a charged suspension of particles and in particular the main theoretical models used to describe Laponite system are discussed. Sequentially the aging phenomenon and the different arrested states are introduced. Finally a description of the controversial Laponite phase diagram and the most recent picture of the arrested states are addressed.

- Chapter 3 describes the basic theory of light scattering experiments and the different scattering techniques used in this work. The main expressions necessary to understand correlation function measurements are introduced and the five angle DLS setup, developed and employed as main technique, is described together with its alignment procedure. The working mechanisms of XPCS and NSE techniques are briefly described and the general theory of static scattering is presented together with SAXS experiments. Finally the protocol for sample preparation is reported.

- Chapter 4 is dedicated to the discussion of the results obtained through the four aforementioned scattering techniques. The principal part regards DLS and DDLS results with a description of the data analysis procedure. The clay concentration (C_w), waiting time (t_w) and Q dependence of the relaxation parameters, for samples in a concentration range $1.5\% \leq C_w \leq 3.5\%$ in both H_2O and D_2O solvents, have been presented an discussed. Afterwards the relaxation times probed by XPCS and NSE have been studied as a function of Q and t_w. The joined results from all these techniques have been presented and permited to explore the waiting time behavior of the slow dynamics and the Q-dependence of the fast relaxation times in both ergodic and non-ergodic

regimes. Lastly the SAXS results for samples, both in H_2O and D_2O solvents, in the gel and glass states have been obtained elucidating that the picture of these two different arrested states, respectively at low and high concentrations, is preserved also for isotopic substitutions.

Chapter 2

Laponite Systems

In this work the dynamic and static properties of an anisotropic charged colloidal suspension in H_2O and D_2O solvents are investigated. The system used is a commercial synthetic clay, Laponite, deeply discussed in this chapter. The different interparticle interactions present in charged colloidal systems and more specifically in Laponite suspensions are described. The phenomenon of aging and the formation of different arrested states are introduced. Finally the evolution of the complex and controversial phase diagram of Laponite suspensions, presenting the most recent one are discussed.

2.1 Laponite Dispersions

Laponite is an entirely synthetic layered silicate developed by Laporte industries between 1965 and 1970 with a structure and composition closely resembling the natural clay mineral hectorite [8]. During the synthesis process, salts of sodium magnesium and lithium are combined with sodium silicate at well controlled rates and temperature. This process results an amorphous precipitate which is submitted to a high temperature treatment for a partial crystallization. The final product is then filtered, washed, dried and milled, having the appearance of a very fine white powder [18].

The crystalline structure of Laponite unit cell is composed by six octahedral magnesium ions sandwiched between two layers of four tetrahedral silicon atoms as shown in Fig. 2.1. These groups are balanced by twenty oxygen atoms and four hydroxyl groups. The idealized structure shown in Fig. 2.1 should be composed by six divalent magnesium ions (Mg^{++}) in the octahedral layer to give a positive charge of $+12\ e$, where e denotes the elementary charge. However, some magnesium ions are substituted by monovalent cations such as lithium (Li^{+}) and some positions are empty obtaining a negative charge of $-0.7\ e$ in the whole unit cell. During manufacturing process this negative charge is neutralized by the addition of sodium ions (Na^{+}) that adsorb onto the surfaces of the crystals. The sodium ions are shared by adjacent crystals that are consequently held together in form of stacks schematically shown (facing the rims) in Fig. 2.2 (a). The energy compensation originated by sodium ions is done according to the following molecular formula:

$$Na^{+}_{0.7}[(Si_8Mg_{5.5}Li_{0.3})O_{20}(OH)_4]^{-0.7}. \tag{2.1}$$

When dispersed in aqueous solvent the sodium ions release from the crystal interlayers (see Fig. 2.2 (b)), leading a homogeneous negative charge on the faces, while a protonation process of the hydroxide groups localized where the crystal structure terminates, originates a positive charge on the rim [19]. Therefore Laponite in aqueous solvent forms a colloidal dispersion of charged disc-like particles with a diameter of ∼25 nm and a thickness of ∼1 nm with negative and positive charges distributed on the faces and rims respectively [19]. The thickness of each Laponite disc corresponds to the height of the crystal unit cell shown in Fig. 2.1.

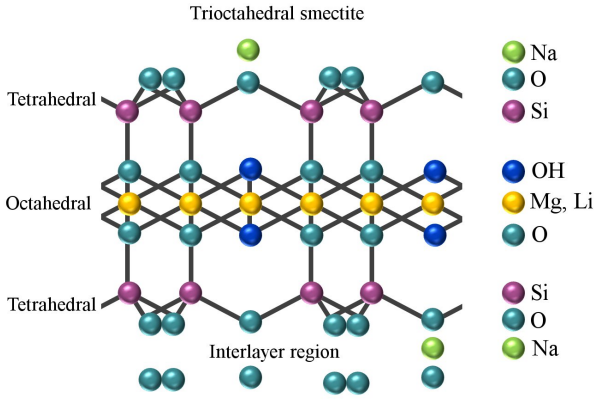

Figure 2.1. Idealized chemical structure of the unitary cell of Laponite (facing the rim). Six octahedral magnesium ions are sandwiched between two layers of four tetrahedral silicon atoms. The legend on the right displays the elements present in this structure [18].

The sodium counter-ions released in the system form a diffuse layer surrounding Laponite faces due to electrostatic attractions. It has been estimated that each crystalline unit cell shown in Fig. 2.1 is repeated around thousand times in two directions to form a single Laponite disc that is illustrated in Fig. 2.2 (c). The negative charges have been recently found by means of conductivity measurements to be lower than the nominal charge ($\sim -700\ e$), which is expected when all sodium ions are released from the particle surface [20]. On the other hand the positive charges present a pH dependence, showing a slow decreasing with increasing pH for pH $\lesssim$ 11 [19, 21]. It has been also suggested that for pH $\gtrsim$ 11 the positive charge can be neutralized [19]. However a systematic investigation done by Cummins has shown that independently if the sample has been prepared in water at fixed pH = 10, or if Laponite has been dispersed in deionized water without fixed pH, the final Laponite solution will always have a pH $\simeq$ 10 [22]. It means that under normal experimental conditions Laponite discs have positive charge on their rims.

Laponite dispersions are generally considered a monodisperse suspensions of discs shown in Fig. 2.2 (c). However Balnois and coauthors by using Atomic Force Microscopy in a very diluted deposition of Laponite solution on mica have found a small polydispersity both in radius and height [9]. Laponite particles appear as ellipses with height of $\sim$ 1 nm and both major and minor radius of 24.0 $\pm$ 6.9 nm

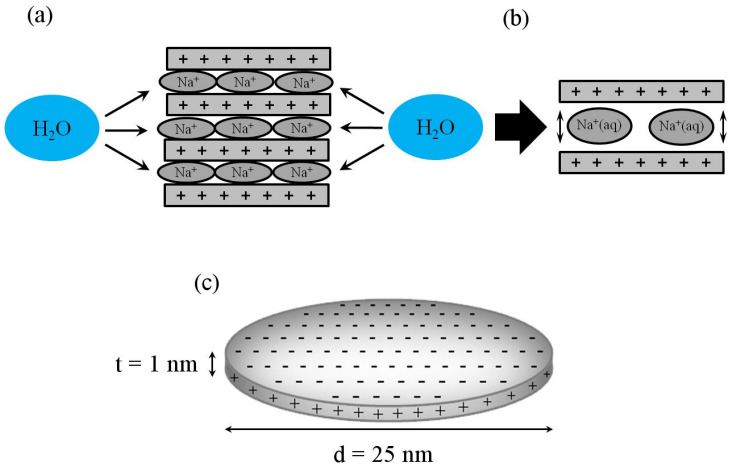

Figure 2.2. Sketch illustrating (a) the disposition of Laponite discs (facing the rim) in a dry configuration, (b) the hydration of the sodium ions and (c) the typical dimensions of single Laponite disc.

and 16.8 ± 4.9 nm respectively. Moreover they also reported that ∼ 20% of the particles on the mica surface were in a dimer configuration.

Laponite interaction potential is characterized by an isotropic van der Waals attraction and an anisotropic electrostatic interaction, which can be either repulsive (face-face, rim-rim) or attractive (rim-face). Since sodium counter-ions Na^+ are dispersed in the solution, the negative charged faces of the particles are screened by them forming an electrical double layer composed by a Stern and a diffuse layer. All these interactions will be discussed in the following section.

When Laponite is added to water a clear and colorless solution with low viscosity is formed. Nevertheless even for very low concentrations the solution evolves spontaneously with time towards a more viscous regime until it reaches an arrested state. This makes Laponite an ideal thickening agent to be used in several applications, such as surface coatings, ceramic glazes, paints, household cleaners and personal care products [18]. Several studies have elucidated the structure and the behavior of Laponite particles to reach the arrested states [10, 12, 13, 14]. The detailed phase diagram and the latest discoveries about Laponite systems will be shown and deeply explained in this thesis.

2.2 Interactions in Charged Colloidal Systems

2.2.1 Van der Waals Forces

The attractive forces between neutral and chemically saturated molecules was postulated by van der Waals to explain non-ideal gas behavior. The intermolecular attraction may act between two molecules with permanent dipole mutually oriented each other. It may also act between dipolar molecules and neutral molecules, in such a way that a dipole is induced in neutral molecules, and then an attraction is generated. Finally intermolecular interactions arises between non polar molecules, where polarization of one molecule is induced by fluctuations in the charge distribu-

tion in a second molecule, and vice versa. This last case is known as dispersion force, and it was explained by London in 1930. Apart of highly polar materials, London dispersion force is responsible by all of the van der Waals attraction that acts in a system and it is very short-ranged, since it has an inversely correspondence with the sixth power of the intermolecular distance.

For an assembly of molecules the dispersion forces are, to a first approximation, additive in such a way that interaction energy between two particles can be calculated by summing the attractions between all interparticle molecule pairs. Colloidal particles are large assemblies of atoms and hence the result of the sum predicts that the London interaction energy between a group of molecules decays much less rapidly than that between individual molecules. For example, the London dispersion interaction between two spherical particles of radii a_1 and a_2, separated in vacuum by a distance d, was first approximated by Hamaker in 1937 [23] and is given as follow:

$$\psi_{vdW} = -\frac{A}{12}\left[\frac{y}{x^2+xy+x} + \frac{y}{x^2+xy+x+y} + 2\ln\left(\frac{x^2+xy+x}{x^2+xy+x+y}\right)\right], \quad (2.2)$$

where

$$x = \frac{d}{a_1+a_2} \quad \text{and} \quad y = \frac{a_1}{a_2}. \quad (2.3)$$

For spheres with the same size, (*i.e.* $a_1 = a_2 = a$), we have $x = d/2a$, and then Eq. (2.2) becomes

$$\psi_{vdW}(x) = -\frac{A}{12}\left[\frac{1}{x(x+2)} + \frac{1}{(x+1)^2} + 2\ln\left(\frac{x(x+2)}{(x+1)^2}\right)\right]. \quad (2.4)$$

As we can see in Eq. (2.4) the attractive potential energy is directly proportional to a particle radius a, to a material constant (called Hamaker constant) A, and is inversely proportional to the distance separation d. The detailed calculation of Hamaker constants is a challenging task and for deep details see Refs. [24, 25]. However, for many practical purposes, the following equation estimated by Israelachvili [26] is enough:

$$A = \frac{3h\nu(n_1+n_2)^2(n_1-n_2)^2}{16\sqrt{2}(n_1^2+n_2^2)^{3/2}}, \quad (2.5)$$

where h is the Planck's constant, ν is a characteristic frequency and n_1 and n_2 are the optical refractive indices of the colloids and the solvent respectively. Therefore, by choosing a solvent with refractive index identical of the colloids ($n_1 = n_2$) one can suppress the van der Waals attraction.

In the limit of close-approach, the spheres are sufficiently large compared to the distance between them, *i.e.* ($d \ll 2a$), so that Eq. (2.4) reduces to a simple form:

$$\psi_{vdW} = -\frac{Aa}{12d}. \quad (2.6)$$

It means that if the particle approaches very close to each other it will lead to particle coagulation. In fact, the strong Born repulsions between electrons make the value of the van der Waals potential finite at contact, but still many times larger than the thermal energy k_BT, thus leading to an irreversible aggregation. Overlaps between colloidal particles are forbidden by Born repulsion what make the system to be usually modelled by a hard sphere potential for separations $r < 2a$, where r is the center-to-center distance.

2.2.2 Electric Double Layer Forces

When dispersed in a polar medium (principally in water) most substances acquire a surface electric charge. Possible charging mechanisms are ionization, ion adsorption and ion dissolution. In the case of Laponite dissociation of sodium ions adsorbed in between crystals layers (discs) are favored by the high dielectric constant ε of the medium, in such a way that the surface becomes charged with a $-\sigma$ net charge per unit area. On the other hand, sodium ions (Na^+) that have opposite charge compared to the Laponite faces are released into the solvent, which generally contains a finite concentration of anions and cations (microions). The final suspension is composed by negatively charged particles, ions of the same sign (co-ions) and ions of opposite sign (counter-ions).

The surface charge of the suspended particles influences the distribution of nearby ions in the polar medium in such a way that counter-ions are attracted towards the surface tending to screen the electrostatic potential, while co-ions are repelled away from the surface. This, together with the thermal motion of the microions, that tends to spread out or homogenize their distribution in order to increase their entropy, leads to the formation of an electric double layer, built up of the charged surface and a "cloud" of counter-ions as illustrated in Fig. 2.3.

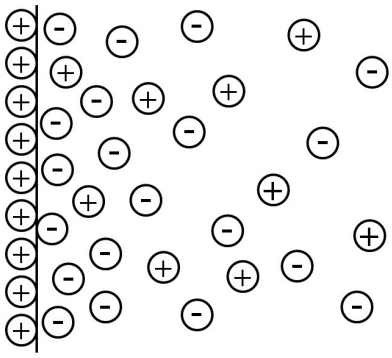

Figure 2.3. Schematic representation of a diffuse electric double layer.

The electric double layer can be considered composed of two regions: an inner region, which may include adsorbed ions in an area close to the actual interface, and a diffuse layer in which ions are subjected to the influence of electrical forces and random thermal motion. Ions in the inner region are supposed to be adsorbed strongly enough that they will not be displaced by thermal Brownian motion at least for a relatively long time.

This type of interaction represents one of the principal interaction of colloids and its quantitative treatment represents an extremely difficult and in some respects unresolved problem. Lets first start keeping our attention to a system composed only by the charged surface and the diffuse layer (see Fig. 2.3). The simplest quantitative treatment of this layer has been described by Gouy (1910) and Chapman (1913), where some important assumptions are considered and described in the following:

1. The surface is assumed to be uniformly charged, flat with infinite extension.
2. The ions involved, both on the surface and in solution, are assumed to be point charges.
3. The solvent is assumed to influence the double layer only through its dielectric constant that remains unchanged throughout the double layer.
4. The electrolyte is assumed to be symmetrical, *i.e.* the absolute values of the signed units of charge (z) are the same for all ions present.

Most of these assumptions are valid with some limitations, for example, ions are known to possess characteristic radii and the dielectric constant in a polar medium may be reduced due to orientation of the polarized molecules close to the charges in the surface. Particularly, the assumption that the surface is uniformly charged is really crucial for the mathematical description of an electric double layer system. Also in this case we know that the surface charge will be changed by modifying the environment of the interface, *e.g.* changing the electrolyte concentration or bringing two surfaces very close one to each other. However, results obtained under these assumptions are really useful for the understanding of electrical phenomena in colloidal systems.

In order to describe a solution of electrolytes and colloids, it is necessary to employ Boltzmann's distribution law, which relates the probability of a unit (atom, molecule, ion, particle, etc.) being at a certain point with a specified free energy (or potential energy), $\Delta\psi$, relative to a specified reference state. The probability is generally expressed in terms of an average unit concentration, c, at the point r relative to a concentration, c_0, at some reference distance in which the energy is taken as zero. At a temperature, T, the Boltzmann distribution is given as:

$$c = c_0 \exp\left(\frac{-\Delta\psi}{k_B T}\right). \tag{2.7}$$

Lets consider the electric potential at the flat surface to be ψ_0 and ψ at a distance x from the surface in the electrolyte solution. If the surface is positively charged, as shown in Fig. 2.3, Eq. (2.7) predicts that:

$$n_+ = n_0 \exp\left(\frac{-ze\psi}{k_B T}\right) \quad \text{and} \quad n_- = n_0 \exp\left(\frac{+ze\psi}{k_B T}\right), \tag{2.8}$$

where n_+ and n_- are the number of positive and negative ions per unit volume at points with a distance x from the surface where the potential is ψ (*i.e.* where the electric potential energy is $ze\psi$ and $-ze\psi$ respectively), and n_0 is the corresponding bulk concentration of each ionic species. Here z is the valency of the ions.

Although the solution as a whole is electrically neutral, in the regions close to the electrical potential there is an imbalance of electrical charges. For example, in a region with a negative ψ, there will be more positive than negative ions. Therefore, the net volume charge density ρ at points where the potential is ψ, is given by

$$\begin{aligned}\rho &= ze\left(n_+ - n_-\right) \\ &= zen_0\left[\exp\left(\frac{-ze\psi}{k_BT}\right) - \exp\left(\frac{+ze\psi}{k_BT}\right)\right] \\ &= -2zen_0 \sinh\frac{ze\psi}{k_BT}. \end{aligned} \tag{2.9}$$

The region around a potential that accumulates charge with opposite sign is generally referred as "ionic atmosphere" or "charge cloud" associated with that potential. For a flat double layer, ρ is associated with ψ by Poisson's equation in the form:

$$\frac{d^2\psi}{dx^2} = -\frac{\rho}{\varepsilon}, \tag{2.10}$$

where ε is the permittivity. Then by combining Eqs. (2.9) and (2.10) we get

$$\frac{d^2\psi}{dx^2} = \frac{2zen_0}{\varepsilon}\sinh\frac{ze\psi}{k_BT}. \tag{2.11}$$

The solution of this second order differential equation, taking into account the boundary conditions ($\psi = \psi_0$ when $x = 0$ and $\psi = 0$ or $d\psi/dx = 0$ when $x = \infty$), can be written in the form:

$$\psi = \frac{2k_BT}{ze}\ln\left(\frac{1+\gamma\exp(-\kappa x)}{1-\gamma\exp(-\kappa x)}\right), \tag{2.12}$$

where

$$\gamma = \frac{\exp(ze\psi_0/2k_BT) - 1}{\exp(ze\psi_0/2k_BT) + 1}, \tag{2.13}$$

and

$$\kappa = \left(\frac{2e^2n_0z^2}{\varepsilon k_BT}\right)^{1/2} = \left(\frac{2e^2N_Acz^2}{\varepsilon k_BT}\right)^{1/2} = \left(\frac{2F^2cz^2}{\varepsilon RT}\right)^{1/2}, \tag{2.14}$$

where in the first step we used the definition of Avogadro's constant ($N_A = n_0/c$), with n_0 being the concentration of ions in the solution and c the molar concentration of the electrolyte, while in the second step we used the two relations of Boltzmann's and Faraday's constants $k_B = R/N_A$ and $F = eN_A$ respectively.

κ is commonly referred as the "Debye length" and is reciprocally related to the electrical double layer thickness. Thus, we can observe that the thickness of the electrical double layer ($1/\kappa$) is inversely proportional to the concentration of electrolyte in the system and to the square of the valency of the ions involved. Particles separation distance in a given system will depend, among other things,

on these two factors that will play a very important role for manipulating the characteristics and stability of many colloidal systems.

If we apply the high-temperature or low potential limit $z\psi_0 \ll 2k_BT/e$, we can Taylor expand the exponential

$$\exp\left(\frac{ze\psi_0}{2k_BT}\right) \approx 1 + \frac{ze\psi_0}{2k_BT}. \tag{2.15}$$

This is know as Debye-Hückel approximation that can be used to simplify Eqs. (2.12) and (2.13) to

$$\psi = \psi_0 \exp(-\kappa x). \tag{2.16}$$

Equation (2.16) shows that at low potentials ($z\psi_0 \ll 25.6$ mV at 25°C) the electrical potential in the solution falls exponentially with distance from the charged surface. However, in regions very close to the surface, the potential is likely to be relatively high, therefore the Debye-Hückel approximation does not hold and the potential will decrease at a rate grater than exponential decay.

By equating the surface charge with the net space charge in the diffuse part of the double layer (*i.e.* $\sigma_0 = -\int_0^\infty \rho dx$) and applying the Poisson-Boltzmann distribution, a relation between the potential ψ_0 and the charge density σ_0 at the surface can be obtained. For the simple case of a flat surface and using the assumptions introduced before, the resulting expression is:

$$\sigma_0 = (8n_0\varepsilon k_BT)^{1/2} \sinh\frac{ze\psi_0}{2k_BT}, \tag{2.17}$$

where at low potentials we can use the same approximation used before to get:

$$\sigma_0 = \varepsilon\kappa\psi_0. \tag{2.18}$$

From Eq. (2.18) we see that the surface potential ψ_0 depends on both the surface charge density (σ_0) and on the ionic composition of the medium through Debye length (κ) shown in Eq. (2.14).

If we consider an aqueous solution of a symmetrical electrolyte at 25°C, κ can be simplified to the following relationship:

$$\kappa = 0.329 \times 10^{10} \left(\frac{cz^2}{mol\ dm^{-3}}\right)^{1/2} m^{-1}, \tag{2.19}$$

where for a 1-1 electrolyte, the double layer thickness will be about 1 nm for a 10^{-1} mol dm^{-3} solution and 10 nm for a 10^{-3} mol dm^{-3} solution. For unsymmetrical electrolytes the double layer thickness can be estimated by considering z to be only the counter-ion charge number.

Recalling the volume charge density (Eq. (2.9)), the Poisson-Boltzmann distribution for a spherical interface can be written in the form

$$\nabla^2\psi = \frac{1}{r^2}\frac{d}{dr}\left(\frac{r^2 d\psi}{dr}\right) = \frac{2zen_0}{\varepsilon}\sinh\frac{ze\psi}{k_BT}, \tag{2.20}$$

where r is the distance from the center of the sphere. Analytical solutions for this expression cannot be calculated without approximation to the exponential terms. Thus, if we apply the already described Debye-Hückel approximation, Eq. (2.20) reduces to:

$$\nabla^2\psi = \kappa^2\psi. \tag{2.21}$$

By considering the boundary conditions ($\psi = \psi_0$ at $r = a$ and $\psi = 0$ or $d\psi/dx = 0$ when $x = \infty$) the integration of Eq. (2.21) gives:

$$\psi = \psi_0 \frac{a}{r} \exp\left(-\kappa\left(r - a\right)\right). \tag{2.22}$$

This expression is known as Yukawa potential or screened Coulomb potential. Unfortunately the low potential limit ($z\psi_0 \ll 25.6$ mV at 25° C) is often not a good choice to treat colloid and surface phenomena. Therefore, unapproximated numerical solutions of Eq. (2.20) have been computed [27].

Ion Adsorption and Stern Layer

In the previous sections, in order to describe the diffuse part of the double layer, we assumed that the ions present in the medium were point charges. However the actual finite size of ions establish a limit close to the surface, in which the center of each ion can only approach the surface, without become adsorbed, by its hydrated radius. In a work published in 1924, Stern suggested a model in which a plane, located at about a hydrated ion radius from the surface, delimits an internal fixed layer (Stern layer) composed by adsorbed ions and divides the double layer into two parts (see Fig. 2.4) [28].

The adsorbed ions are kept fixed (albeit temporarily) in a certain position at the surface by electrostatic and/or van der Waals forces that are strong enough to overcome thermal agitation. Because ions in the Stern layer are "fixed", they effectively screen or neutralize a portion of the surface charge changing the potential from ψ_0 (at the surface) to ψ_d (at the Stern plane). Ions with centers located beyond the Stern plane are considered to form the diffuse part of the double layer, in which the Gouy-Chapman treatment described in the past section is valid. In this case, the surface potential ψ_0 is replaced by ψ_d which is the Stern potential (Fig. 2.4).

Generally, in an electrolyte, both counter- and co-ions are adsorbed on the surface, however, counter-ion adsorption usually predominates over co-ions adsorption, screening partially the surface potential and giving rise to a typical double layer composition described in Fig. 2.4. Indeed it is possible, especially with polyvalent or surface-active counter-ions, to reverse the surface charge in such a way that the surface potential ψ_0 has opposite sign respect to the Stern potential ψ_d (Fig. 2.5 (a)). On the other hand adsorption of surface-active co-ions could increase the surface charge and create a situation in which the surface potential ψ_0 has the same sign as the Stern potential ψ_d, but higher magnitude (Fig. 2.5 (b)).

To describe the equilibrium between ions adsorbed on the surface and those in the diffuse part of the double layer Stern assumed that a Langmuir adsorption isotherm can be used. There exists many types of adsorption isotherm which differ in one or more assumptions used to derive the expression of surface coverage. Particularly,

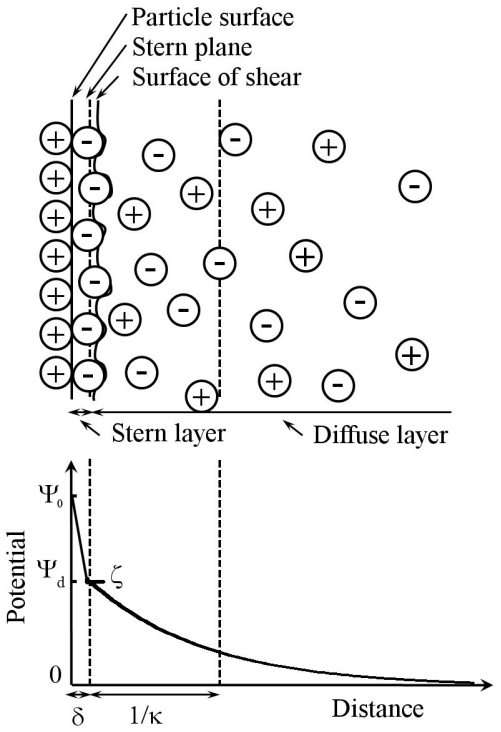

Figure 2.4. Schematic representation of the electric double layer structure according to Stern's theory.

Langmuir adsorption isotherm is one of the simplest and was proposed by Irving Langmuir in 1916 to describe the dependence of the surface coverage of an adsorbed gas on the pressure that it exerts on the surface at a fixed temperature. This model assumes that a surface consists of a given number of available sites N_m that can be physically or chemically stick by N_1 atoms or ions. If we define the fractional coverage as $\theta = N_1/N_m$, the adsorption rate (ν_a) will be proportional to the concentration of atoms or ions c above the surface and to the fraction of the surface that is not covered $(1-\theta)$

$$\nu_a = k_a c\,(1-\theta)\,, \tag{2.23}$$

where k_a is the rate constant for adsorption. On the other hand, the desorption rate is simply proportional to the fraction of surface that is covered

$$\nu_d = k_d \theta, \tag{2.24}$$

with k_d being the rate constant for desorption. In equilibrium we have that ν_a is equal to ν_d, thus

$$\frac{\theta}{1-\theta} = \frac{k_a c}{k_d} \quad \text{or} \quad \theta = \frac{Kc}{1+Kc}, \tag{2.25}$$

where K is an equilibrium constant ($K = k_a/k_d$). If we consider only the adsorption of counter-ions with adsorption energy divided between electrical ($ze\psi_d$) and van

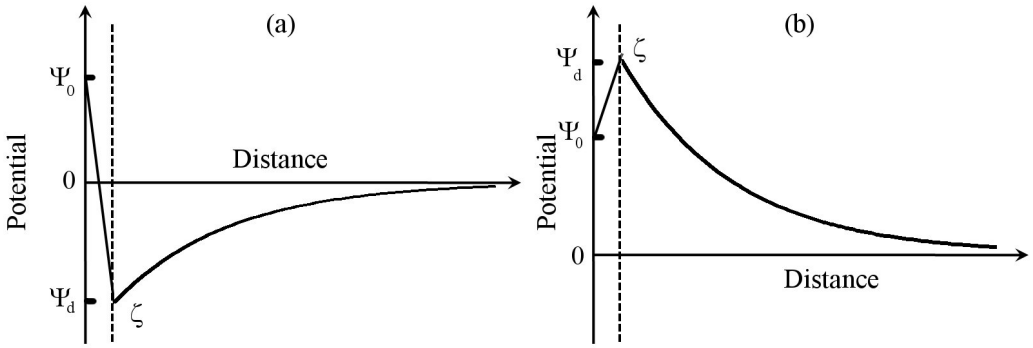

Figure 2.5. (a) Reversal of charge due to the adsorption of surface-active or polyvalent counter-ions. (b) Surface-active co-ions adsorption.

der Waals (ϕ) terms, the binding constant can be represented by $K = \exp((-ze\psi_d + \phi)/k_BT)$ and the surface charge density σ_1 of the Stern layer is given by the expression

$$\sigma_1 = \frac{\sigma_m}{1 + \frac{N_A}{n_0 V_m} \exp\left(\frac{-ze\psi_d + \phi}{k_B T}\right)}, \tag{2.26}$$

where σ_m is the surface charge density corresponding to a monolayer of counter-ions, N_A is Avogadro's constant and V_m is the molar volume of the solvent. Here we have used $\sigma_1 = zeN_1$.

By treating the Stern layer as an ideal parallel plate capacitor (molecular condenser) of thickness δ and permittivity ε', the charge density at the particle surface can be written as

$$\sigma_0 = \frac{\varepsilon'}{\delta}(\psi_0 - \psi_d)\,. \tag{2.27}$$

Assuming that each particle reaches the electrical neutrality throughout the whole of the double layer, we have that

$$\sigma_0 + \sigma_1 + \sigma_2 = 0, \tag{2.28}$$

where σ_2 is the surface charge density of the diffuse part of the double layer and is given by Eq. (2.17) with opposite sign and the potential ψ_0 substituted by the Stern potential ψ_d. If we substitute Eqs. (2.27), (2.26) and (2.17) into (2.28), we obtain a complete expression to describe the double layer problem according to the Stern model:

$$\frac{\varepsilon'}{\delta}(\psi_0 - \psi_d) + \frac{\sigma_m}{1 + \frac{N_A}{n_0 V_m} \exp\left(\frac{-ze\psi_d + \phi}{k_B T}\right)} - (8n_0\varepsilon k_B T)^{1/2} \sinh\frac{ze\psi_d}{2k_B T} = 0. \tag{2.29}$$

We can observe that this expression has some unknown quantities. Fortunately some informations of the system can be obtained by some experimental techniques.

For example, the Stern potential (ψ_d) can be estimated from electrokinetic measurements and, for some systems, electrocapillary or potentiometric titration measurements can be used to determine the total capacity of the double layer that is associated with the charge density and potential.

The electric double layer interaction is very important for the stabilization of colloidal suspensions, avoiding particles to aggregate due to van der Waals and sediment. A classical example is the milk that exists only because the fat droplets suspended in a water-based solution are covered with a double layer that prevent their coagulation into butter.

2.2.3 Interaction Potential of Laponite Particles

To obtain an effective potential that well describes Laponite system is very challenging, due to particles shape and charge distribution anisotropy. The first great contribution to understand this potential came from Secor and Radke that numerically solved the Poisson-Boltzmann equation for a thin disc with negative charge on its surface and positive on its rim immersed in an electrolyte solution [29]. They showed that for an unsymmetrical electrolyte concentrations the negative electrostatic field emanating from the particle face spills over into the rim region giving rise to a completely repulsive interactions between the particles even for a face-rim configuration. More recently Sun and co-authors used the same method to calculate the distribution of the electrostatic potential around a Laponite disc [30]. They considered a Laponite disc with radius of 15 nm, thickness of 1 nm, negative face charge of $-700\ e$, rim charge of $+50\ e$ at pH $\lesssim 11$ and the sum of 5.0 mM of added NaCl and 1.07×10^{25} m^{-3} of released Na^+ estimated by Jabbari *et al.* for a 2% sample [20].

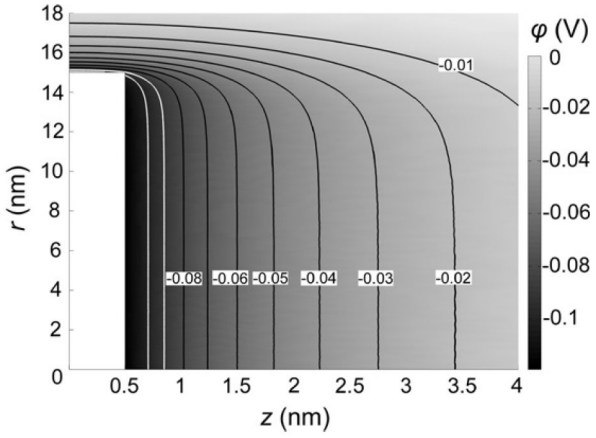

Figure 2.6. Electrostatic potential distribution around a Laponite particle in a 2% suspension with 5 mM of added NaCl [30].

Figure 2.6 shows a two dimensional picture of the equipotential lines surrounding a Laponite disc disposed with its center perpendicular to the x axis. The spillover of the negative electrostatic potential is also observed meaning that, despite Laponite particles have positive charge on the rims, the electrostatic double layer interaction

will be always repulsive, even for the higher salt concentration added to the system (5.0 mM).

The first application of Debye-Hückel framework to colloidal dispersions was done by Levine and Dube who found that charged colloidal particles should be expressed by a weak long-range attraction and a strong medium-range repulsion [31, 32]. However this theory failed to explain the instability observed in colloidal dispersions against irreversible aggregation in solutions of high ionic strength. In 1941, Derjaguin and Landau introduced a theory for the stability of colloidal dispersions, that also describes the instability due to aggregation, by taking into account the strong but short-ranged van der Waals attractions [33]. Some years later, Verwey and Overbeek independently obtained the same results [34] and nowadays this model is known as DLVO theory named from those contributions. Basically this theory assumes the association between both electrostatic screened repulsion (Yukawa repulsion for spheres) and short range van der Waals attractions. For spheres, the schematic DLVO free energy as a function of surface to surface particle separation is shown in Fig. 2.7. The combination between both attractive and repulsive interactions give rise to an energy barrier that keep the particles away from each other preventing aggregation. However, if the particles have enough energy to overcome that barrier, they will stick together forming bigger clusters or aggregates.

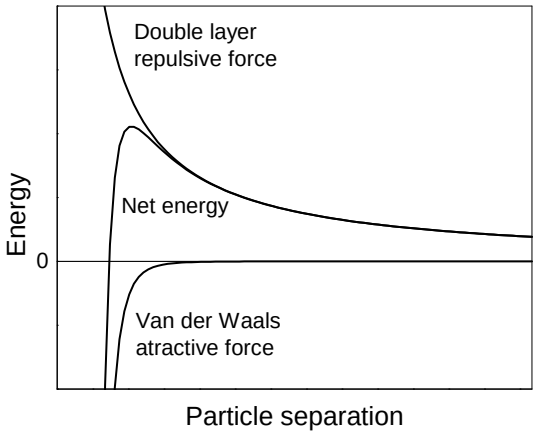

Figure 2.7. Schematic graph of the free energy variation as a function of surface to surface particle separation according to the DLVO theory. The net energy is calculated by the sum of both double layer and van der Waals interactions.

The height of this energy barrier that prevents aggregation, can be easily modified by changing some parameters of both Yukawa or van der Waals potentials. For example, any change in the dielectric constant of the solvent will affect both attractive and repulsive interactions through the Hamaker constant and the electrostatic terms, the increasing of salt concentration will change the Debye screening length in such a way that the range of the electrostatic term decreases (the same effect is achieved by increasing the counter-ion valence) and also the change in the thermodynamics quantities will modify the electrostatic repulsion since the Debye screening length depends explicitly on the density and temperature.

DLVO theory has been widely applied to study many type of spherical colloidal dispersions. However, a big interest regarding charged disc-like colloids arose after the observation of nematic phases by Langmuir in 1938. Recently Trizac and coworkers gave a big contribution to obtain a satisfactory generalization of DLVO theory for charged disc-shaped particles incorporating also the non-linear effects of counter-ion condensation (charge renormalization) [35, 36, 37]. To describe the effective pair potential between the discs with arbitrary orientation they have solved the Poisson-Boltzmann equation, assuming the Debye-Hückel approximation (Eq. (2.15)), for two discs at large distances ($r/\kappa \ll 1$) and showed that a Yukawa potential (Eq. (2.22)) still describes the effective interactions, with a prefactor which depends both on the renormalized charge and on the orientations of the two discs [37]. At fixed centre-to-centre distance, the repulsive interaction is maximized for co-planar configuration ($\theta_A = \theta_B = \pi/2$ that corresponds to the maximum electric double layers overlap) and minimized for co-axial and parallel configurations where $\theta_A = \theta_B = 0$ (see Fig. 2.8).

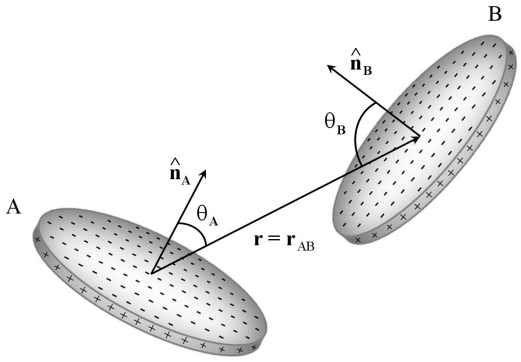

Figure 2.8. Coordinates defined to describe the interaction between two discs [37].

As discussed in the past section, the Debye-Hückel approximation is not valid for particles with large bare charge (as in the case of Laponite). However, for distances sufficiently away from the particle surface (of the order of Debye length) and effective charge much smaller than the bare, it may still be valid. For example, if we assume $\kappa \sim R$ (where R is the particle radius), the upper charge boundary to maintain the validity of Debye-Hückel approximation is $\sim 100e$, that is considerably smaller than the Laponite bare charge.

Despite the lack of a good effective potential to describe Laponite systems, several models have been adopted to explain the rich phase diagram of this system [16, 38, 39, 40, 41, 42]. Jonsson *et al.* performed Monte Carlo simulations for two discs composed by positive and negatively charged spheres immersed in an electrolyte solution to show the energetically preferred configurations at different ionic strength (Fig. 2.9) [42]. In this model they assumed a total interaction composed by Yukawa repulsion and van der Waals attraction terms and used the dielectric continuum model (primitive model), where the solvent is described as a structureless medium characterized only by its relative dielectric permittivity (ε_r). The global minimum is always found for PPO configurations (Fig. 2.9 (b)), while the T-bond configurations (Fig. 2.9 (a)) appear only for salt concentration bigger than

40 mM and represent only a local minimum. With no added salt ($C_s < 5$ mM) the electrostatic repulsion dominates, while a slight addition of salt is enough to trigger a net attraction between the discs. As the attractive potential term appears ($C_s >$ 10 mM) the PPO configuration represents always the lowest energy configuration, while the T-bond configuration comes out only for higher salt concentrations (C_s > 40 mM) and represents only a local minimum. The authors found that the role of the van der Waals interactions is not significant for low ionic strength and it starts to give an important contribution for intermediate salt concentrations (C_s > 100 mM). At sufficiently high salt concentration ($C_s > 200$ mM), the van der Waals interaction dominates and the net interaction becomes strongly attractive for all particle separations. This work stressed the importance of the van der Waals interaction for salt values not experimentally accessible. However, experimental works show that low concentrated Laponite suspensions reach a non ergodic phase (gel) even for very low ionic strength ($C_s < 5$ mM) indicating that this model still not describes perfectly the complex behavior of Laponite systems.

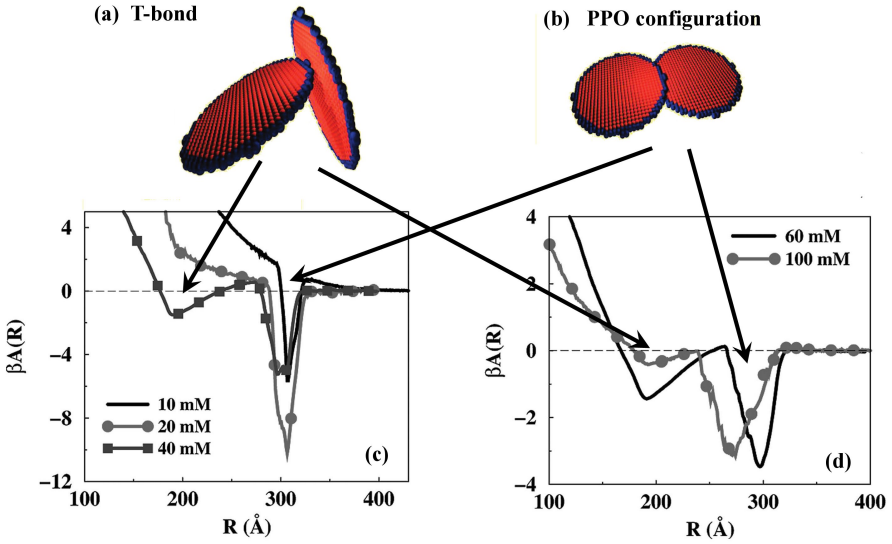

Figure 2.9. Schematic model of two discs composed by 556 negatively charged spheres in the center (blue) and 100 positively charged spheres on the rims (red) used by Jonsson *et al.* to simulate the corresponding energy for different configurations [42]. Here we show (a) the T-bond and (b) PPO configurations with an arrow indicating their minimum free energy value in respect to center to center distance.

Recently Ruzicka and coworkers introduced the patchy model to describe the low-density behavior of the experimental data of Laponite in the context of low-valence systems [16]. In this model each disc is composed by 19 sites (red spheres) with five short-ranged attractive patches (blue spheres), three located on the rim and one at the centre of each face (see Fig. 2.10). The overall repulsive electrostatic interaction is neglected.

Since only face-rim bonds can be formed, a square-well attraction is active only between face and rim sites, while face-face and rim-rim sites are considered to be non-interacting. In this primitive model the short-range nature of attractive interactions ensures that each site is involved in at most in one T-bond configuration.

Thus, the idea behind this model is that the combination between the anisotropy of the discs and the directional face-rim attraction favors the formation of low-density bonded networks, with only a few bond per particle (low valence), as expected in Laponite systems that forms macroscopic networks at extremely low densities.

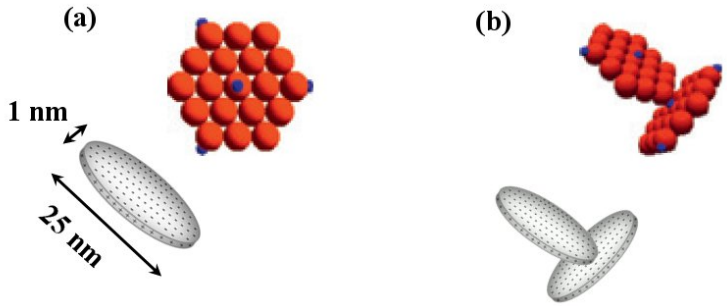

Figure 2.10. (a) Sketch of a Laponite disc composed by 19 sites (red spheres) with five attractive patches (blue spheres), three located on the rim and one at the center of each face, used by Ruzicka *et al.* for simulations [16]. (b) Representation of the T-bonded configuration for two interacting Laponite discs.

2.3 Aging and Arrested States

In condensed physics systems a glass can be obtained by means of a temperature quench. During this process the temperature of a melted material is quickly decreased in such a way that the atoms froze in the previously liquid (disordered) configuration. In soft glassy materials, such as colloidal systems and foams, this process can be achieved by increasing the concentration of particles or bubbles. Initially works focusing on the features of the fluid-solid transition in disordered materials introduced the concept of *jamming* [43, 44]. The viscosity of jammed systems is so hight that, due to their crowding, and/or to the presence of strong attractive or repulsive interactions, the mobility of the constituents is extremely reduced. These systems are in a far-from-equilibrium configuration, which means that the particles can not reach the lowest possible energy configuration. Actually, one of the most striking features of non-equilibrium system is that the sample properties are continuously changing with time as the system slowly evolves towards its equilibrium configuration, never reachable. For example, if we carry out a response experiment, that is if we weakly perturb the glassy system at a given time t with an external field and measure the response (activity) of its conjugated variable at some later "waiting" time t_w, we observe that the response depends on the time elapsed after perturbation. This phenomenon is called aging and is easily observed through the time correlation functions of non-equilibrium system.

Understanding the slow dynamics of systems under aging have been a challenge for longtime. Although many advances have been obtained, it is still unclear whether any existing theory provides a correct and complete description of the dynamics and the related glass transition. The discussion about the glass transition as an universal kinetic process has intensified greatly since the advent of the mode coupling theory (MCT) by Bengtzeliuus [45], Leutheuser [46], and Götze and Sjölander [47, 48].

The main presupposition of the MCT is the non-linear coupling between pairs of density fluctuation. Increasing the strength of this coupling, either by decreasing the temperature or increasing the density, causes a dynamic instability where the structure of the system becomes permanently frozen. At that moment the system is non-ergodic in the sense that during the course of the measurement only a restricted part of the phase space available to the system is explored [49].

The MCT has attracted much attention due to the interesting predictions regarding the aging and the glass transition of glassy systems in terms of density-density correlation function. The theory identifies that beyond the time scale of microscopic motions, the relaxation of the intermediate scatterings function (density autocorrelation) proceeds in two stages, as shown in Fig. (2.11).

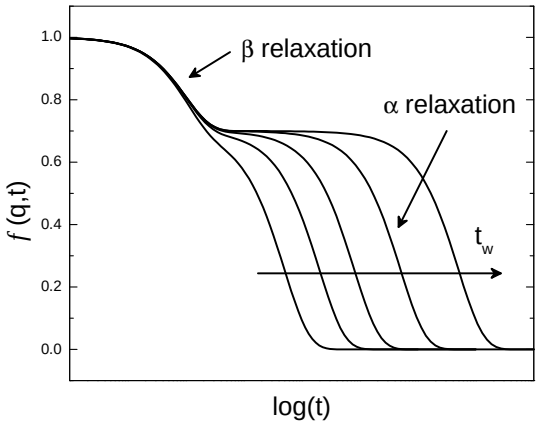

Figure 2.11. Illustrative picture of the prediction of the Mode Coupling Theory. The intensity correlation function shows two relaxation times: β for the fast relaxation and α for the slow relaxation. The α mode becomes slower due to the progressive frozen-in of the intensity fluctuation of the system with waiting time t_w.

The β or fast relaxation is associated with the rapid motion of the particles inside the cage formed by its neighbors. In other words, in a short time scale a single particle is trapped among the neighboring particles in such a way that it maintains its original position almost unchanged and exchange kinetic energy mainly through phonon-like modes with the surrounding environment. On the other hand α relaxation corresponds to the slow rearrangements of the cages, that is the relaxation of the whole structure. Moreover MCT predicts that β relaxation time remains almost constant when the system approaches the glass transition, while α becomes slower as the system evolves on time, reflecting the progressive frozen-in of the density fluctuations.

Another way to understand this two step relaxation process observed in glassy system is through the complex free-energy landscape that is formed by a large number of basins that correspond only to local minima separated by higher barriers. During an aging process at early times the system is able to access at least part of the energy states by thermally overcoming barriers and getting out of local minima. However, as time passes, the system falls down each time in a deeper minima that

is more difficult to escape from. Consequently the kinetics of the system during aging become slower and slower, in such a way that the system cannot reach the thermodynamic equilibrium, that is, non-ergodic state. During aging, the viscosity of the system increases and the diffusion coefficient of the particles decreases. This suggests that the trapping of particles in cages formed by neighbors in real space is equivalent to the arrest of the system in a local minimum of the free energy landscape.

Laponite dispersions have been extensively explored in the past years and different non-ergodic states have been observed. Because of the competition of short range Van der Waals attractions, short range patchy attractions and long range electrostatic attractions and repulsions, the final arrested states will strongly depend on the ionic strength of the medium and on Laponite concentration and will be characterized by different interparticles interactions. Due to the shape and charge anisotropy of Laponite particles, the final arrested states have been always found in disordered structures, such as gel or glass, while a more organized nematic phase is perhaps found for high Laponite concentrations [50]. Despite a gelation process presents a kinetic behavior similar to the glass formation, their sub-products, gel and glass, have structures and physical meanings completely different one from each other. Gel and glass can be differentiated in a broad sense, however the density of the system is generally used to classify them. For example glasses typically arise in dense fluids, due to supercooling or compression, and the arrested state is described by the cage effect felt by the particles between the neighboring ones. On the other hand gels are characterized by the formation of a percolated network that extends over the whole length of the sample space. These percolated structures give the characteristic of very low density for gels compared with glasses (see Fig. 2.12).

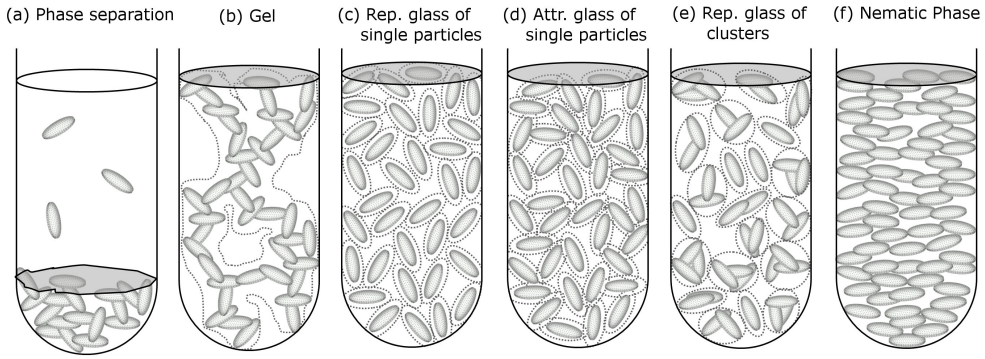

Figure 2.12. Schematic structure of the arrested states of Laponite: (a) phase separation, (b) gel, (c) repulsive glass of single particles, (d) attractive glass of single particles, (e) repulsive glass of clusters and (f) nematic phase.

Regarding the interparticle interaction, while attraction is necessary to form a gel, a glass can be either repulsive or attractive. As previously described, the high density present in attractive glasses differentiate them from gels. However, repulsive glasses can also be found at very low densities. In this case particles do not form a network, but remain spatially disconnected although arrested in a sort of empty cage stabilized by electrostatic repulsions. In this repulsive glass (also called Wigner

glass) the interparticles distance should be on average larger or comparable to the particle size [51]. On the other hand attractive glass has interparticle distances smaller than that of repulsive Wigner glass and bigger than that of gel, presenting also a structure of disconnected particles. Repulsive Wigner glass in some cases can be also observed with formation of small clusters (Fig. 2.12 (e)). In this case a remaining repulsive force between clusters is responsible for the "stabilization" of the arrested structure. A simple way to distinguish if repulsive or attractive interactions are responsible of the arrested structure is to perform a "dilution test" that consists on the addition of a solvent on the arrested structure. If the glass is formed due to repulsive interactions, it will melt and reorganize in a new disordered structure. On the contrary if the dominant interaction is attractive, the arrested state should remain solid because the attractive bonds between the particles are not altered by the solvent [15, 52].

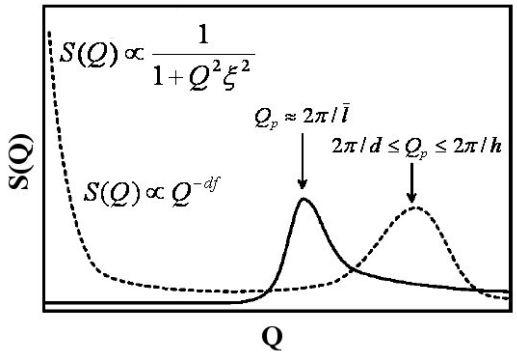

Figure 2.13. Characteristic static structure factor of a gel (dashed line) and a glass (full line) reported by Tanaka *et al.* [13].

A clear way to differentiate gel and glass is to investigate their static structure factors that should be significantly different, as it is schematically shown in Fig. 2.13 [13]. A glass, represented by a full line in Fig. 2.13, presents a peak on $S(Q)$ at lower Q-values compared to that of a gel (represented by a dashed line in Fig. 2.13), due to the fact that the interparticle distance is higher for glasses. In other words, the attractive nature of gels gives rise to a percolated aggregates network that has a shorter interparticle distance compared with glasses (see Fig. 2.12). Besides, gel systems exhibit an excess scattering at low Q, which reflects the correlation of the concentration fluctuations associated with the network structure.

2.4 Phase Diagram of Laponite

It is important to clarify that in this work we are frequently using the term 'phase diagram' to describe diagrams containing also non-ergodic states. Such non-ergodic states are metastable states in a non-equilibrium configuration caused by the slowing down of the particles due to different arrested mechanisms. Despite non-ergodic states are in a non-equilibrium configuration (*i.e.* disordered states) we will identify the phase diagram of Laponite in the limit of very long times, that is, when the system, through slow aging dynamics, reaches a 'stable' arrested state in which the

sample properties remain unchanged during a long time scale.

The first investigations of Laponite phase diagram were performed in 1995 by Mourchid and coworkers, who reported a rich phenomenology by changing both clay concentration and ionic strengths, using rheological, osmometric and birefringence (BF) measurements [10, 53]. As shown in Fig. 2.14 (a), four "phases" have been suggested:

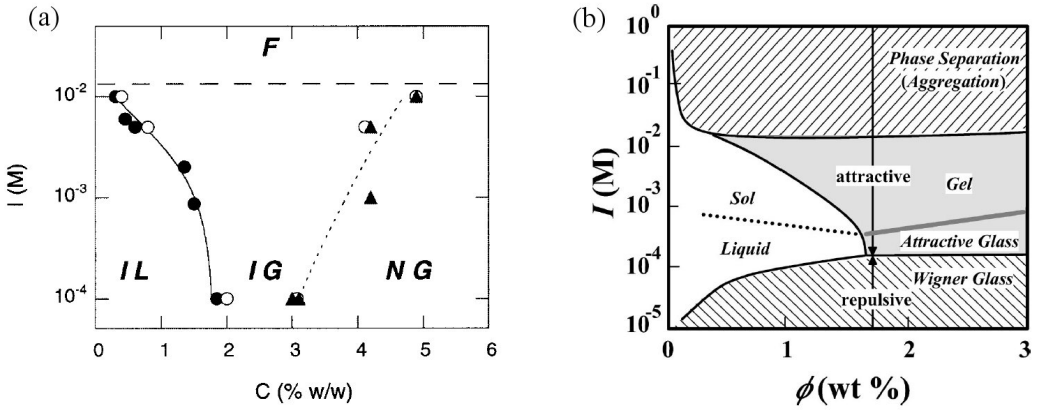

Figure 2.14. (a) Phase diagram for Laponite suspensions by changing both clay and salt concentrations obtained by (•) rheological, (○) osmometric, and (▲) birefringence (BF) measurements. F, flocculation; IL, isotropic liquid; IG, isotropic gel; NG, nematic gel [53]. (b) Phase diagram proposed by Tanaka *et al.* [13].

- IL: Isotropic Liquid. For low ionic strength and Laponite concentrations, the potential barrier is sufficiently high to prevent the colloidal particles from coming into contact, and single or only small Laponite aggregates form remaining suspended in water due to Brownian motions. The size and compactness of the aggregates may depend on electrolyte concentration through Debye screening length (κ). In general the aggregates formed are small and do not strongly scatter visible light in such a way that the sample is transparent with a viscosity not so different from that of water (increasing with ionic strength).

- IG: Isotropic Gel. For intermediate Laponite concentration a percolating mechanism is promoted by attraction between oppositely charged rim and faces and is reinforced by Van der Waals interactions, yielding to the "house of cards" structure. The gelation mechanism is favored by increasing the ionic strength due to the screening of the repulsive double layer. For low electrolyte concentration the gel is transparent since the formed structures are still small.

- NG: Nematic Gel. For high clay concentrations Laponite discs or small stacked aggregates of discs orient respect to each other in domains over macroscopic length scales. This ordering can be observed by macroscopic birefringence.

- F: Flocculation. Ionic concentration is so high that the repulsive double layer is strongly screened, giving rise to the formation of large aggregates that no longer perform Brownian motion and sediment, originating in this way a

clay-water "phase separation". In this case the aggregates structure becomes micrometer sized and the scattered light is stronger, generating a macroscopic opaqueness.

These early studies however neglected the fact that the samples are continuously aging with time. For example, for low ionic strength ($I \sim 10^{-4}$ M) and Laponite concentration ($C_w < 1.8\%$), a "young" sample remains in a liquid state for months before it reaches a "stable" arrested state. Thus, this led to a misinterpretation in the region where the aging is very slow (IL region) and opened the way for a large number of subsequent experimental and theoretical investigations [54].

Since the time that the sample needs to reach a "stable" non-ergodic state is very small (minutes) for high ionic strength ($I > 10^{-2}$ M) and Laponite concentration ($C_w > 3\%$), we expect that these regions F and NG will not be affected by the lack of aging considered in the phase diagram showed in Fig. 2.14 (a). In fact, there exist in literature important evidences of birefringence in Laponite reporting the formation of an ordered nematic phase for a clay concentration range comparable to that reported in Fig. 2.14 (a), if one takes into account the different aspect ratio (1:40) of Laponite B samples used in this experiment compared to that (1:30) of Laponite RD used by Mourchid [55, 56].

Now, lets concentrate on the IG region of Fig. 2.14 (a) that has been extensively explored and shows an intermediate aging time (hours/days) to reach a "stable" arrested phase. Kroon and co-authors have found, by means of Dynamic Light Scattering (DLS) measurements, that the samples, initially liquid, perform aging up to the final non-ergodic state, with waiting time depending on Laponite concentration for a fixed ionic strength [57]. Later on, Bonn and co-workers used DLS to study a sample with $C_w = 3.5\%$ and argued that the combination of a flat, Q-independent, scattered intensity (typical of homogeneous systems) and the extremelly low density of the samples (translated into packing fraction, $\phi = 0.014$), compared with the typical value of the glassy density observed in a spherical colloids ($\phi \gtrsim 0.5$), are compatible with the interpretation of this non-ergodic state as a Wigner glass [58]. Taking into account the electrostatic interactions, the authors calculated (assuming a Debye screening length of about 30 nm at $C_s = 10^{-4}$ M) an effective volume fraction $\phi \approx 0.43$ comparable with that of a glassy system, but much larger than the actual value occupied by the Laponite discs.

Subsequent investigations done by Levitz *et al.*, supporting the idea of Wigner glass instead of gel, reported the observation of a re-entrant fluid-solid transition for lower salt concentrations ($10^{-5} \leq C_s \leq 10^{-4}$ M obtained by means of ion exchange resins) and low Laponite concentrations ($0.4\% \leq C_w < 2.0\%$) [11]. Through Ultra Small Angle X-ray Scattering (USAXS) and (SAXS) measurements they found that the electrostatic interactions are responsible for the formation of a disordered solid state (lack of Bragg peaks), in agreement with the Wigner glass interpretation. The measured structure factors seem to indicate the presence of microdomains (clusters), rather than fractal-like large aggregates characteristic of a gel structure. This evidence could be a hint to the existence of Wigner glass of clusters, a state that was recently found in spherical colloids [59, 60].

Turning to the low clay concentration region, Nicolai and co-workers investigated the waiting time dependence of sol-gel boundary previously found by Mourchid *et al.*

without considering any aging behavior. They were the first to explore a very low clay concentration region by means of Static and Dynamic Light Scattering (SLS and DLS) techniques in the salt concentration range of $10^{-3} \leq C_s \leq 10^{-2}$ M [12, 61, 62]. They found that the gel-like behavior does not immediately manifest after sample preparation, but develops slowly with increasing waiting time. Consequently, they argued that the phase diagram found by Mourchid *et al.* (Fig. 2.14 (a)) depends on waiting time, and should not be considered as an "equilibrium" phase diagram. Besides, Nicolai *et al.* improved the phase diagram of Laponite by observing sedimentation (phase separation or flocculation) for samples with $C_s = 10^{-3}M$ and very low clay concentration ($C_w < 0.3\%$). Again, this discrepancy arose due to the fact that sedimentation of very low clay concentration takes several months to happen, long waiting times that were not considered by Nicolai and co-workers. Investigating the evolution of the scattered intensity of samples with $C_w < 2.0\%$ and different salt concentrations, they found a Q-dependence that can be described by a power law, indicating that fractal aggregates are formed. From these studies, on samples with $C_w < 2.0\%$ in salt free water ($C_s = 10^{-4}$ M), Nicolai and co-authors concluded that the arrested structure is characterized by a gel instead of a Wigner glass as claimed by other authors [12].

The controversy about gel or glass nature of the arrested states was also discussed by Tanaka *et al.* who combined several observations from different groups [11, 53, 58, 62, 63] to propose a new phase diagram which reconciles the existence of gel, attractive and Wigner glass (Fig. 2.14 (b)) [13]. The idea in this study was to use the phase diagram for uncharged spheres as a reference, and adapt it to Laponite taking into account the effect of charges and the experimental results available in literature. Again the low Laponite concentration range was considered to be liquid/sol phase, ignoring the slow aging behavior of the system in this region. For high clay concentration they supported the idea that the arrested state is a Wigner glass for $C_s < 10^{-4}$ M, passing to an attractive glass and gel by increasing the ionic strength (see Fig. 2.14 (b)).

Finally, the issue of waiting time was properly taken into account by Ruzicka and coworkers who investigated a large range of Laponite concentrations ($0.3\% \leq C_w \leq 3.1\%$) in salt free water by means of DLS [54]. They found a surprising new picture where a final arrested states were found in the whole examined C_w range. The very long waiting times (of the order of months) needed to reach an arrested state in this region of low clay concentrations is the reason why previous studies were interpreting the liquid or sol phase as the stable one. Thus, the liquid or sol phase reported by Mourchid [53] and Tanaka [13] (respectively shown in Fig. 2.14 (a) and (b)) should be replaced by a solid one. Following the complete ergodic to non-ergodic transition by DLS, Ruzicka and coworkers could diferenciate two dinstinct arrested states for low and high Laponite concentrations. Consecutively works, increasing the addition of salt, have been carried out by the same group to find that the picture of these two different regions remains unchanged for $C_s \leq 10^{-3}$ M, being only shifted in the C_w axis [65]. Based on these extensive and systematic investigations, Ruzicka *et al.* proposed a new Laponite phase diagram reported in Fig. 2.15 (a) characterized by two different arrested states IG1, IG2 [64].

The existence of two different non-ergodic states, despite their (still unknown) nature, was at that time enough to clarify some controversies among different

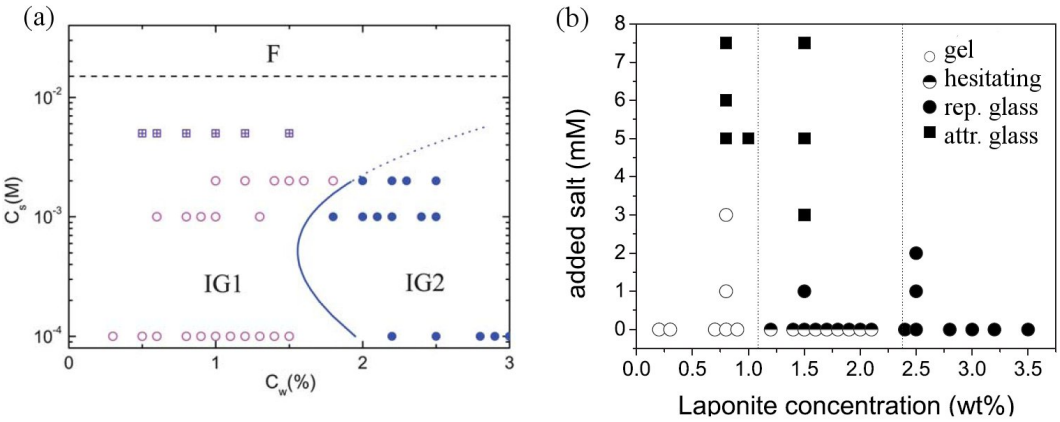

Figure 2.15. (a) Phase diagram proposed by Ruzicka *et al.* [64]. The solid-dashed line separates the two different arrested states IG1 and IG2 respectively for low (open circles) and high (full circles) clay concentrations. For high C_s no clear transition is observed and the nature of the the non-ergodic state is unclear (squares). (b) Phase diagram suggested by Jabbari and coworkers reporting the presence of gel, attractive and repulsive glass [20]. An hesitating state sharing characteristics of both gel and attractive glass is also present in (b).

experimental results. Recalling previous works, the gel structure defended by Nicolai *et al.* was found in samples at region IG1 of Fig. 2.15 (a), while the Wigner glass identified by Bonn and coworkers was in the region IG2. However, further efforts are necessary to give a clear and universal picture of Laponite arrested states, since early results could suffer from non reproducibility due to the non filtration of the samples (issue deeply discussed by Cummins [22]), and regardless of aging (already described previously).

To have a clear signature of the nature of the arrested states, Ruzicka and coworkers performed SAXS measurements following the aging of Laponite suspensions in salt free water, in both high and low concentration regime (IG1 and IG2 regions), up to the formation of the arrested states. They found two different aging evolutions of the static structure factor $S(Q)$ that increases at low Q-values for low C_w while for high C_w it remains stable, Fig. 2.16 (a). This means that aggregates (large structures) are formed only at low clay concentrations. In addition, the peak found at high ($Q \sim 0.15$ nm^{-1}) and low ($Q \gtrsim 0.4$ nm^{-1}) clay concentrations, after the aging evolution, corresponds respectively to a mean length scale of ≈ 40 nm and $\lesssim 15$ nm, which indicates that the particles are mainly disconnected at high C_w and probably bonded in a T-configuration at lower C_w. The latter configuration gives a strong hint to the interpretation of a 'house-of-cards' network proposed for the first time by van Olphen [66].

In agreement with these results obtained by Ruzicka, Jabbari and coworkers performed ensemble-averaged DLS measurements to investigate samples in the clay range of $(0.1 - 3.6\%)$ in ultrapure water, and found the two distinct states at low and high Laponite concentrations [67]. They also classified these two arrested states as gel for low C_w and glass for high C_w. Futhermore, they also found that for intermediate clay concentrations $(1.1 - 2.4\%)$, located in the region of transition

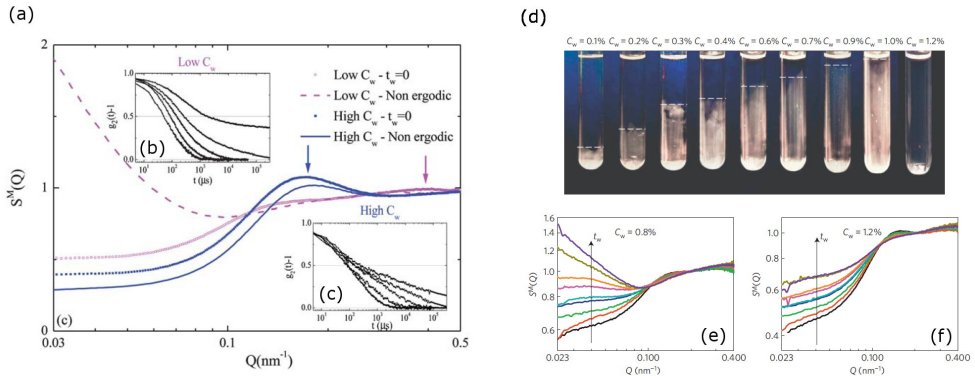

Figure 2.16. Aging evolution of static structure factor $S(Q)$ obtained through SAXS for low and high Laponite concentrations (a). Waiting time dependence of intensity correlation function measured by means of DLS for low (b) and high (c) Laponite suspensions. Photographs of Laponite in salt free water samples in the concentration range of $0.1\% \leq C_w \leq 1.2\%$ showing the presence of phase separation for concentration lower than $C_w = 1.0\%$ and very long waiting time $t_w = 30,000$ h (d). Waiting time evolution of $S(Q)$ for the samples $C_w = 0.8\%$ (e) and $C_w = 1.2\%$ (f) showed in (d) reporting the strong intensity increasing at low Q for (e) compared to (f). Data taken from Refs. [14, 16].

between gel and Wigner glass, the arrest mechanism can give raise to either gel or glass, without a certainty about how the sample is going to evolve. They named these samples as "hesitating" and extended their analysis for different salt concentrations to propose a new phase diagram reproduced in Fig. 2.15 (b) [20].

In two very recent publications Ruzicka *et al.* presented novel experimental evidences that gave a new contribution to the understanding of Laponite systems in absence of added salt in the whole clay concentration window, prior to the nematic transition [15, 16]. In the first publication they combined dilution experiment, *i.e.* addition of water to the arrested samples, with SAXS measurements, theoretical and numerical investigations. With the dilution experiments they confirmed that at low C_w, the arrested structure is characterized by attractive bonds that the added water has not enough energy to break. On the contrary, the addition of water to arrested states obtained at high clay concentrations fluidizes the states, indicating that this structure is due to repulsive interactions. Furthermore, theoretical and numerical calculations based on Yukawa potential were found in complete agreement with $S(Q)$ results from SAXS measurements, implying that in salt free water and high clay concentrations ($C_w \geq 2.0\%$), the system is a Wigner glass [15].

The subsequent work regarded only low clay concentrations ($C_w < 2.0\%$) and extended the time observation window [16]. In this concentration region the system is known to reach a gel arrested state in a timescale of thousand hours. However, for waiting times extremely large (order of years), the authors found that all the samples with $C_w \leq 1.0\%$ show a phase separation composed by a clay-poor and a clay-rich phase. Figure 2.16 (d) shows the photographs of the samples, taken three years after preparation, evidencing these two phases: an upper transparent fluid and an opaque gel on the bottom. More interesting is that for a clay concentration

higher than a threshold ($C_w \approx 1.0\%$) the phase separation compleately disappear, indicating that the system remains indefinitely in a gel state. SAXS measurements for two samples in this region during a period of more than one year show that while the intensity of the static structure factor at low Q is increasing indefinitively for the sample at $C_w = 0.8\%$ (Fig. 2.16 (e)), it saturates for the sample at $C_w = 1.2\%$ (Fig. 2.16 (f)). These results are in agreement with the picture of the phase separation in which, for $C_w \leq 1.0\%$, the gel network reorganizes in a more compact structure and for $C_w > 1.0\%$, a long-time equilibrium structure (stable network) is formed. To support these experimental evidences, Ruzicka *et al.* introduced the patchy model for Laponite systems, already described in section 2.2.3 that is able to reproduce the phase separation found at low clay concentration region ($C_w \leq 1.0\%$) and the equilibrium gel for $1.0\% < C_w < 2.0\%$.

Combining all reasonable experimental and theoretical results obtained so far and claiming for a rigid protocol of sample preparation, to increase the reproducibility of the results, Ruzicka and coworkers proposed the most complete, up to date, phase diagram for Laponite suspension reproduced in Fig. 2.17 [14]. They considered the waiting time to be sufficiently long in order to have no additional (macroscopic) changes in the samples state behavior. To construct this phase diagram, arrested structures suggested by different authors and studied by different techniques have been taken into account.

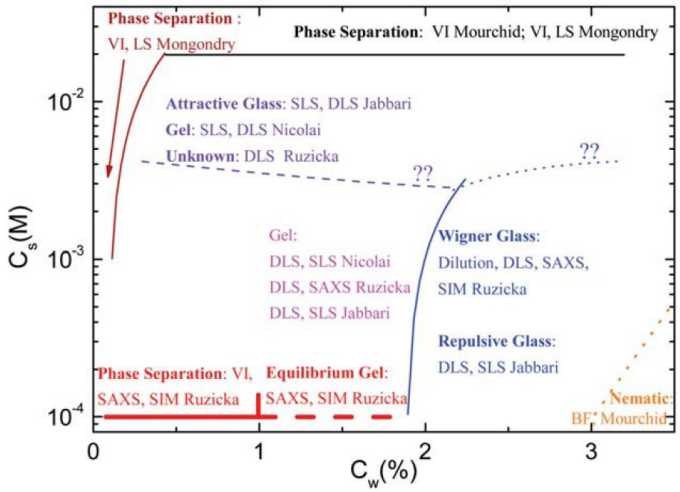

Figure 2.17. New phase diagram proposed by Ruzicka *et al.* combining the experimental and theoretical results from different authors. Each experimental technique used is displayed by initials, and SIM stands for numerical simulations [14].

In salt free water conditions ($C_s = 10^{-4}$ M) there exist four regions, depending on clay concentration: for $0.1\% \leq C_w \leq 1.0\%$ phase separation was found by Ruzicka [16]; for $1.0\% < C_w < 2.0\%$ gel was found by Nicolai, Jabbari and Ruzicka [12, 20, 68] and afterwards interpreted as a true equilibrium gel by Ruzicka [16]; for $2.0\% \leq C_w < 3.0\%$ a Wigner glass region was suggested by Ruzicka [15] although Jabbari *et al.* simply described it by repulsive glass [20]; finally for $C_w > 3.0\%$ a nematic phase was evidenced by Mourchid [10, 50, 53]. By increasing salt concentration, evidence of two different non-ergodic states for low and high

clay concentration (gel and glass respectively) are found up to $C_s = 2 \times 10^{-3}$ M. For $C_s \geq 3 \times 10^{-3}$ M, the high clay concentration region has not been extensively investigated, due to the immediate arrest of the sample during preparation. Lower clay concentrations in this region were found to be an attactive glass by Jabbari *et al.* [20], due to the dual features of light scattering data resembling both gel and glasses, and a gel by Nicolai *et al.* [61]. The results of Ruzicka and coworkers are not conclusive in this range of clay and salt concentrations [65]. For very low clay concentrations ($C_w < 0.3\%$), Mongondry *et al.* [12] found evidences of a phase separation region, which develops with waiting time, in a wide range of salt concentrations down to $C_s = 10^{-3}$ M. Finally, for salt concentrations higher than $C_s = 2 \times 10^{-2}$ M phase separation in form of flocculation or sedimentation of large aggregates was observed by Mourchid *et al.* [53] by means of visual inspection (VI) and by the group of Mongondry [12] using both VI and light scattering (LS).

This recent phase diagram depicts the complexity of Laponite systems caused by the competition between the attractive and repulsive interactions. Although all decennial experiments on the system have been done, there are still several points to be clarified in order to have a real comprehension about the arrested states of Laponite systems (see Ref. [14]).

Chapter 3

Experimental Section

The experimental methods used in this work to investigate the Q-dependence of the aging of a charged colloidal suspension and its modification with H_2O/D_2O isotopic substitution are Dynamic Light Scattering (DLS), X-ray Photon Correlation Spectroscopy (XPCS), Neutron Spin Echo (NSE) and Small Angle X-ray Scattering (SAXS). In this chapter the basic theory of light scattering and the working mechanisms of each technique, clarifying which informations can be obtained by their use will be discussed. A special attention will be dedicated to the explanation of the multi angle DLS setup, built during this thesis, with a detailed description of the alignment procedure. Finally the sample procedure used during this work will be described.

3.1 Dynamic Light Scattering

3.1.1 Basic Theory of Light Scattering

Electromagnetic radiation is one of the most powerful probes of the structure and dynamics of matter. When photons interact with a molecule they can either donate or receive energy from the translational, rotational, vibrational and electronic degrees of freedom. The scattered light thereby experiences frequency shifts related to the degrees of freedom of the particles. In the case of scattering techniques used in this thesis we deal with light scattered only from translational and rotational degrees of freedom, which means that the energy (and therefore the wavelength) of the incident photon is conserved (Rayleigh scattering) and only its direction is changed.

The scattering experiment is based on an incident beam of particles or radiation that impinges on a sample and is consequently scattered by its microscopic structures. When electromagnetic radiation interacts with matter, the electric field induces an oscillating polarization of the electrons in the molecules that consequently act as a secondary source of radiation. The frequency shifts, the angular distribution, the polarization, and the intensity of the scattered light encode informations about the size, shape, and molecular interactions of the scattering material. Thus, with the aid of the electrodynamics and the theory of the time-dependent statistical mechanics, one can extract structure and dynamic informations of the particles from the scattered light.

The top view of a typical scattering experiment is shown in Fig. 3.1 (a). The light emitted from a laser passes through a polarizer (that define the polarization of the incident beam), and then impinges on the sample (the scattering medium). The major part of the radiation passes through the sample unaffected, while just a small part is scattered. The scattering intensity ($I_s(\mathbf{Q}, t)$) is measured by a detector placed at an angle θ between the incident beam and the scattered light. In Fig. 3.1, the region of the sample formed by the overlap between the incident beam and the region "seen" by the detector defines a volume V called "scattering volume". Typically, in a light scattering setup, the dimensions of the scattering volume can be controlled by apertures, slits, walls of the sample's container, or by optics such as lenses.

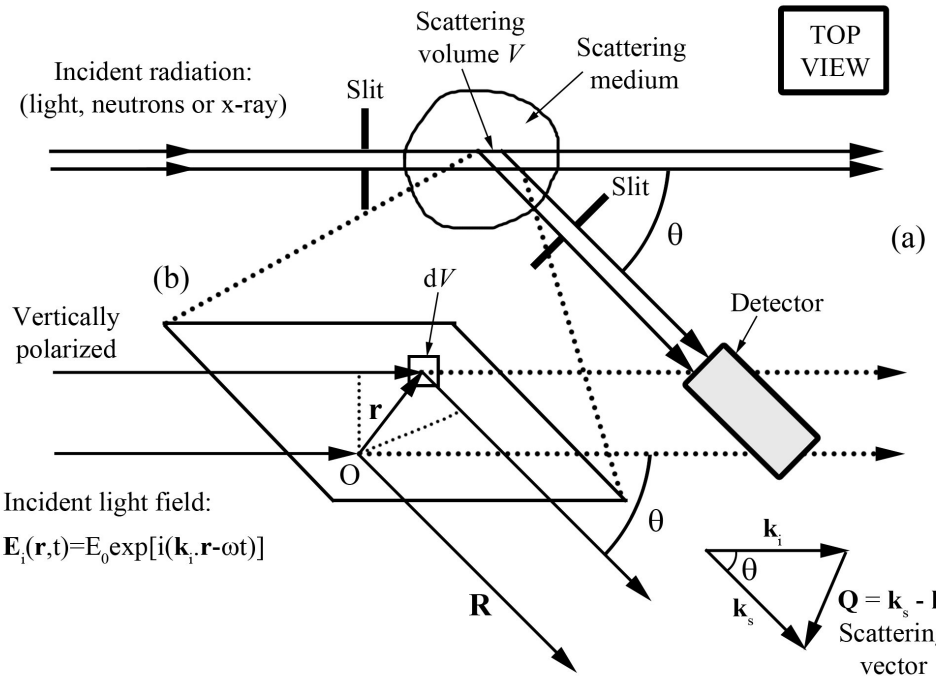

Figure 3.1. (a) Top view of a typical light-scattering experiment. (b) Expanded view of the scattering volume, showing rays scattered at the origin O and by a volume element dV at position $\mathbf{r}$.

In Fig. 3.1 the source is a monochromatic beam of laser light with the electric field component at position $\mathbf{r}$ and time t given by $\mathbf{E}_i(\mathbf{r}, t)$. The incident light can be considered as a plane-wave, well described by:

$$\mathbf{E}_i(\mathbf{r}, t) = \mathbf{p}_i E_0 e^{i(\mathbf{k}_i \cdot \mathbf{r} - \omega_i t)}, \tag{3.1}$$

where $\mathbf{p}_i$ is the polarization, E_0 is the amplitude, $\mathbf{k}_i$ is the propagation vector, and ω_i is the angular frequency of the incident electric field. Here the magnitude of the propagation vector is given by $|\mathbf{k}_i| = k_i = 2\pi n/\lambda$ with λ being the wavelength of light and n the refractive index of the scattering medium. This plane wave is incident on a medium with a local dielectric constant

$$\boldsymbol{\varepsilon}(\mathbf{r},t) = \varepsilon_0 \mathbf{I} + \delta\boldsymbol{\varepsilon}(\mathbf{r},t), \tag{3.2}$$

where $\delta\boldsymbol{\varepsilon}(\mathbf{r},t)$ is the dielectric constant fluctuation tensor at position $\mathbf{r}$ and time t, ε_0 is the average dielectric constant of the medium and $\mathbf{I}$ is the second-order unit tensor.

We assume that the scattering of the light that passes through the sample is weak, so that:

1. most photons pass through the sample undeviated, few of them are scattered only once and the probability of double and high-order scattering events, both within the particle and between distinct particles, is negligible;

2. the incident beam is not significantly distorted from the medium. (This corresponds to the first Born approximation or, in the specific context of light scattering, to the so-called Rayleigh-Gans-Debye approximation);

3. the scattering process is "quasielastic", implying only a very small change in frequency. Thus the magnitude of the propagation vector $\mathbf{k}_s$ of the scattered light is also $2\pi n/\lambda$.

Furthermore we assume that the phase of the incident field is simply related to the position $\mathbf{r}$ in space as $2\pi\mathbf{r}\cdot\mathbf{k}_i/(|\mathbf{k}_i|\lambda)$. The refractive index of the particles is generally different from that of the surrounding fluid, so that the wavelength of the light inside the particle and the fluid differ. Therefore the phase difference between the electric field that traverses a particle and the fluid is equal to $2\pi[\frac{a}{\lambda_p} - \frac{a}{\lambda_f}]$, where a is the radius of the particle and $\lambda_p(\lambda_f)$ the wavelength of the light in the particle (fluid). If λ_0 denotes the wavelength of the light in vacuum, $\lambda_p = \lambda_0/n_p$ and $\lambda_f = \lambda_0/n_f$, with $n_p(n_f)$ being the refractive index of the particle (fluid). In this case the phase difference is equal to $2\pi[n_p - n_f]\frac{a}{\lambda_0}$. Equation (3.1) is a good approximation only if the phase shift is small, *i.e.*

$$2\pi[n_p - n_f]\frac{a}{\lambda_0} \ll 1. \tag{3.3}$$

In the following, we will also consider the direction of the incident field to be the same everywhere in the scattering volume. Refraction of light at the interface fluid/particle is thus neglected and this is justified when $|n_p - n_f| \ll 1$.

By applying the Maxwell's equations to the problem of a plane electromagnetic wave propagating in a medium with a local dielectric constant given by Eq. (3.2), we have that the amplitude $E_s(\mathbf{R},t)$ of the electric field of the radiation scattered to a point detector at position $\mathbf{R}$ in the far field is given by

$$E_s(\mathbf{R},t) = \frac{E_0}{4\pi\varepsilon_0}\frac{e^{i(k_s R-\omega_i t)}}{R}\int_V e^{-i\mathbf{Q}\cdot\mathbf{r}}[\mathbf{p}_s\cdot[\mathbf{k}_s\times(\mathbf{k}_s\times(\delta\boldsymbol{\varepsilon}(\mathbf{r},t)\cdot\mathbf{p}_i))]]d^3\mathbf{r}, \tag{3.4}$$

where V indicates that the integral is over the scattering volume, $\mathbf{Q}$ is defined as the difference between the incident and scattered propagation vector ($\mathbf{Q} = \mathbf{k}_s - \mathbf{k}_i$) and $\mathbf{p}_s$ is the polarization of the scattered electric field. Here we simply quote the

result of the scattered electric field, details of this derivation are given, for example, in Ref. [69].

Since we are assuming a quasielastic scattering process, we have that the wavelength of the incident light is changed very little, so that $|\mathbf{k}_i| \cong |\mathbf{k}_s|$. Thus, the triangle in Fig. 3.1 is isosceles and the magnitude of $\mathbf{Q}$ can be found from the law of cosines,

$$\begin{aligned} Q^2 &= |\mathbf{k}_s - \mathbf{k}_i|^2 = k_s^2 + k_i^2 - 2\mathbf{k}_i \cdot \mathbf{k}_s = 2k_i^2 - k_i^2 \cos(\theta) = 4k_i^2 \sin^2\left(\frac{\theta}{2}\right) \\ |\mathbf{Q}| &= 2k_i \sin\left(\frac{\theta}{2}\right) = \frac{4\pi n}{\lambda} \sin\left(\frac{\theta}{2}\right), \end{aligned} \tag{3.5}$$

where θ is the scattering angle formed by the directions of the incident and scattered fields.

With the help of the identity $a \times (b \times c) = b(a \cdot c) - c(a \cdot b)$, Eq. (3.4) can be simplified to:

$$E_s(\mathbf{R}, t) = -\frac{k_s^2 E_0}{4\pi\varepsilon_0} \frac{e^{i(k_s R - \omega_i t)}}{R} \int_V e^{-i\mathbf{Q}\cdot\mathbf{r}} \delta\varepsilon_{is}(\mathbf{r}, t) d^3\mathbf{r}, \tag{3.6}$$

where

$$\delta\varepsilon_{is}(\mathbf{r}, t) \equiv \mathbf{p}_s \cdot \delta\boldsymbol{\varepsilon}(\mathbf{r}, t) \cdot \mathbf{p}_i \tag{3.7}$$

is the component of the dielectric constant fluctuation tensor along the initial and final polarization directions.

Equation (3.6) can be rewritten as the sum of the amplitudes of the fields $dE_s(\mathbf{R}, t)$ scattered by volume elements $dV \equiv d^3r$ at position $\mathbf{r}$:

$$E_s(\mathbf{R}, t) = \int_V dE_s(\mathbf{R}, t), \tag{3.8}$$

where

$$dE_s(\mathbf{R}, t) = -\frac{k_s^2 E_0}{4\pi\varepsilon_0} \frac{e^{i(k_s R - \omega_i t)}}{R} e^{-i\mathbf{Q}\cdot\mathbf{r}} \delta\varepsilon_{is}(\mathbf{r}, t) d^3\mathbf{r}. \tag{3.9}$$

Equation (3.9) can be recognized as the expression describing the radiation due to an oscillating point dipole. The incident electric field, of strength E_0 and propagation vector k_s, induces in the volume element dV at position $\mathbf{r}$ a dipole moment of strength proportional to $E_0 \delta\varepsilon_{is}(\mathbf{r}, t)$ which oscillates at angular frequency ω_i. This elementary dipole radiates, or scatters, light in all directions. The second factor in Eq. (3.9) describes a spherical wave of scattered radiation emanating from the origin O. Finally, the term $\exp(-i\mathbf{Q} \cdot \mathbf{r})$, takes into account that the radiation scattered by the volume element at position $\mathbf{r}$ is shifted in space relative to that scattered by an element at the origin O. Referring to Fig. 3.1 (b), simple geometry shows that the extra distance traveled by the light scattered at $\mathbf{r}$, compared to that scattered at O, is $\mathbf{k_i} \cdot \mathbf{r} - \mathbf{k_s} \cdot \mathbf{r}/k$ which, by using Eq. (3.5), gives a phase shift of $-\mathbf{Q} \cdot \mathbf{r}$ radians.

Equation (3.4) embodies the fundamental physics of light scattering. The scattered light field consists of a spherical wave emanating from the scattering volume with an angle- or Q-dependent amplitude which is the spatial Fourier transform of instantaneous variations in the dielectric constant of the sample. In fact, from Eq. (3.4) it is evident that if the medium is totally homogeneous, *i.e.* $\delta\boldsymbol{\varepsilon}(\mathbf{r},t)=0$, there is no scattering. In other words, scattering of radiation (for $Q\neq 0$) is caused by spatial fluctuations in the dielectric properties of the medium. As described afterwards the intensity of the scattering, averaged over time, provides information on the sample's structure, essentially on spatial correlations of the particles. Any variation in time of the local dielectric constant is directly reflected in temporal variations of the amplitude and intensity of the scattered field. Light scattering therefore probes directly the structure and dynamics of a sample in reciprocal space (or Q space).

The scattering expressions shown up to here (Eqs. (3.4), (3.6) and (3.9)) have been written in general tensor notation and hence are independent of any specific laboratory coordinate system used for a scattering experiment. However, for a reason of clarity, it is convenient to proceed the mathematical description of light scattering assuming only polarized scattering electric field and considering that the dielectric behavior of the medium is scalar rather than tensorial. Moreover, the main expressions related to the depolarized scattering electric field will be pointed out.

Discrete Scatterers

We now consider the case of a sample containing discrete scattering particles suspended in a liquid. Let's assume N suspended particles in the scattering volume V whose centers of mass at time t are described by position vectors $\{\mathbf{R}_j(t)\}$. By considering only the polarized component of the scattered light and the dielectric constant to be scalar, if $\mathbf{r}_j(t)$ is the position of volume element ($dV_j = d^3r_j$) in particle j relative to its center of mass (see Fig. 3.2), after some calculations [70], Eq. (3.6) becomes:

$$E_s(\mathbf{R},t)=-\frac{k_s^2E_0}{4\pi}\frac{e^{i(k_sR-\omega_it)}}{R}\times\sum_j\left\{\int_V\left[\frac{\varepsilon_P(\mathbf{r_j},t)-\varepsilon_L}{\varepsilon_0}\right]e^{-i\mathbf{Q}\cdot\mathbf{r}_j}d^3\mathbf{r}_j\right\}e^{-i\mathbf{Q}\cdot\mathbf{R}_j(t)}, \tag{3.10}$$

or

$$E_s(\mathbf{R},t)=-E_0\frac{e^{i(k_sR-\omega_it)}}{R}\times\sum_j\left[\int_V\Delta\rho(\mathbf{r}_j,t)e^{-i\mathbf{Q}\cdot\mathbf{r}_j}d^3\mathbf{r}_j\right]e^{-i\mathbf{Q}\cdot\mathbf{R}_j(t)}. \tag{3.11}$$

Here V_j is the volume of particle j and $\Delta\rho(\mathbf{r}_j,t)$ is defined by

$$\Delta\rho(\mathbf{r}_j,t)=\frac{k_s^2}{4\pi}\left[\frac{\varepsilon_P(\mathbf{r}_j,t)-\varepsilon_L}{\varepsilon_0}\right], \tag{3.12}$$

where $\varepsilon_P(\mathbf{r}_j,t)$ is the local dielectric constant at position $\mathbf{r}_j$ in particle j, ε_L is the average dielectric constant of the liquid and ε_0 is, as before, the average dielectric constant of the whole suspension.

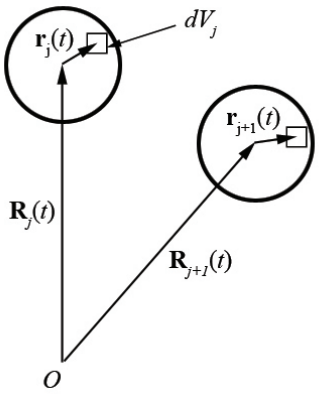

Figure 3.2. Co-ordinates for discrete scatterers. Relative to an arbitrary origin O, $\mathbf{R}_j(t)$ is the position of the center of mass of particle j at time t and $\mathbf{r}_j(t)$ is the position of volume element dV_j in particle j, relative to its center of mass.

From the derived expression it is clear how the strength of the scattering depends on the difference between the dielectric properties of the particle and of the liquid, since we have assumed that the "background" scattering due to spontaneous fluctuations in the liquid itself is negligible. The quantity $\Delta\rho(\mathbf{r}_j, t)$ can be regarded as a measure of the local "density of scattering material".
Eq. (3.11) can be rewritten as

$$E_s(\mathbf{R}, t) = -E_0 \frac{e^{i(k_s R - \omega_i t)}}{R} \sum_j b_j(\mathbf{Q}, t) e^{-i\mathbf{Q}\cdot\mathbf{R}_j(t)}, \tag{3.13}$$

where we have defined the "scattering length" of particle j by

$$b_j(\mathbf{Q}, t) = \int_{V_j} \Delta\rho(\mathbf{r}_j, t) e^{-i\mathbf{Q}\cdot\mathbf{r}_j} d^3\mathbf{r}_j. \tag{3.14}$$

From Eq. (3.14) we see that the local total scattered electric field is the sum of the fields scattered by the individual particles. Each of these is the product of a scattering length, determined by the instantaneous distribution of material within the particle, and a phase factor determined by the instantaneous position of the particles in the sample. Usually in light scattering techniques, the scattered intensity rather than the electric field is directly measured. Since the intensity and fields are related by $I(\mathbf{Q}, t) = |E(\mathbf{Q}, t)|^2 = E(\mathbf{Q}, t)E^*(\mathbf{Q}, t)$, from Eq. (3.13) one can easily get an expression for the instantaneous scattered intensity:

$$I_s(\mathbf{Q}, t) = \frac{E_0^2}{R^2} \sum_{j=1}^{N} \sum_{k=1}^{N} b_j(\mathbf{Q}, t) b_k^*(\mathbf{Q}, t) e^{-i\mathbf{Q}\cdot[\mathbf{R}_j(t) - \mathbf{R}_k(t)]}. \tag{3.15}$$

Structural information can be obtained by the ensemble average, indicated by $\langle \ldots \rangle$, of this intensity (equivalent to a time average if the scattering medium is ergodic)

$$\langle I_s(Q) \rangle = \frac{E_0^2}{R^2} \left\langle \sum_{j=1}^{N} \sum_{k=1}^{N} b_j(\mathbf{Q}) b_k^*(\mathbf{Q}) e^{-i\mathbf{Q}\cdot(\mathbf{R}_j - \mathbf{R}_k)} \right\rangle. \tag{3.16}$$

By writing the averaged scattered intensity as a function of the modulus Q of the scattered vector, we have assumed the sample to be on average spatially isotropic, as expected for a "liquid-like" dispersion or solution. Therefore, Eq. (3.16) represents the general result for the averaged intensity scattered by an assembly of discrete particles in some simple cases.

Dilute Systems

In dilute systems the individual particles are, on average, widely spatially separated so that their behaviors are uncorrelated. Omitting for simplicity the pre-factors, Eq. (3.16) can be written in the form:

$$\left\langle I_s(\mathbf{Q},t)\right\rangle = \sum_{j=1}^{N}\left\langle |b_j(\mathbf{Q},t)|^2\right\rangle + \sum_{j=1}^{N}\sum_{k=1}^{N}\left\langle b_j(\mathbf{Q},t)e^{-i\mathbf{Q}\cdot(\mathbf{R}_j(t))}\right\rangle\left\langle b_k^*(\mathbf{Q},t)e^{-i\mathbf{Q}\cdot(\mathbf{R}_k(t))}\right\rangle. \tag{3.17}$$

Since, over time, particle j can take up any position in the sample, unaffected by the position of the others, the exponential factors can be considered randomly distributed around zero and $\langle b_j(\mathbf{Q},t)\exp(-i\mathbf{Q}\cdot\mathbf{R}_j(t))\rangle = 0$. Therefore, in the dilute limit, the averaged scattered intensity is just the sum of the averaged intensities scattered by the individual particles.

Considering that the averaged intensity scattered by identical particles are the same, Eq. (3.17) becomes:

$$\left\langle I_s(Q)\right\rangle = N\left\langle |b(\mathbf{Q})|^2\right\rangle \tag{3.18}$$

and can be rewritten as

$$\langle I_s(Q)\rangle = N\langle |b(\mathbf{0})|^2 P(\mathbf{Q})\rangle \quad \text{with} \quad P(\mathbf{Q}) = \frac{\langle |b(\mathbf{Q})|^2\rangle}{\langle |b(0)|^2\rangle}. \tag{3.19}$$

Here, $P(\mathbf{Q})$ is called the *form factor* of the particle and is defined in such a way that $P(\mathbf{Q}) \to 1$ as $Q \to 0$. It gives information on the size, structure and shape of the particles, averaged over orientation and over any distribution of size and shape.

To investigate the properties of the fluctuating scattered field we consider the simple situation of a dilute suspension of identical spherical particles. In this case the scattering lengths $b_j(\mathbf{Q},t)$ have the same time-independent value $b(\mathbf{Q})$, and can therefore be taken outside the sum in Eq. (3.13), giving a total scattered field:

$$E_s(\mathbf{Q},t) = \sum_{j}^{N} e^{-i\mathbf{Q}\cdot\mathbf{R}_j(t)}. \tag{3.20}$$

Since DLS deals with normalized quantities, we have neglected the pre-factors in Eq. (3.20). The total scattered field $E_s(\mathbf{Q},t)$ is the (vectorial) sum of the individual vectors $\exp(-i\mathbf{Q}\cdot\mathbf{R}_j(t))$ forming an angle $\mathbf{Q}\cdot\mathbf{R}_j(t)$ with the real axis. Since the particles are randomly distributed throughout the sample, the phase angles are randomly distributed between 0 and 2π and thus the field $E_s(\mathbf{Q},t)$ can be represented pictorially as a two-dimensional random walk of N vectors. Due to the Brownian motion of the particles, positions $\mathbf{R}_j(t)$ and phase angles $\{\mathbf{Q}\cdot\mathbf{R}_j(t)\}$ change and the

total scattered field has fluctuations which become totally uncorrelated over times so that the phase angles change by $\sim 2\pi$. In such conditions, the average value of the scattered field is:

$$\left\langle E_s(\mathbf{Q},t)\right\rangle = \sum_{j=1}^{N}\left\langle e^{-i\mathbf{Q}\cdot\mathbf{R}_j(t)}\right\rangle = 0. \tag{3.21}$$

In addition, the average of the scattered intensity becomes:

$$\begin{aligned}\left\langle I_s(\mathbf{Q},t)\right\rangle &= \left\langle |E(\mathbf{Q},t)|^2\right\rangle = \sum_{j=1}^{N}\sum_{k=1}^{N}\left\langle e^{-i\mathbf{Q}\cdot[\mathbf{R}_j(t)-\mathbf{R}_k(t)]}\right\rangle \\ &= \sum_{j} 1 + \sum_{j\neq k}\left\langle e^{-i\mathbf{Q}\cdot\mathbf{R}_j(t)}\right\rangle\left\langle e^{-i\mathbf{Q}\cdot\mathbf{R}_k(t)}\right\rangle = N,\end{aligned} \tag{3.22}$$

where, in averaging the cross-terms separately, we have exploited the assumption that the suspension is dilute so that the particles position are uncorrelated. Equations (3.21) and (3.22) reflects the well-known results from the random walk, *i.e.* the mean value is zero since the walk is, on average, symmetrical about the origin and the mean-square displacement is proportional to the number of steps.

Concentrated Systems

Now we consider the general expression for the averaged intensity scattered by an ensemble of discrete particles (Eq. (3.17)). For simplicity we first assume the particles to be homogeneous identical spheres, so that all $b_j(\mathbf{Q}) = b(Q)$. The use of Eq. (3.19) gives

$$\langle I_s(Q,t)\rangle = Nb(0)^2P(Q)S(Q), \tag{3.23}$$

where $S(Q)$ is the "static structure factor", defined by

$$S(Q) \equiv \frac{1}{N}\sum_{j=1}^{N}\sum_{k=1}^{N}\left\langle e^{-i\mathbf{Q}\cdot(\mathbf{R}_j(t)-\mathbf{R}_k(t))}\right\rangle. \tag{3.24}$$

In Eq. (3.23) the products $Nb(0)^2P(Q)S(Q)$ describe the scattering by N uncorrelated particles and the structure factor represents the modifications of the intensity due to the spatial correlations of the particles. Clearly, in a dilute system where particle positions are uncorrelated, cross terms ($i \neq j$) in Eq. (3.24) vanish and $S(Q) = 1$.

3.1.2 Correlation Functions

Consider a scattering medium, such as a suspension of colloidal particles, illuminated by coherent light. At any instant, the far-field pattern of scattered light is constituted by a grainy random diffraction, or "speckle" pattern (Fig. 3.3 (a)). The interference of phases of light scattered by individual particles yields to regions of large and small intensities. Furthermore, as the scattering medium is constantly changing with time, since particle positions $\mathbf{R}_j(t)$ change for Brownian motion, the phase changes, and

the speckle pattern fluctuates from one random configuration to another. Thus, as sketched in Fig. 3.3 (b), the scattered intensity $I_s(\mathbf{Q}, t)$, relative to a certain point in the far field, fluctuates randomly in time. These fluctuations contain important structural and dynamical information about the positions and orientations of the particles. For example, at the simplest level, faster the particles move, more rapidly the intensity fluctuates.

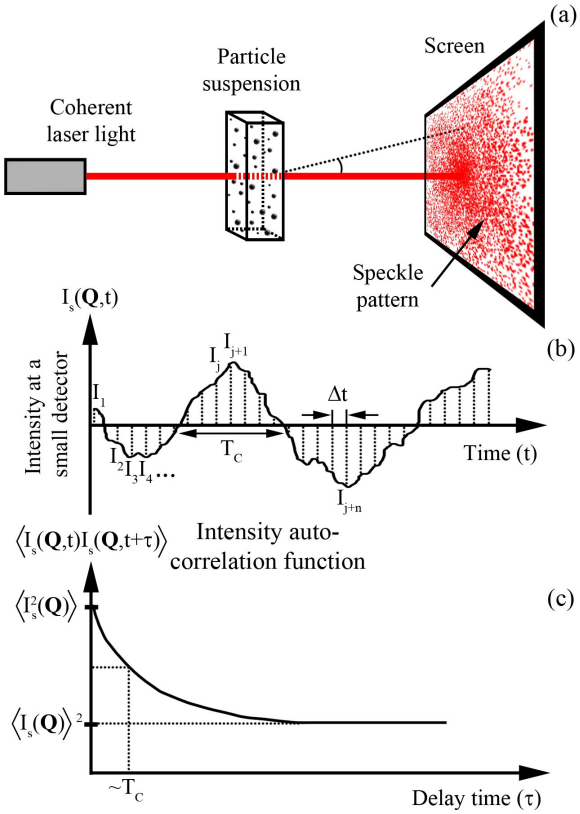

Figure 3.3. (a) Coherent (laser) light scattered by a random medium such as a suspension of colloidal particles gives rise to a random diffraction pattern, or speckle, in the far field. (b) Fluctuating intensity observed at a detector with the size of about one speckle. (c) Time-dependent part of the correlation function decays with a time constant T_C equal to the typical fluctuation time of the scattered light.

In order to extract useful information from a fluctuating intensity one can perform a simply time average

$$\langle I_s(\mathbf{Q}, t_0, T)\rangle = \frac{1}{T}\int_{t_0}^{t_0+T} I_s(\mathbf{Q}, t)dt, \tag{3.25}$$

where t_0 is the time at which the measurement was initiated and T is the time over which it is averaged. The average becomes meaningful only if T is large compared to the period of fluctuation. Actually in the ideal experiment the average would be done over an infinite time

$$\langle I_s(\mathbf{Q}, t_0)\rangle = \lim_{T\to\infty} \frac{1}{T} \int_{t_0}^{t_0+T} I_s(\mathbf{Q}, t)dt. \tag{3.26}$$

Under general conditions it can be shown that this infinite time average is independent of t_0 [69]. In Fig. 3.3 (b) it is possible to observe that the intensity fluctuates around its time average, thus, thanks to its independence on t_0, Eq. (3.26) can be expressed as:

$$\langle I_s\rangle = \lim_{T\to\infty} \frac{1}{T} \int_{0}^{T} I_s(\mathbf{Q}, t)dt. \tag{3.27}$$

Due to the fluctuations of I_s, generally the intensity of the scattered light at two different instants (t and $t+\tau$) will give two different values ($I_s(\mathbf{Q}, t) \neq I_s(\mathbf{Q}, t+\tau)$). Nevertheless when τ is very small compared to the times scale of a single fluctuation (T_C), $I_s(\mathbf{Q}, t)$ will be very close to $I_s(\mathbf{Q}, t+\tau)$. On the other hand, as τ increases, the deviation of $I_s(\mathbf{Q}, t)$ from $I_s(\mathbf{Q}, t+\tau)$ will be different from zero. Therefore, the value of $I_s(\mathbf{Q}, t)$ is correlated with $I_s(\mathbf{Q}, t+\tau)$ when τ is small and the correlation is lost as τ becomes large compared to the typical fluctuation time of the system. A measure of this correlation is the intensity autocorrelation function which is defined as

$$\langle I_s(\mathbf{Q}, 0)I_s(\mathbf{Q}, \tau)\rangle = \lim_{T\to\infty} \frac{1}{T} \int_{0}^{T} I_s(\mathbf{Q}, t)I_s(\mathbf{Q}, t+\tau)dt. \tag{3.28}$$

Now it is important to demonstrate how the time-correlation function changes with time. At zero delay Eq. (3.28) reduces to

$$\lim_{\tau\to 0}\langle I_s(\mathbf{Q}, 0)I_s(\mathbf{Q}, \tau)\rangle = \langle I_s^2(\mathbf{Q})\rangle. \tag{3.29}$$

For delay times much greater than the typical fluctuation time of the intensity (T_C), fluctuations in $I_s(\mathbf{Q}, t)$ and $I_s(\mathbf{Q}, t+\tau)$ are uncorrelated so that the average in Eq. (3.28) can be separated

$$\lim_{\tau\to\infty}\langle I_s(\mathbf{Q}, 0)I_s(\mathbf{Q}, \tau)\rangle = \langle I_s(\mathbf{Q})\rangle\langle I_s(\mathbf{Q}, \tau)\rangle = \langle I_s(\mathbf{Q})\rangle^2. \tag{3.30}$$

Since $\langle I_s^2(\mathbf{Q})\rangle \geq \langle I_s(\mathbf{Q})\rangle^2$, if I_s is a constant of the motion (a conserved quantity), the autocorrelation function either remains equal to its initial value for all times τ, or it decays from its initial value which is the maximum. The scattered intensity $I_s(\mathbf{Q}, t)$ is a nonconserved and nonperiodic property of the system, therefore the intensity correlation function decays from the mean of the squared intensity $\langle I_s^2(\mathbf{Q})\rangle$ at small delay times to the square of the mean intensity $\langle I_s(\mathbf{Q})\rangle^2$ at long times. The characteristic time of this decay is a measure of the typical fluctuation time of the intensity (T_C in Fig. 3.3 (b) and (c)).

Suppose that the time axis is divided into discrete intervals Δt as shown in Fig. 3.3 (b), *i.e.* $t = j\Delta t$, $\tau = n\Delta t$, $T = N\Delta t$ and $t+\tau = (j+n)\Delta t$. Moreover, let's suppose that the intensity $I_s(\mathbf{Q}, t)$ does not change significantly over the time interval Δt. From the definition of integral Eqs. (3.27) and (3.28) can be approximated by:

$$\begin{aligned} \langle I_s \rangle &\cong \lim_{N\to\infty} \frac{1}{N} \sum_{j=1}^{N} I_j \\ \langle I_s(\mathbf{Q},0) I_s(\mathbf{Q},\tau) \rangle &\cong \lim_{N\to\infty} \frac{1}{N} \sum_{j=1}^{N} I_j I_{j+n}, \end{aligned} \tag{3.31}$$

where I_j is the scattering intensity at the beginning of the j^{th} interval. These sums become better approximations to the infinite time averages as $\Delta t \to 0$. Normally, this discrete expression is used in order to compute the time-correlation functions in light scattering experiments.

3.1.3 Dynamic Light Scattering Measurements

The Dynamic Light Scattering (DLS) setup used in this work is based in the homodyne method where the time correlation function of the scattered intensity $I_s(\mathbf{Q},t) = |E_s(\mathbf{Q},t)|^2$ is measured. The normalized autocorrelation function of the intensity is defined as

$$g^{(2)}(\mathbf{Q},\tau) \equiv \frac{\langle I_s(\mathbf{Q},0) I_s(\mathbf{Q},\tau) \rangle}{\langle I_s(\mathbf{Q},0) \rangle^2}. \tag{3.32}$$

In the homodyne setup only the scattered light impinges on the detector. Otherwise, in the heterodyne setup a small portion of the incident beam (called local oscillator) is mixed with the scattered light. The sum of these two interfering fields $E_{LO}(t) + E_s(\mathbf{Q},t)$, where $E_{LO}(t)$ stands for the Q-independent local oscillator, hits the detector surface and the time correlation function of the collected intensity $I_{he}(\mathbf{Q},t) = |E_{LO}(t) + E_s(\mathbf{Q},t)|^2$ is recorded. In this case the normalized time correlation function of the scattered field defined as:

$$g^{(1)}(\mathbf{Q},\tau) \equiv \frac{\langle E_s(\mathbf{Q},0) E_s^*(\mathbf{Q},\tau) \rangle}{I_s(\mathbf{Q})} \tag{3.33}$$

can be directly measured. Homodyne and heterodyne techniques yield different information on the system's dynamics which are intrinsically related one with each other as described in the following.

Substituting Eq. (3.20) into Eq. (3.33), and using similar manipulations as those which led to Eq. (3.22), yields

$$\begin{aligned} g^{(1)}(\mathbf{Q},\tau) &= N^{-1} \sum_j \left\langle e^{-i\mathbf{Q}\cdot[\mathbf{R}_j(0)-\mathbf{R}_j(\tau)]} \right\rangle \\ &= \left\langle e^{-i\mathbf{Q}\cdot[\mathbf{R}(0)-\mathbf{R}(\tau)]} \right\rangle. \end{aligned} \tag{3.34}$$

Last step follows from the fact that the average motions of identical particles are equal.

Now regarding the time correlation function of the scattered intensity, the use of Eq. (3.20) permits to obtain

$$\begin{aligned}\left\langle I_s(\mathbf{Q},0)I_s(\mathbf{Q},\tau)\right\rangle &= \sum_{j,k,l,m}\left\langle e^{-i\mathbf{Q}\cdot[\mathbf{R}_j(0)-\mathbf{R}_k(0)+\mathbf{R}_l(\tau)-\mathbf{R}_m(\tau)]}\right\rangle \\ &= N^2+N^2|\left\langle e^{-i\mathbf{Q}\cdot[\mathbf{R}(0)-\mathbf{R}(\tau)]}\right\rangle|^2,\end{aligned} \tag{3.35}$$

where the independence of particle positions in a dilute suspension and the limit $N\to\infty$ have been considered.

Using the definition of the normalized time correlation function $g^{(2)}(\mathbf{Q},\tau)$ (Eq. (3.32)), together with Eqs. (3.33), (3.22), (3.34) and (3.35) we obtain that

$$g^{(2)}(\mathbf{Q},t)=1+[g^{(1)}(\mathbf{Q},t)]^2. \tag{3.36}$$

This result, called "Siegert relation", reflects the factorization properties of the correlation functions of a complex Gaussian variable. It can be shown that the above equation is valid even when the hypotheses of Gaussian distribution of the diffuse field $E_s(\mathbf{Q},t)$ is not verified, due to a non ideal incident beam or to non-independent scattered fields.

Moreover, although Eq. (3.36) was derived by considering the absence of spatial correlations, it is applicable to any fluid system in which the range of spatial correlations is much smaller than the linear dimension of the scattering volume. Then the scattering volume contains a large number of "correlation volumes", *i.e.*, region where particle positions are correlated, and the derivation proceeds essentially in the same way with correlation volumes taking the role of the independent particles [71]. Thus Eq. (3.36) also applies, for example, to a suspension of interacting, non-identical, non spherical and/or flexible particles. It can be shown that, in this case, the field correlation function $g^{(1)}(\mathbf{Q},\tau)$, frequently called the "measured intermediate scattering function" $f^M(\mathbf{Q},\tau)$, can be written as

$$g^{(1)}(\mathbf{Q},\tau)=\frac{\sum_j\sum_k\left\langle b_j(\mathbf{Q},0)b_j^*(\mathbf{Q},\tau)e^{-i\mathbf{Q}\cdot[\mathbf{R}_j(0)-\mathbf{R}_k(\tau)]}\right\rangle}{\sum_j\sum_k\left\langle b_j(\mathbf{Q})b_j^*(\mathbf{Q})e^{-i\mathbf{Q}\cdot[\mathbf{R}_j(0)-\mathbf{R}_k(0)]}\right\rangle}\equiv f^M(\mathbf{Q},\tau). \tag{3.37}$$

For identical interacting spheres, where all $\{b_j^*(\mathbf{Q},t)\}=b(\mathbf{Q})$, Eq. (3.37) simplifies to

$$f^M(\mathbf{Q},\tau)\equiv f(\mathbf{Q},\tau)\equiv\frac{F_c(\mathbf{Q},\tau)}{S(\mathbf{Q})}, \tag{3.38}$$

where

$$F_c(\mathbf{Q},\tau)=N^{-1}\sum_j\sum_k\left\langle e^{-i\mathbf{Q}\cdot[\mathbf{R}_j(0)-\mathbf{R}_k(\tau)]}\right\rangle. \tag{3.39}$$

Here $S(\mathbf{Q})$ is the static structure factor discussed in section 3.1. $F_c(\mathbf{Q},\tau)$ is called the intermediate scattering function or the collective dynamic structure factor and $f(\mathbf{Q},\tau)$ is the normalized intermediate scattering function.

In a DLS experiment, the intermediate scattering function $f^M(\mathbf{Q},\tau)$ (or $g^{(1)}(\mathbf{Q},\tau)$) is usually the quantity of interest and can be obtained directly from the intensity correlation function $g^{(2)}(\mathbf{Q},\tau)$ by inverting Eq. (3.36):

$$f^M(\mathbf{Q},\tau) = \sqrt{g^{(2)}(\mathbf{Q},\tau) - 1}. \tag{3.40}$$

The results obtained until now correspond to the situation of "far field", since they have been derived considering the amplitude of the electric field scattered to a point in the far field (Eq. (3.6)). Actually, a detector has a non-zero active area and therefore it sees different scattered fields (or intensities) at different points on its surface. Then it can be shown that in real experiments Eq. (3.36) is modified to

$$g^{(2)}(\mathbf{Q},t) = 1 + \beta[g^{(1)}\mathbf{Q},t)]^2, \tag{3.41}$$

where β is a factor which represents the degree of spatial coherence of the scattered light over the detector and is determined by the ratio of the detector area to the area of one speckle. When this ratio is much less than 1, as is the case of a "point detector", $\beta \to 1$. On the contrary when the detector is actually detecting many independently fluctuating speckles $\beta \to 0$. In practice the detector aperture is usually chosen to accept about one speckle in such a way that $\beta \approx 0.8$. Inverting Eq. (3.41) gives

$$\beta^{1/2} f^M(\mathbf{Q},\tau) = \sqrt{g^{(2)}(\mathbf{Q},\tau) - 1}. \tag{3.42}$$

The setup dependent coherence factor β can be obtained by fitting the time correlation functions and is useful for the alignment of the experimental apparatus. Once the setup is aligned β remains unchanged and is regarded as an uninteresting parameter.

Polarized and Depolarized Dynamic Light Scattering Measurements

By dealing with optically isotropic samples, the averaged quantities such as $g^{(1)}(Q,\tau)$ and $g^{(2)}(Q,\tau)$ only depend on the modulus of the scattering vector ($|\mathbf{Q}|$). On the other hand, particles with anisotropic shape posses an anisotropic polarizability tensor. For particles with axial symmetry such as discs and rods, the eigenvectors of polarizability tensor correspond to the directions perpendicular and parallel to the symmetry axis and their resultant eigenvalues are $\gamma_{\|}$ and $\gamma_{\perp}$ respectively. In this case, for a vertically polarized incident field, the vertical and horizontal scattering components give informations about the translational and rotational degrees of freedom.

Figure 3.4 shows the two different pairs of polarization directions used in this work. The vertically polarized incident beam is scattered in both vertical (a) and horizontal (b) modes, registered by a photomultiplier tube as I_{VV} and I_{VH}. The experiments performed with these signals are generally called Polarized and Depolarized Dynamic Light Scattering (DLS and DDLS).

The total electric field scattered by particles with axially symmetric optical anisotropy (when the incident electric field is linearly polarized in the vertical direction) has two components. The first is the vertically polarized component E_{VV}, which has an amplitude proportional to the average polarizability ($\alpha = (\gamma_{\|} + 2\gamma_{\perp})/3$) and the second is the horizontal depolarized component E_{VH} which is proportional to the intrinsic particle anisotropy ($\beta = \gamma_{\|} - \gamma_{\perp}$), that is the difference between the polarizabilities parallel and perpendicular to the optical axis [69]. For particles with spherical symmetry the parallel and perpendicular polarizabilities are equal, so that

Figure 3.4. Two different pairs of polarization directions used in this work: (a) polarized scattering signal I_{VV} and (b) depolarized scattering signal I_{VH}.

the intrinsically particle anisotropy is zero ($\beta = 0$). It implies that the depolarized signal (I_{VH}) is also zero. Thus, for a dilute suspension of identical non-interacting spheres, the field correlation function has only the contribution of the polarized component of the electric field (E_{VV}) that is given by Eq. (3.34). If we define the displacement of the particle in time by

$$\Delta\mathbf{R}(\tau) = \mathbf{R}(\tau) - \mathbf{R}(0), \tag{3.43}$$

we see that Eq. (3.34) can be written as:

$$g^{(1)}_{VV}(\mathbf{Q},t) = \left\langle e^{i\mathbf{Q}\cdot\Delta\mathbf{R}(\tau)} \right\rangle, \tag{3.44}$$

which means that DLS provides information on the average translational motion of a single particle.

The displacement of a particle in Brownian motion is a (real) three-dimensional random variable having a Gaussian probability distribution

$$P\left[\Delta\mathbf{R}(\tau)\right] = \left[\frac{3}{2\pi\langle\Delta R^2(\tau)\rangle}\right]^{3/2} \exp\left[-\frac{3\Delta R^2(\tau)}{2\langle\Delta R^2(\tau)\rangle}\right], \tag{3.45}$$

where the particle's mean square displacement in time is:

$$\langle\Delta\mathbf{R}(\tau)\rangle = 6D_t\tau. \tag{3.46}$$

The free-particle translational diffusion coefficient if given by the well known Stokes-Einstein relation

$$D_t = \frac{k_B T}{6\pi\eta R}, \tag{3.47}$$

where k_B is the Boltzmann's constant, T is the temperature, η the shear viscosity of the suspension medium, and R the particles radius. Evaluation of the average in Eq. (3.44) over the Gaussian probability distribution (Eq. (3.45)) gives

$$g^{(1)}_{VV}(\mathbf{Q},\tau) = \exp\left[-\frac{Q^2}{6}\left\langle\Delta R^2(\tau)\right\rangle\right] = e^{-Q^2 D_t \tau}. \tag{3.48}$$

In this simple case the autocorrelation function behaves as a single exponential decay. The normalized intensity correlation function on the other hand can be calculated by using the Siegert expression (Eq. (3.41)), and it takes the form

$$g^{(2)}_{VV}(\mathbf{Q},\tau) = 1 + \beta e^{-2D_t Q^2 \tau}. \tag{3.49}$$

However, if one considers particles with axially symmetric optical anisotropy, the scattered light will be composed by the two components E_{VV} and E_{VH}, which originate both polarized and depolarized correlation functions. Assuming that orientations of different particles are uncorrelated and decoupled from the translation motion, the measured polarized and depolarized intensity correlations at scattering vector $\mathbf{Q}$ (with modulus given by Eq. (3.5)) are

$$g^{(2)}_{VV}(\mathbf{Q},\tau) = 1 + \left[\frac{\alpha^2 F_c(\mathbf{Q},\tau) + \frac{4}{45}\beta^2 F_r(\tau) F_s(\mathbf{Q},\tau)}{\alpha^2 + \frac{4}{45}\beta^2}\right]^2 \tag{3.50}$$

$$g^{(2)}_{VH}(\mathbf{Q},\tau) = 1 + \left[F_s(\mathbf{Q},\tau) F_r(\tau)\right]^2, \tag{3.51}$$

where $F_c(\mathbf{Q},\tau)$ is the dynamic structure factor expressed by Eq. (3.39) which is associated to the collective diffusion of the particles, $F_s(\mathbf{Q},\tau) = \langle \exp[-i\mathbf{Q}\cdot(\mathbf{R}(0) - \mathbf{R}(\tau))]\rangle$ is the translational self correlation function, previously shown in Eq. (3.44), and $F_r(\tau) = 4\pi\langle Y^*_{2,1}(\hat{u}(0)) Y_{2,1}(\hat{u}(\tau))\rangle$ is the rotational self-correlation function in which $Y_{2,1}$ is the second-order spherical harmonic of index 1 and $\hat{u}(\tau)$ is the unit vector determining the orientation of a particle at time τ.

In the case of spherical non-interacting particles, $F_c(\mathbf{Q},\tau)$, $F_s(\mathbf{Q},\tau)$ and $F_r(\tau)$ can be represented by single exponential decays

$$F_c(\mathbf{Q},\tau) = F_s(\mathbf{Q},\tau) = e^{-Q^2 D_t \tau} \tag{3.52}$$

$$F_r(\tau) = e^{-6D_r\tau}, \tag{3.53}$$

where D_t and D_r are respectively the translational and rotational diffusion coefficient of a single particle at infinite dilution. In the presence of interactions, $F_c(\mathbf{Q},\tau)$ and $F_s(\mathbf{Q},\tau)$ start to have contributions from many exponentials terms. It is therefore possible to extract from $F_s(\mathbf{Q},\tau)$ a short-time and a long-time self-diffusion coefficient, D^s_t and D^l_t, respectively. In the short-term limit the particle diffuses in an approximately constant configuration of the other particles and its motion is only influenced by hydrodynamic interactions. In the long-time limit the particle interacts with many other particles, and its motion is slowed down by direct interparticle forces. The case of $F_r(\tau) = \exp(-6D_r\tau)$ is similar: one can extract both short-time and long-time rotational diffusion coefficients, respectively D^s_r and D^l_r [72, 73, 74]. Generally speaking, the translational and rotational degrees of freedom will be strongly depend on interparticle interaction potential and on particle concentration.

Considering the case of non-interacting particles with axially symmetric optical anisotropy, we have that the polarized and depolarized field correlation function can be expressed by

$$g^{(1)}_{VV}(\mathbf{Q},t) = \exp(-\tau_{VV} t) \tag{3.54}$$

$$g^{(1)}_{VH}(\mathbf{Q},t) = \exp(-\tau_{VH} t), \tag{3.55}$$

where the first cumulant are given by [69, 72, 73, 74]

$$\tau_{VV} = \left(D_t Q^2\right)^{-1} \tag{3.56}$$

$$\tau_{VH} = \left(6D_r + D_t Q^2\right)^{-1}. \tag{3.57}$$

Since the values of τ_{VV} and τ_{VH} can be directly obtained by fitting, respectively, DLS and DDLS correlation curves, it comes out that the values of the translational and rotational diffusion coefficients can be calculated. While D_t can be obtained directly by DLS, the rotational diffusion coefficient (D_r) requires the extraction of the contribution from the translational degree of freedom (D_t). Therefore, to compute D_r we need both DLS and DDLS at a fixed scattering angle, or only DDLS at many Q-values in order to plot τ_{VH} as a function of Q^2 and make a linear fit. In this way the limit of $Q \to 0$ gives the value of the pure rotational diffusion coefficient.

3.1.4 Multi Angles Dynamic Light Scattering Setup

This section is dedicated to the description of the five angles dynamic scattering setup built and used to acquire DLS and DDLS measurements during this work. Figure 3.5 shows the sketch of this experimental apparatus.

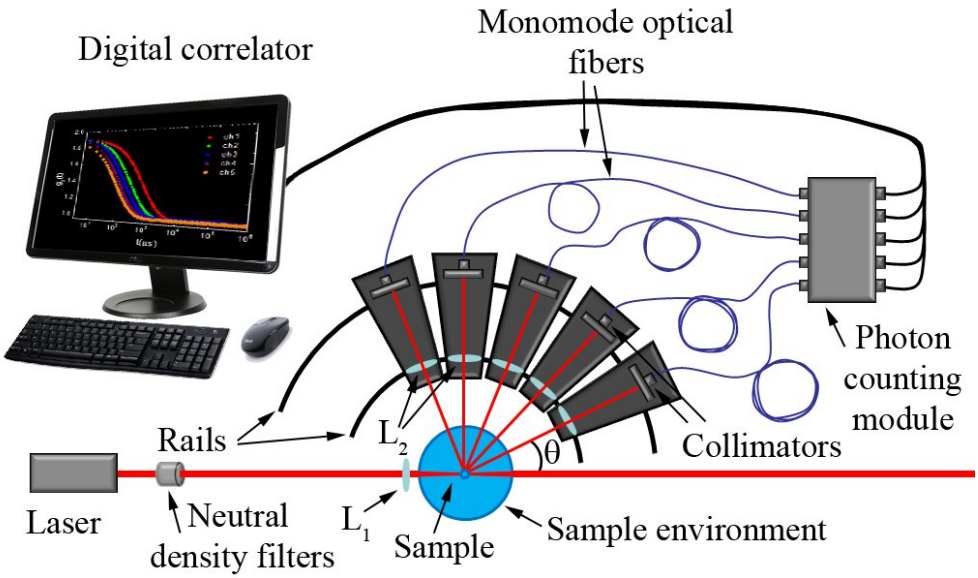

Figure 3.5. Sketch of the five angles dynamic light scattering setup. The laser beam of wavelength 642 nm is focused by lens L_1 on the center of the sample. The scattered field is collected through lenses L_2 at five different scattering angles θ and then collimated on five monomode optical fibers. The collection/collimation devices can move on circular rails, in such a way that the scattering angles can be chosen before the experiment. Five photomultiplier tubes collect photon-counts that are analyzed by the software correlator to compute time autocorrelation functions.

A solid state laser with a wavelength of $\lambda = 642$ nm and a power of 100 mW has been used. The laser beam is vertically polarized (perpendicular to the plane of the

paper) with a polarization ratio of 500:1. In order to control the intensity of the laser impinging the sample, and consequently the intensity of the scattered light, neutral density filters are placed in front of the laser. These filters have been used in order to choose an incident intensity that provides the best correlation quality, *i.e.* high coherence factor and low noise. The laser beam is then focused on the sample by a lens (L_1) with a beam waist of approximately 50 μm, which corresponds to a focal length of 125 mm. The sample environment is a cylindrical transparent glass cell, called VAT, with 111 mm of diameter, filled with distilled water that is used as index matching fluid in order to reduce the refraction of the scattered light through the walls and stray light scattering. The sample cuvette with cylindrical shape is inserted in the center of the VAT. The focal point is at the center of the circular optical geometry that can be evidenced by the concentric rails used to move the detection lenses L_2 and the collimators coupled together by a metallic base.

The scattered intensity is collected at five different values of the scattering angle θ, which corresponds to five different values of the exchanged momentum, according to the relation $Q = (4\pi n/\lambda)\sin(\theta/2)$. The values θ_i ($i = 1,\ldots,5$) of the scattering angles can be chosen by displacing the bases that are free to move on circular rails centered on the scattering cell. Each base holds the optics and mechanics necessary for the collection of the scattered beam as well as for its collimation on an optical fiber. The minimum angular offset between adjacent collection device is 20°. The scattered light is collected by biconvex lenses (L_2) with focus on the illuminated sample volume, so that the scattering volume V is defined by the intersection of Gaussian beam profiles relative to lenses L_1 and L_2. The scattered light is collimated in the core of each monomode optical fiber that brings the signal to the photomultipliers used in single photon counting mode. The number of photons detected by each photomultiplier is transfered to a computer through an input-output digital card from National Instruments®, and the time autocorrelation functions are computed using a software correlator developed by Di Leonardo [75].

A top view photograph of the five angles DLS setup is shown in Fig. 3.6. The laser beam as well as the scattered light at five different θ are highlighted by red lines. All the optical components shown in the schematic Figure 3.5 can be evidenced in this photograph.

For DDLS measurements optical polarizers have been placed in the base, between L_2 and the collimators, in order to select only a required scattered polarization direction. In the case of DLS no optical polarizer were used, since the depolarized intensity (I_{VH}) is much lower than I_{VV} giving no significant contribution to the polarized correlation function, issue better discussed later.

Setup Calibration

In order to calibrate the five channels DLS setup we have performed time correlation experiments using the polarized component of the scattering intensity ($g^{(2)}_{VV}(\mathbf{Q},t)$) for a standard sample of a highly diluted suspension of latex microspheres with a well defined diameter $\varnothing = 90$ nm. These colloidal particles are performing Brownian motion as consequence of collisions with the molecules of the surrounding medium [69]. As already discussed in section 3.1.3, the normalized field correlation function is given, in Gaussian approximation, by the expression (3.54) that by using the

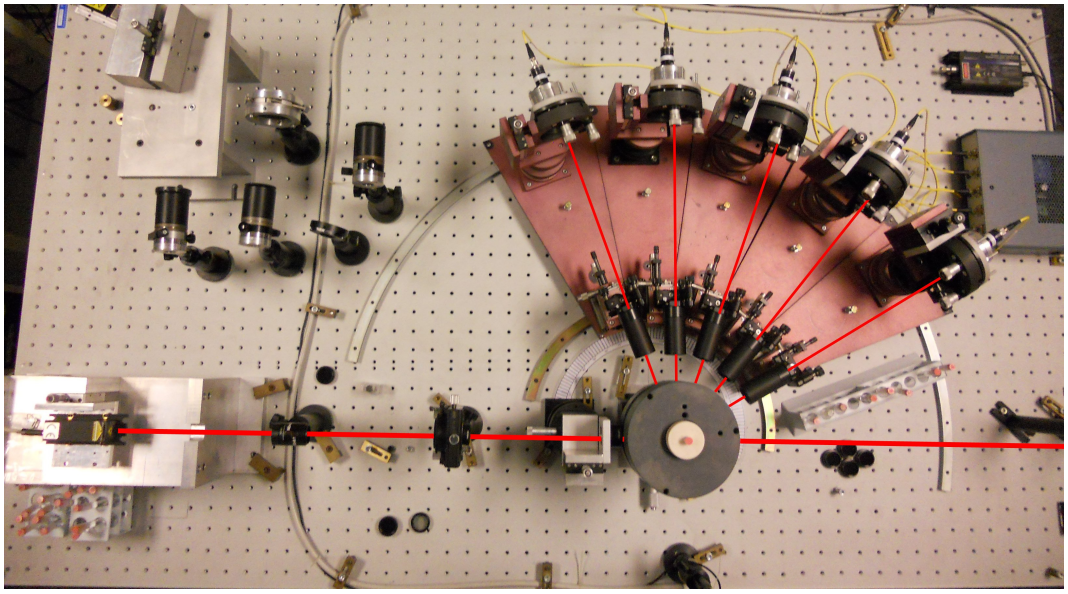

Figure 3.6. Top view photograph of the five angles DLS setup. The laser beam and the scattered light are evidenced by red lines drawn only to guide the eyes. All the optical components shown in the schematic Figure 3.5 can be observed in this photograph.

Siegert expression (Eq. (3.41)) gives:

$$g^{(2)}_{VV}(\mathbf{Q},t) - 1 = \beta e^{-2\tau_{VV}t}, \tag{3.58}$$

where β and τ_{VV} are fitting parameters. An important detail in a dynamic light scattering experiment is to ensure good optical coherence, *i.e.* that the detector is monitoring only the coherence area of the scattered radiation. This quantity is related to the coherence factor (β parameter) that should be close to the maximal and optimal value $\beta = 1$. For each scattering angle the value of β is maximized by fine alignment of the collection and collimation optics. We have achieve coherence factor values $\beta > 0.9$ for all the five scattering angles, which characterize a very good optical alignment. The value of the relaxation time τ_{VV} is associated with the exchanged momentum and the translational coefficient diffusion of the particles by Eq. (3.56).

We use the expression obtained by combining Eqs. (3.56), (3.47) and (3.5) to align the system:

$$\theta = 2\arcsin\left[\frac{\lambda}{2n}\sqrt{\frac{3}{2\pi}\frac{\eta R}{\tau_{VV}k_BT}}\right]. \tag{3.59}$$

where R is the nominal radius of the calibration particles. The angular alignment is a critical point. In fact Fig. 3.7 illustrates the situation where we consider at first instance, for simplicity, only the interface between the VAT and the air. We represent as a horizontal red line the laser beam crossing the sample and the vertical red light the scattered light coming from the sample. The collection lens L_2 can move along the X axes, by means of a translation stage. When the lens L_2 is correctly aligned, it is placed at the central position ($x = 0$), its optical axes lies along the

vertical dotted line and the collected scattered light impinges normally on the walls. In this condition the scattering angle is $\theta_0 = 90°$. On the other hand, if the lens is placed in a different position (as shown in Fig. 3.7), the scattering light follows the red path, which is affected by refraction at the walls. In this case the scattering angle is θ_{eff} instead of θ_0.

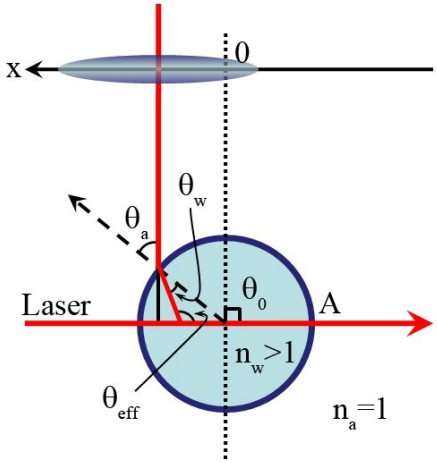

Figure 3.7. Schematic geometry of the refraction suffered by the scattered light coming from the sample. We depict the view along the scattering plane where the laser beam, represented by horizontal red line, passes through the sample. The lens L_2 is supposed to be able to move along the x-axis. For simplicity we consider, at first instance, only the refraction through the water inside the VAT and the air *i.e.* neglecting the effect of the VAT walls and the sample cuvette on its center. If the lens is placed in a position different from $x = 0$, the scattered light follows the read path and suffers refraction forming an angle θ_{eff} different from θ_0. Here, A is the radius of the VAT, $n_w(n_a)$ are the refractive indices of water(air) and $\theta_w(\theta_a)$ are the angle of incidence(refraction).

Therefore, in order to correctly align the lens L_2, it is necessary to have θ_{eff} as a function of x. Hence, once the position x of the lens L_2 is fixed, we can acquire an intensity correlation function with the latex sample reference and fit the curve by using Eq. (3.58) to obtain the value of the relaxation time τ_{VV}. In this way, by measuring τ_{VV} as a function of x and by knowing the radius of the spheres, the temperature, the viscosity and the refractive index of the solvent we can obtain $\theta_{eff}(x)$ from Eq. (3.59). An example is given in Fig. 3.8 (open circles).

Based on the schematic scattering geometry shown in Fig. 3.7 and assuming only refraction effects, we can write a model to describe the expected behavior of θ_{eff}:

$$\theta_{eff}(x) = \theta_0 + \arcsin\left(\frac{x}{A}\right) - \arcsin\left(\frac{n_a x}{n_w A}\right), \tag{3.60}$$

where θ_0 is the nominal scattering angle, n_a and n_w are the refractive index respectively in air and water and A is the radius of the VAT (see Fig. 3.7). A generalization of Eq. (3.60) can be done, by taking into account the refraction at all the interfaces present in the sample environment, *i.e.* water-glass (cuvette), glass (cuvette)-water, water-glass (VAT) and glass (VAT)-air

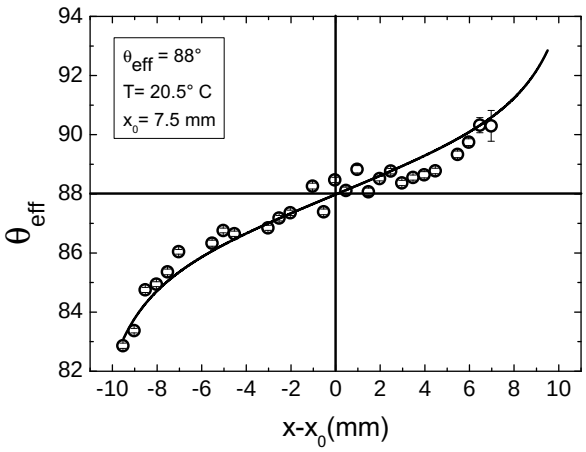

Figure 3.8. Values of the effective scattering angle θ_{eff} (open circles) computed according to Eq. (3.59) as a function of lens displacement $(x - x_0)$, as defined in Fig. 3.7. Full line represents the expected trend characterized by Eq. (3.61). The value of x_0 is then used to align the L_2 lens.

$$\begin{aligned}\theta_{eff}(x) &= \theta_0 + \arcsin\left(\frac{x-x_0}{A+dA}\right) - \arcsin\left(\frac{n_a(x-x_0)}{n_{gv}(A+dA)}\right) + \arcsin\left(\frac{x-x_0}{A}\right) \\ &- \arcsin\left(\frac{n_{gv}(x-x_0)}{n_w A}\right) + \arcsin\left(\frac{x-x_0}{a+da}\right) - \arcsin\left(\frac{n_w(x-x_0)}{n_{gc}(a+da)}\right) \\ &+ \arcsin\left(\frac{x-x_0}{a}\right) - \arcsin\left(\frac{n_{gs}(x-x_0)}{n_w a}\right), \end{aligned} \tag{3.61}$$

where n_w, n_{gs}, n_{gv} and n_a are the refractive indices of the water, glass of the cuvette, glass of the VAT and air respectively, a and A are the radius of the cuvette and VAT respectively, da and dA are the wall thickness of the cuvette and VAT respectively and finally x_0 accounts for the fact that the x axes origin corresponds to an arbitrary position of the translation stage. A direct comparison of the model (Eq. (3.61)) with the experimental results is shown by full line in Fig. 3.8. A fit procedure permits the estimation of the two parameters $\theta_0 \pm \delta\theta_0$ and $x_0 \pm \delta x_0$ that can be subsequently used to correctly align the lens L_2 just by moving it to the position x_0, which corresponds to the normal incidence configuration, with an effective scattering angle θ_0. The same procedure is repeated for each channel, where we found the values of the scattering angles to be $\sim 27.6°$, $48.8°$, $68.8°$, $88°$ and $107.8°$.

Taking the advantage of the five different Q-values, we have also tested the Brownian behavior of the latex sample. For this purpose we acquired several intensity correlation functions and fitted them using the expression (3.58). The value of $1/\tau_{VV}$ as a function of Q^2 is shown in Fig. 3.9 (a). The figure clearly shows that $1/\tau_{VV}$ scales linearly with Q^2 in agreement with the expected Brownian motion behavior. In fact, we fitted all the curves of τ_{VV} versus Q by using a power law expression ($\tau_{VV} = a' Q^{n_{\tau_{VV}}}$), and the obtained mean value of the exponent $n_{\tau_{VV}}$

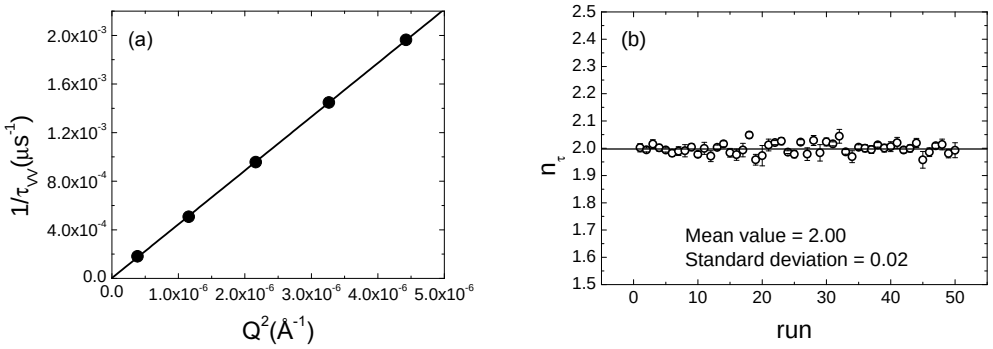

Figure 3.9. (a) Inverse of the relaxation time versus the square wave vectors Q^2. The scattering angles were fixed at $\sim 27.6°$, $48.8°$, $68.8°$, $88°$ and $107.8°$. The black full line in (a) represents a linear fit. (b) Values of the exponent $n_{\tau_{VV}}$ as obtained by fitting the measured intensity correlation functions with the power law expression $\tau_{VV} = a'Q^{n_{\tau_{VV}}}$.

is $n_{\tau_{VV}} = 2.00 \pm 0.02$ (as shown in Fig. 3.9 (b)), *i.e.* $\tau_{VV} \propto 1/Q^2$, reflecting the diffusive nature of the motion.

3.2 X-ray Photon Correlation Spectroscopy

The X-ray Photon Correlation Spectroscopy (XPCS) experiment was performed at the Troika beamline ID10 of the European Synchrotron Radiation Facility (ESRF, Grenoble, France) after the acceptance of a proposal. In this XPCS experiment a collimated and focused X-ray beam with energy of 8 keV, which corresponds to a wavelength $\lambda = 0.155$ nm, was used as a probe. Because of the very short wavelength, XPCS technique is able to explore very high Q-values that are inaccessible for DLS methods involving visible light. The X-ray beam, generated in a powerful triple undulator source, is delivered on the sample via a single bounce Si(111) monochromator reflection. Si mirrors were employed in the beam path under grazing incidence conditions to suppress hard X-rays originating from higher-order monochromator reflections. Coherent illumination of the sample was ensured by a pinhole aperture (10×10 μm^2) which selects a fraction of the beam to limit the scattering volume to the coherence volume of the beam, resulting in more than 10^{10} photons/second impinging on the sample. The stray scattering and fringes produced by the aperture were removed by carefully adjusting a set of guard slits [76]. A photograph of the XPCS setup used in this work is shown in Fig. 3.10. The X-ray beam path, sample position and Medipix detector are pointed out.

While conventional DLS experiments use a point detector, such as a monomode optical fiber coupled to a photomultiplier, acquiring correlation functions at a single Q-value, XPCS uses multi-element detectors, such as Charge-Coupled Device (CCD) cameras that allows the acquisition of the scattered intensity at several Q-values. In this XPCS experiment a Medipix, that is a family of photon counting pixel detectors, was placed at a distance $L = 3$ m downstream of the sample to record the scattering speckle patterns at rate up to 1 Hz. A fast shutter upstream of the

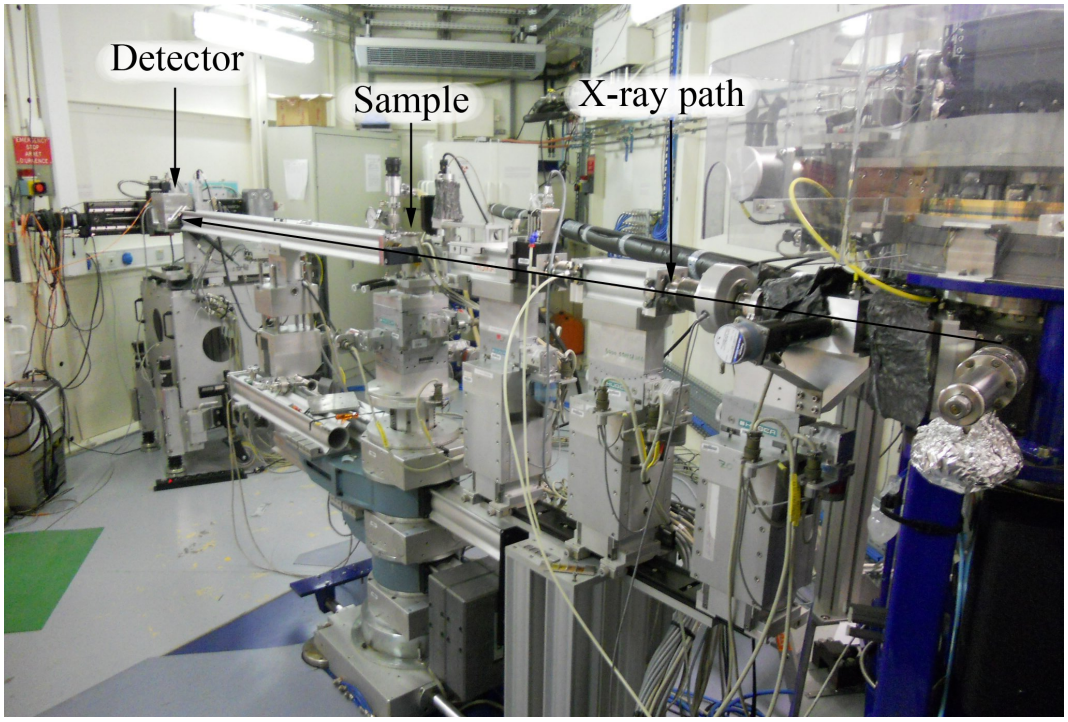

Figure 3.10. Photograph of the XPCS setup available at the Troika beamline ID10 of the European Synchrotron Radiation Facility (ESRF, Grenoble, France). The X-ray beam path, sample position and Medipix detector are evidenced by arrows.

sample is synchronized with the Medipix detector in order to protect the sample from unnecessary X-ray exposition during the read-out of the detector or during waiting time between acquisitions. Figure 3.11 (a) shows a single scattering speckle pattern generated during measurements on Laponite samples. To avoid possible detector damage, a beam stop with dimension of 1 mm is placed just after the beam impinges the sample. The spot covered by the beam stop can be evidenced in the left-down corner of Fig. 3.11 (a). The distance L was chosen to have the best compromise between accessible Q-range and the Q-resolution of a pixel which affects the contrast of the correlation functions.

The point detector generally used in DLS techniques requires considerable time-averaging of the intensity autocorrelation function to ensure reasonable statistics. In addition to the possibility of measuring correlation functions at many Q-values, multi-element detectors permits the reduction of the total experimental time, since each scattering speckle pattern is a composition of several point detectors that can be also averaged. In fact, the key advantage of using multi-element detectors is that the ensemble average may be obtained by simply averaging over pixels corresponding to the same propagation vector $|\mathbf{Q}|$, as depicted by concentric annulus in Fig. 3.11 (a).

For each measurement thousands of speckle patterns are recorded in order to be subsequently analyzed. In a multi-speckle scheme the ensemble-averaged time-resolved correlation functions, also known as two-times correlation functions, are calculated from the scattered intensity I_s per pixel in speckles images (Fig. 3.11 (a))

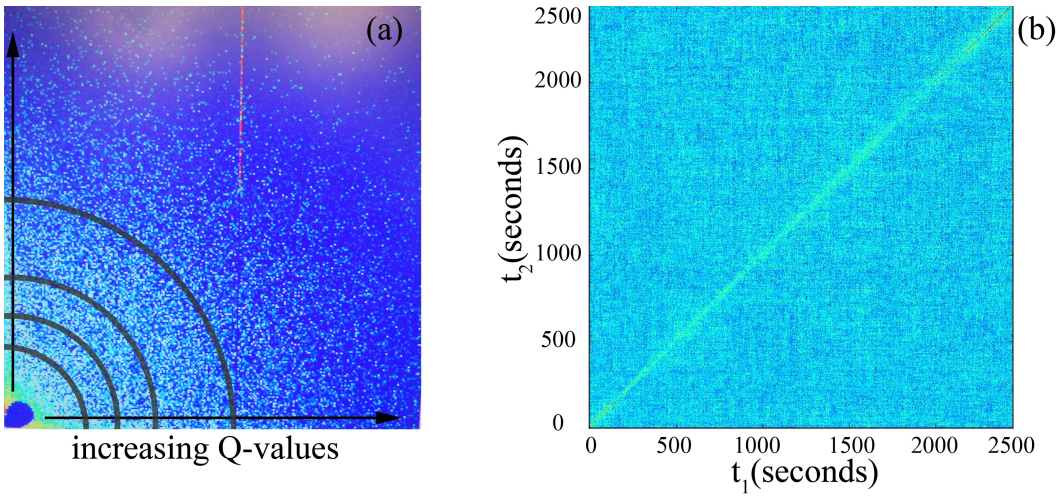

Figure 3.11. (a) Single scattering speckle pattern generated during measurements on Laponite samples. The spot in the left-down corner represents the point in which the direct forward beam would reach the detector. The arrows point towards the increasing scattering angle directions. Concentric annulus depict the regions in which the propagation vector ($|\mathbf{Q}|$) is the same. (b) Ensemble-averaged two-time correlation function calculated through Eq. (3.62) at $Q = 7.2 \times 10^{-3}$ Å^{-1} during a measurement of 2500 seconds in a Laponite sample.

taken at different times t_1 and t_2 according to the expression

$$G(\mathbf{Q}, t_1, t_2) = \frac{\langle I_s(\mathbf{Q}, t_1) I_s(\mathbf{Q}, t_2) \rangle_\phi}{\langle I_s(\mathbf{Q}, t_1) \rangle_\phi \langle I_s(\mathbf{Q}, t_2) \rangle_\phi}, \tag{3.62}$$

where the subscript ϕ indicates that the averaging is performed on the ensemble of pixels corresponding to a range of propagation vectors $|\mathbf{Q}| = Q \pm \Delta Q$, over which the correlations are expected to show negligible variation [77]. In practice a correlation function is averaged over all pixels positioned in an annulus centered at the direct beam position with radius $\sim \lambda L Q/(2\pi)$ and thickness $\sim \lambda L \Delta Q/\pi$ (see Fig. 3.11 (a)). Typically, this amounts to thousands of pixels.

In the cases where time averaging is valid, *i.e.* when the dynamics properties are not changing, $g^{(2)}(\mathbf{Q}, t)$ can be obtained by averaging values of $G(\mathbf{Q}, t_1, t_2)$ at fixed delay time, $t = t_2 - t_1$,

$$g^{(2)}(\mathbf{Q}, t) = \Big\langle G(\mathbf{Q}, t_1, t) \Big\rangle_{t_1}. \tag{3.63}$$

However, even for out-of-equilibrium systems, such as Laponite, when dynamics are evolving on time, it is possible to select a time interval in which the dynamics is practically stationary and then perform the time average according to Eq. (3.63). When the system presents stationary dynamics, the contour lines in plots of $G(\mathbf{Q}, t_1, t_2)$ are parallel to the diagonal, what is not the case in Fig. 3.11 (b), which demonstrate a clear evidence of aging [77, 78]. Nevertheless, divisions of Fig. 3.11 (b) in small squares of 500 seconds can be done, and during these time intervals the system can be considered stationary.

3.3 Neutron Spin Echo

The Neutron Spin Echo (NSE) experiment was available at the spectrometer IN15 of the Institute Laue-Langevin (ILL, Grenoble, France) after the acceptance of a proposal. NSE spectroscopy is a quasielastic neutron scattering technique that determines the time-space correlation function on time-scales from subnanosecond to submicrosencond and length-scales from several angstroms to several hundred angstroms [79]. Therefore, this makes the NSE a suitable technique to cover a time and scattering vector range that is not accessible by DLS.

The basic idea behind NSE spectrometers is that they encode the neutron energy into the Larmor precession angle of the neutrons magnetic moment. Polarized neutrons pass through two identical magnetic fields (large solenoids), one placed before and one placed after the sample. A phase inversion happens at the sample either by a π flipper or by the sample itself. If the scattering process is strictly elastic, the precession angles in the two fields are equal and opposite, so that full polarization is recovered, independently of the initial neutron velocity distribution. This method allows one to obtain high energy resolution over a wide range of incident wavelengths. A schematic illustration of a NSE spectrometer is shown in Fig. 3.12.

In the following we briefly describe each step (numbered in Fig. 3.12) experienced by the neutrons during the experiment:

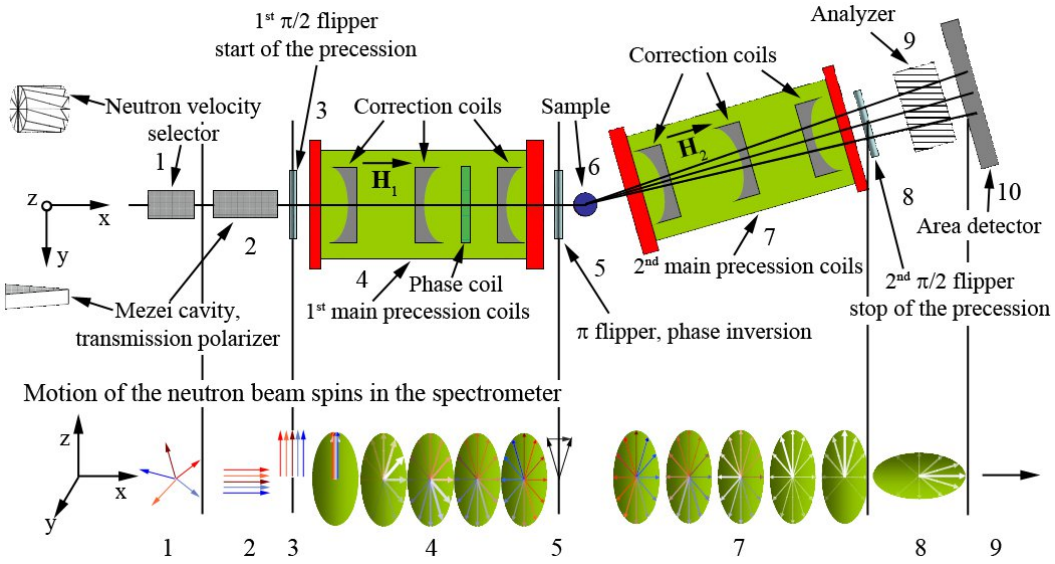

Figure 3.12. Schematic illustration of a neutron spin echo spectrometer. The sketch in the bottom of the figure demonstrates the motion of the neutron beam spins in the spectrometer. The numbers distinguishing each step experienced by the neutrons during the experiment.

1. A velocity selector determines the mean velocity (wavelength) of the neutron beam, usually with a wavelength spread in the order of 10-20%;

2. The beam goes through a polarizing device such as a Mezei cavity. Here only half of the neutrons are transmitted with spins aligned to the velocity direction,

x;

3. The first $\pi/2$ flipper changes the spin direction from x to z direction, perpendicular to the magnetic field inside the main coils. The precession of the spins starts;

4. The neutron beam passes through the first precession coil. This coil produces a homogeneous field parallel to the direction of the neutron path. Each neutron spin will perform a Larmor precession around the magnetic field direction. Faster neutrons will spend less time than slow neutrons in the field and their final precession angle will be smaller. At the end of the first coil the neutron beam is completely depolarized. Each spin has performed as many as 10^5 turns;

5. The π flipper rotates the spin direction of 180° around the z axis. The y component of the spin change sign;

6. The neutron beam interacts with the sample. The neutrons will exchange momentum and energy with the sample, changing their direction and velocity. If the sample is not magnetic the spin status does not change. On the other hand, for magnetic samples the magnetic interaction flips the spins and the π flipper is not necessary;

7. The neutron beam passes through the second coil. Neutrons that have not changed their velocity interacting with the sample (elastic scattering) will regain their full polarization at the end of the second coil. Furthermore, neutrons scattered quasielastically (small energy change) will not fully regain the initial polarization. The final result will be a distribution of spin direction centered around the z-axis. The resulting polarization will be less than 1;

8. A second $\pi/2$ flipper projects the spin onto the xy plane for the analysis. The precession of the spins stops;

9. An analyzer composed by an array of supermirrors onto and absorber material, transmits the neutrons with probability proportional to the cosine of the angle between the spin direction and the z-axis;

10. An area detector collects the resulting signal.

While DLS and XPCS measure the normalized intensity time correlation function ($g^{(2)}(\mathbf{Q},\tau)$) expressed by Eq. (3.32), NSE directly determines the intermediate scattering function ($f^M(\mathbf{Q},\tau) \equiv g^{(1)}(\mathbf{Q},\tau)$). Both correlators are associated each other by the Siegert relation (Eq. (3.36)) presented previously.

Figure 3.13 shows a photograph of the NSE spectrometer experiment used in this work. Here, many of the components, such as the first and second main precession coils, described in the schematic illustration (Fig. 3.12) can be recognized. The neutron beam path and the sample position are specifically pointed out.

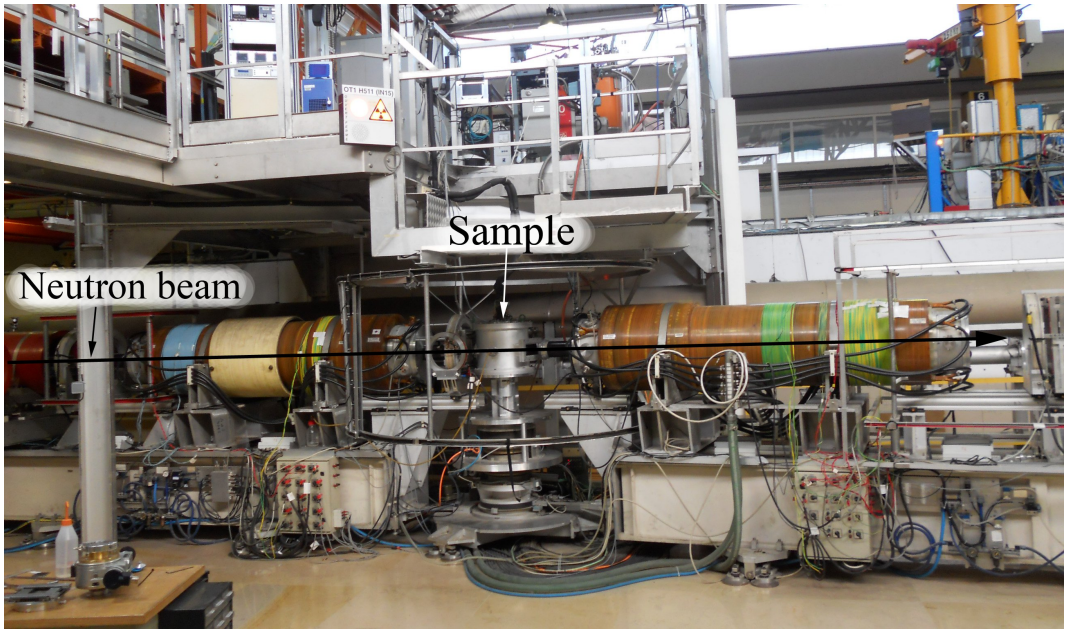

Figure 3.13. Photograph of the neutron spin echo spectrometer located at the spectrometer IN15 of the Institute Laue-Langevin (ILL, Grenoble, France). The neutron beam path and the sample position are evidenced by arrows.

3.4 Small Angle X-ray Scattering

The Small Angle X-ray Scattering (SAXS) experiments were performed at the high brilliance beam line ID2 of the European Synchrotron Radiation Facility (ESRF, Grenoble, France) after the acceptance of the proposal. This technique has a two-dimensional detector that explores Q-values corresponding to length scales from nanometer to micrometer and permits to probe structural information about inhomogeneities of soft matter and related system, which is suitable to study the arresting dynamics of Laponite systems.

A photograph of the SAXS instrument used in this work is shown in Fig. 3.14. The direction of the incoming X-ray beam is evidenced by an arrow, where in front of it the samples are placed.

Since interatomic distances are smaller compared to the length scales probed by small angle scattering technique, the medium is usually treated as a continuum with an average density. Consequently, the scattering process is described as arising from "scattering objects" of some electron density embedded in a medium of different density.

The intensity profiles from small angle scattering contain information on the size and shape of the particles as well as on the interactions between them. In order to describe how to extract these informations from the scattering intensity, we assume that the elementary scattering objects are particles that can be isolated in the sample or distributed with some type of spatial correlations.

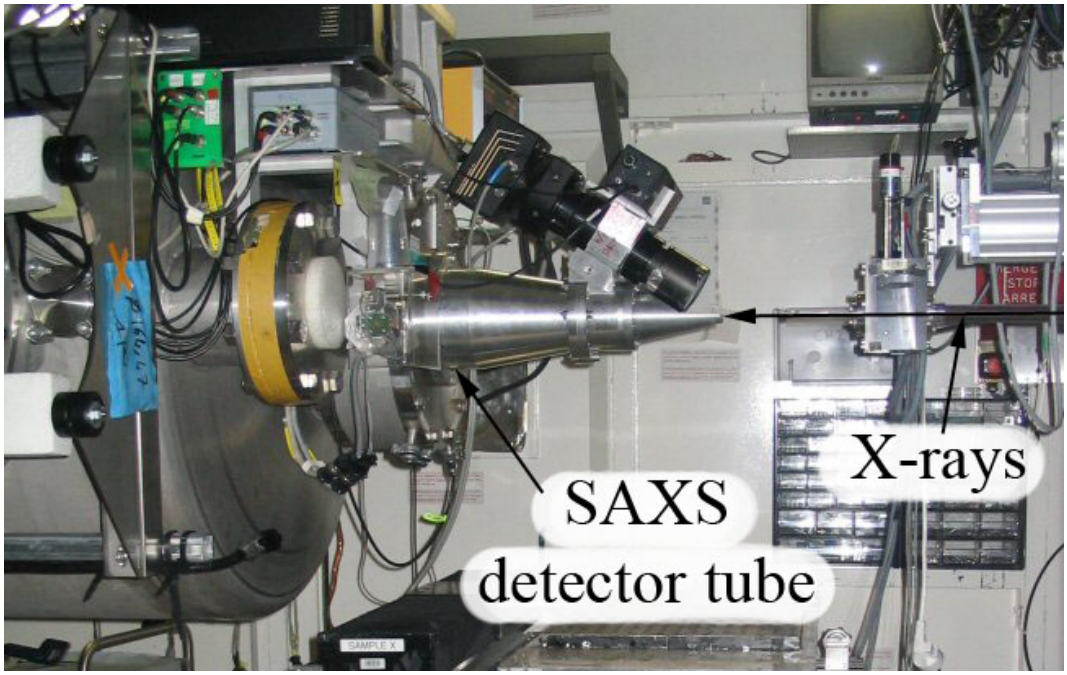

Figure 3.14. Photograph of the Small Angle X-ray Scattering (SAXS) instrument located at the high brilliance beam line ID2 of the European Synchrotron Radiation Facility (ESRF, Grenoble, France). The SAXS detector and the X-ray beam path are evidenced by arrows.

The Absolute Scattered Intensity

When a coherent beam of a flux N_0 passes through a sample with volume V and thickness e_s, part of the flux ΔN is elastically scattered in the direction $\mathbf{u}$ with a solid angle $\Delta\Omega$. This scattered portion of the beam can be expressed as

$$\Delta N = N_0 T \frac{e_s}{V} \frac{d\sigma}{d\Omega}(\mathbf{u})\,\Delta\Omega, \tag{3.64}$$

where T is the transmission of the sample, and $(d\sigma/d\Omega)(\mathbf{u})$ is the differential scattering cross section characteristic of the elastic interactions between the beam and material. The intensity I_s scattered by a unit volume can then be defined by

$$I_s\left(m^{-1}\right) = \frac{1}{V}\frac{d\sigma}{d\Omega}(\mathbf{u}) = \frac{\Delta N}{N_0}\frac{1}{T e_s \Delta\Omega}. \tag{3.65}$$

This quantity can be estimated experimentally by measuring the thickness (e_s), transmission T and the scattering properties $(\Delta N/N_0)(1/\Delta\Omega)$ of the sample.

General Expression for The Scattering Intensity

The scattering intensity $I_s(m^{-1})$ is directly related to the structure of the sample. The local interaction with the beam depends on the kind of beam and on the element i illuminated. For each couple of particles, it can be defined a scattering length b_i, therefore a density of scattering lengths can be written as

$$\rho(\mathbf{r}) = \sum \rho_i(\mathbf{r})\, b_i, \tag{3.66}$$

with ρ_i being the local density of scatterers of type i. In the case of X-rays, the photons can interact with every electron present in the sample. The scattering length of the associated electric field is the *Thompson scattering length* $b = e^2/(4\pi\varepsilon_0 m_e c^2)$, where e and m_e are the electric charge and the mass of the electron, c is the speed of light, and ε_0 is the permittivity of free space. This value corresponds to the classical electron radius that is equal to 2.817×10^{-15} m. Therefore, in X-ray scattering, a material can be simply described by its electron local density ρ_e. A common approximation is to consider the interaction with a scatterer at point r independent on the scattering by other scatterers (*Born approximation*). This approximation is generally valid for X-rays even for large density of scatterers. By assuming this approximation, the local scattered amplitudes simply add [80, 81]:

$$A(\mathbf{Q}) = \int_V \rho(\mathbf{r})\, e^{-i\mathbf{Q}\mathbf{r}} d\mathbf{r}. \tag{3.67}$$

The scattered intensity per unit volume V is then expressed as:

$$I_s(\mathbf{Q}) = \frac{A(\mathbf{Q})\, A^*(\mathbf{Q})}{V}. \tag{3.68}$$

By recalling Eq. (3.67) we have

$$I_s(\mathbf{Q}) = \frac{1}{V} \int_V \int_V \rho(\mathbf{r})\, \rho(\mathbf{r}')\, e^{-i\mathbf{Q}(\mathbf{r}-\mathbf{r}')} d\mathbf{r} d\mathbf{r}' \tag{3.69}$$

that can be rewritten as

$$I_s(\mathbf{Q}) = \int_V g(\mathbf{r}) e^{-i\mathbf{Q}\mathbf{r}} d\mathbf{r}, \tag{3.70}$$

where we have inserted the correlation function introduced by Debye and Bueche [82], $g(\mathbf{r})$, defined as follows

$$g(\mathbf{r}) = \frac{1}{V} \int_V \rho(\mathbf{r})\, \rho(\mathbf{r}+\mathbf{r}')\, d\mathbf{r}'. \tag{3.71}$$

Equation (3.70) shows that the scattered intensity is the Fourier transform of the spatial correlation function of the scattered length density. Following the same argument presented in section 3.1.2, the spatial correlation function demonstrates the following limits

$$\lim_{r\to 0} g(\mathbf{r}) = \langle \rho^2 \rangle \quad \text{and} \quad \lim_{r\to\infty} g(\mathbf{r}) = \langle \rho \rangle^2, \tag{3.72}$$

where the pointy brackets represent the spatial averaging. Now, in order to simplify the following expressions, we define the local fluctuation of the scattering length density as

$$\eta(\mathbf{r}) = \rho(\mathbf{r}) - \langle \rho \rangle, \tag{3.73}$$

where its mean-square becomes

$$\langle \eta^2 \rangle = \langle \rho^2 \rangle - \langle \rho \rangle^2. \tag{3.74}$$

Introducing the normalized correlation function $g_0(\mathbf{r})$

$$\langle \rho^2 \rangle g_0(\mathbf{r}) = \frac{1}{V} \int_V \eta(\mathbf{r}) \, \eta(\mathbf{r} + \mathbf{r}') \, d\mathbf{r}', \tag{3.75}$$

we obtain

$$g_0(\mathbf{r}) = \frac{g(\mathbf{r}) - \langle \rho \rangle^2}{\langle \eta^2 \rangle} \tag{3.76}$$

that now varies from 1, at $\mathbf{r} = 0$, to 0 at $\mathbf{r} = \infty$. Thus, it follows that the scattered intensity per unit of volume has the general form

$$I_s(\mathbf{Q}) = \langle \eta^2 \rangle \int_V g_0(\mathbf{r}) \, e^{-i\mathbf{Q}\mathbf{r}} d\mathbf{r} + \langle \rho \rangle^2 \delta(\mathbf{Q}), \tag{3.77}$$

where the second term on the right-hand side simply express that the mean density of scatterers produces signal only in the forward direction, *i.e.* when $\mathbf{Q} = 0$, and therefore only the fluctuations of density contribute to a measurable signal.

Systems of N Interacting Particles

When the suspension is diluted, the particles are widely separated and their positions can be considered as not correlated. In this situation, the intensity scattered by each particle can be added. Therefore, if one considers a unique particle with a generic shape of inhomogeneous density $\rho(\mathbf{r})$, the normalized amplitude scattered by this particle, for a given orientation, is given by

$$a(\mathbf{Q}) = \int_{V_{Part}} \rho(\mathbf{r}) \, e^{-i\mathbf{Q}\mathbf{r}} d\mathbf{r} = f(\mathbf{Q}), \tag{3.78}$$

yielding

$$I_{V_{Part}}(\mathbf{Q}) = a(\mathbf{Q}) \, a^*(\mathbf{Q}) = V^2 P(\mathbf{Q}), \tag{3.79}$$

with

$$P(\mathbf{Q}) = \frac{1}{V_{Part}} \int \int_{V_{Part}} \rho(\mathbf{u}) \, \rho(\nu) \, e^{-i\mathbf{Q}(\mathbf{u}-\nu)} d\mathbf{u} d\nu \tag{3.80}$$

being the *form factor* of the particle. It follows, therefore, the intensity per unit volume of a suspension containing N identical particles in a volume V is

$$I_s(\mathbf{Q}) = \frac{N}{V} V_{Part}^2 P(\mathbf{Q}). \tag{3.81}$$

A more general case is when the particles are identical but spatially correlated. For a given set of position and orientation of the particles, the total scattered intensity is

$$I_s(\mathbf{Q}) = \frac{A(\mathbf{Q}) \, A^*(\mathbf{Q})}{V}. \tag{3.82}$$

When the particles are diffusing in time (Brownian dynamics), the intensity is changing for each configuration and the time average is the measured quantity. For an ergodic system, it is equal to the statistical average done below

$$I_s(\mathbf{Q}) = \left\langle \frac{A(\mathbf{Q})\,A^*(\mathbf{Q})}{V} \right\rangle = \frac{1}{V}\left\langle \left(\int \rho(\mathbf{r})\, e^{-i\mathbf{Q}\mathbf{r}} d\mathbf{r} \right) \left(\int \rho(\mathbf{r}')\, e^{-i\mathbf{Q}\mathbf{r}'} d\mathbf{r}' \right) \right\rangle, \quad (3.83)$$

where $\langle \cdots \rangle$ is performed over the available positions and orientations of the particles. Introducing the centre position of a particle $\mathbf{r}_i$, one gets $\mathbf{r} = \mathbf{r}_i + \mathbf{u}$ and the intensity develops into

$$I_s(\mathbf{Q}) = \frac{1}{V}\left\langle \left(\sum_{i=1}^{N} e^{-i\mathbf{Q}\mathbf{r}_i} \int_{V_{Part}} \rho(\mathbf{u})\, e^{-i\mathbf{Q}\mathbf{u}} d\mathbf{u} \right) \left(\sum_{j=1}^{N} e^{-i\mathbf{Q}\mathbf{r}_j} \int_{V_{Part}} \rho(\nu)\, e^{-i\mathbf{Q}\nu} d\nu \right) \right\rangle \quad (3.84)$$

that can be rewritten by the average of the product

$$I_s(\mathbf{Q}) = \frac{N}{V}\left\langle \left(\int\int_{V_{Part}} \rho(\mathbf{u})\,\rho(\nu)\, e^{-i\mathbf{Q}(\mathbf{u}-\nu)} d\mathbf{u} d\nu \right) \left(\frac{1}{V} \sum_{i=1}^{N}\sum_{j=1}^{N} e^{i\mathbf{Q}(\mathbf{r}_j - \mathbf{r}_i)} \right) \right\rangle, \quad (3.85)$$

where the first term is the *form factor* $V_{Part}^2 P(\mathbf{Q})$ defined previously, and the second term is the structure factor $S(\mathbf{Q})$

$$S(\mathbf{Q}) = 1 + \frac{1}{N}\left\langle \sum_{i=1}^{N}\sum_{i\neq 1}^{N} e^{i\mathbf{Q}(\mathbf{r}_j - \mathbf{r}_i)} \right\rangle. \quad (3.86)$$

Finally, the following expression is obtained [80, 83]:

$$I_s(\mathbf{Q}) = \Phi V_{Part} P(\mathbf{Q})\, S(\mathbf{Q}), \quad (3.87)$$

where $\Phi = N/V$.

3.5 Sample Preparation

In this work we followed the protocol for sample preparation recently claimed by Ruzicka *et al.* in Ref. [14] in order to obtain reliable and reproducible results. Samples were prepared with Laponite RD manufactured by Rockwood Additives Ltd®. This Laponite has a bulk density of 2570 kg/m^3 and appears as a fine white powder where crystals structure are arranged into stacks held together electrostatically by sharing of sodium ions in the interlayer region between adjacent crystals (see Fig. 2.2).

Once dispersed into the solvent sodium ions are released from the crystal interlayers and a colloidal dispersion of nanometric discs is obtained, as amply discussed in chapter 2.

In this thesis we have investigated isotopic effects and therefore we have used both deuterium oxide (D_2O) with purity $\geq$ 99.9 % produced by EURISO-TOP®

and ultra pure deionised water with an electroresistance above 18 $m\Omega cm^{-1}$ obtained by a Milli-Q system present in our chemical laboratory.

A glove box under a Nitrogen (N_2) atmosphere was used during the preparation of all the samples to minimize CO_2 dissolution and possible sample degradation. In fact in atmospheric conditions, water absorbs from the air a quantity of carbon dioxide as big as its volume. Therefore, about 1% of the absorbed CO_2 is converted in carbonic acid through the process

$$CO_2 + H_2O \rightarrow H_2CO_3 \rightarrow H^+HCO^{3-}, \tag{3.88}$$

leading to a consistent acidification of the water. It has been shown [84, 85] that when Laponite particles are dispersed in an acid solution environment they originate a chemically unstable system. In fact at low pH values, Laponite dissolves according to the following equation [85]:

$$Si_8Mg_{5.45}Li_{0.4}H_4O_{24}Na_{0.7}+12H^+ +8H_2O \rightarrow 0.7Na^+ +8Si(OH)_4+5.45Mg^{2+}+0.4Li^+. \tag{3.89}$$

To prepare the samples firstly a certain quantity of the solvent is added into a beaker and its weight is measured with a digital balance that has an accuracy of $\pm$ 0.001 g. The mass of Laponite is then calculated by using the expression

$$M_{\text{Laponite}} = \frac{C_{\text{Laponite}}}{1 - C_{\text{Laponite}}} \times m_{H_2O}, \tag{3.90}$$

where C_{Laponite} is the desired Laponite concentration and m_{H_2O} is the previously measured mass of water. The equation (3.90) gives the mass of Laponite to be added in a certain amount of water (m_{H_2O}) in order to achieve the desired Laponite concentration solution in % of weight. For a given Laponite concentration, in order to mantain the same molar concentration in D_2O compared to H_2O, a fraction between the molar mass of H_2O and D_2O has been inserted in Eq. (3.90):

$$M_{\text{Laponite}} = \frac{C_{\text{Laponite}}}{1 - C_{\text{Laponite}}} \times m_{D_2O} \times \frac{PM_{H_2O}}{PM_{D_2O}}. \tag{3.91}$$

Subsequently, the calculated quantity M_{Laponite} is added to the D_2O and kept stirring vigorously for 30 minutes by using a magnetic stirrer. At the beginning of the agitation the solution has a milky color, meaning that large grains of stacked Laponite crystals are still present. During the agitation the sodium ions release from the crystal interlayers, leaving free single charged Laponite crystals that have nanometric dimensions (see Fig. 2.2 (c)). After stirring the solution looks completely transparent like water. At this point the solution is filtered through a 0.45 μm filter directly inside the cuvette, the capillary or the rectangular quartz cell, that have different dimensions depending on the used scattering technique. This filtration process defines the starting waiting time ($t_w = 0$). To minimize CO_2 dissolution and sample degradation, all the cuvettes, capillaries and quartz cells were properly sealed with poly-(tetrafluoroethylene) (PTFE) tape or silicon inside the glove box under N_2 atmosphere. The same procedure was strictly followed to prepare all the samples in order to permit a correct comparison between the results.

Chapter 4

Results and Discussion

In this work, for the first time, a complete and systematic study of the Q-dependence of the aging dynamics and the effects of H_2O/D_2O isotopic substitution in the solvent for Laponite suspensions was performed by means of three dynamic scattering techniques, that cover a wide Q and time window, and by a static scattering experiment. For this purpose several samples in a clay concentration range of $(1.5 - 3.5\%)$ dispersed in both H_2O and D_2O solvents have been prepared.

We present evidences on how D_2O influences the aging and the final arrested structure of Laponite suspensions compared to H_2O. This study has a crucial importance not only for the improvement on the understanding of Laponite systems but also because the use of D_2O is unavoidable to gain contrast in Neutron Scattering (NS) techniques that will permit an enlargement of the available length and time scales.

A five channels Dynamic Light Scattering (DLS) setup has been built and employed as the main technique to investigate the dynamic properties of Laponite, in both solvents H_2O and D_2O, under aging. With this technique it was possible to access an exchange momentum range of $(6.2 \times 10^{-4} < Q < 2.1 \times 10^{-3}$ Å$^{-1})$ covering delay times of $(10^{-6} - 1$ s). By selecting the VV and VH components of the scattered light the translational and rotational degrees of freedom have been followed. The behavior of the dynamics as a function of C_w, t_w and Q were studied during the ergodic regime of the system. To extend the Q-range to $(3.1 \times 10^{-3} - 2.2 \times 10^{-2}$ Å$^{-1})$ and delay times to $(10^{-1} - 10^5$ s), X-ray Photon Correlation Spectroscopy (XPCS) technique was used. This technique permitted, through the ensemble-averaged time correlation functions, to investigate the slow dynamic properties of the system during the non-ergodic regime, not accessible by conventional DLS. To accomplish the dynamic study, Neutron Spin Echo (NSE) measurements were performed accessing an exchange momentum range of $(1.3 \times 10^{-2} < Q < 1.3 \times 10^{-1}$ Å$^{-1})$ and time window of $(3.7 \times 10^{-9} - 5.4 \times 10^{-7}$ s).

Finally, to understand the effects of H/D isotopic substitution on the arrested structures of Laponite systems and to investigate if the existence of two different arrested states (gel and glass) was preserved, the static structure factor was studied by Small Angle X-ray Scattering (SAXS) for high and low concentrated samples in both D_2O and H_2O solvents.

4.1 Dynamic Light Scattering Results of Laponite Suspensions in H_2O and D_2O Solvents

4.1.1 Aging Phenomenon

As discussed in chapter 2 the addition of Laponite in salt free water followed by a rapid agitation leads to the formation of a clear and transparent solution, with viscosity not so different from that of water. However, with time, the solution becomes spontaneously more and more viscous. This characteristic renders Laponite useful as thickener or stabilizer for many industrial applications such as household cleaning products, cosmetics, paints and many others. This behavior exists thanks to the positive and negative electric charges present on Laponite particles, that yields a complex competition between attractive and repulsive interparticle interactions. This viscosity increasing process is accompanied by a slowing down of the system dynamics, *i.e.* by the phenomenon of aging and the formation of multiple arrested states as amply discussed in chapter 2. Therefore the study of aging phenomenon in Laponite suspensions is important for industrial applications but especially to better understand the differences/similarities of gel and glass states and the role of competitive interactions. One of the most powerful technique to investigate the aging of colloidal systems is Dynamic Light Scattering (DLS) technique, which permits to probe the translational and rotational degrees of freedom of the system under measurement (see chapter 3).

Due to the typical dimension of the clay particles and the transparency of the sample, Laponite is an optimal system to be studied with DLS. As described in chapter 3, during this thesis we built a five channels DLS setup that consists basically on a solid state laser ($\lambda = 642$ nm, 100 mW) and five photomultiplier detectors placed at five fixed scattering angles. The main advantage of this new five channels DLS setup is the possibility to measure simultaneously the intensity correlation function at five Q-values. This is essential to investigate the aging at different Q since sample properties, as measured by correlation or response functions, change continuously on time and the comparison between dynamic informations at different Q must be acquired at the same t_w.

The typical behavior of the intensity correlation function obtained by means of DLS in a system performing aging is clearly observed in Fig. 4.1. This figure is an example, for the samples with $C_w = 3.0\%$ (left panels) and $C_w = 1.5\%$ (right panels) in H_2O (upper panels) and D_2O (lower panels), of how aging phenomenon is well signalled by the changes in the correlation functions acquired through channel 4 of the DLS setup, which corresponds to a Q-value of 1.8×10^{-3} Å^{-1}. For the samples with $C_w = 3.0\%$, the first measurement were obtained after 11 min (a) and 9 min (c) from sample filtration (defined as initial waiting time $t_w = 0$) and each subsequent displayed correlation curves were acquired at time intervals of $\sim$ 26 min (a) and $\sim$ 46 min (c), with increasing waiting time as indicated by the arrows. On the other hand the samples with $C_w = 1.5\%$ were first measured after 41 min (b) and 120 min (d) from sample filtration and each displayed subsequent curves were acquired at time intervals of $\sim$ 250 h (b) and $\sim$ 650 h (c). In these cases the slowing down of the correlation curves, evolving towards slower relaxation times is evident. It means that particles reduce their mobility, implying in a slower intensity fluctuation. After

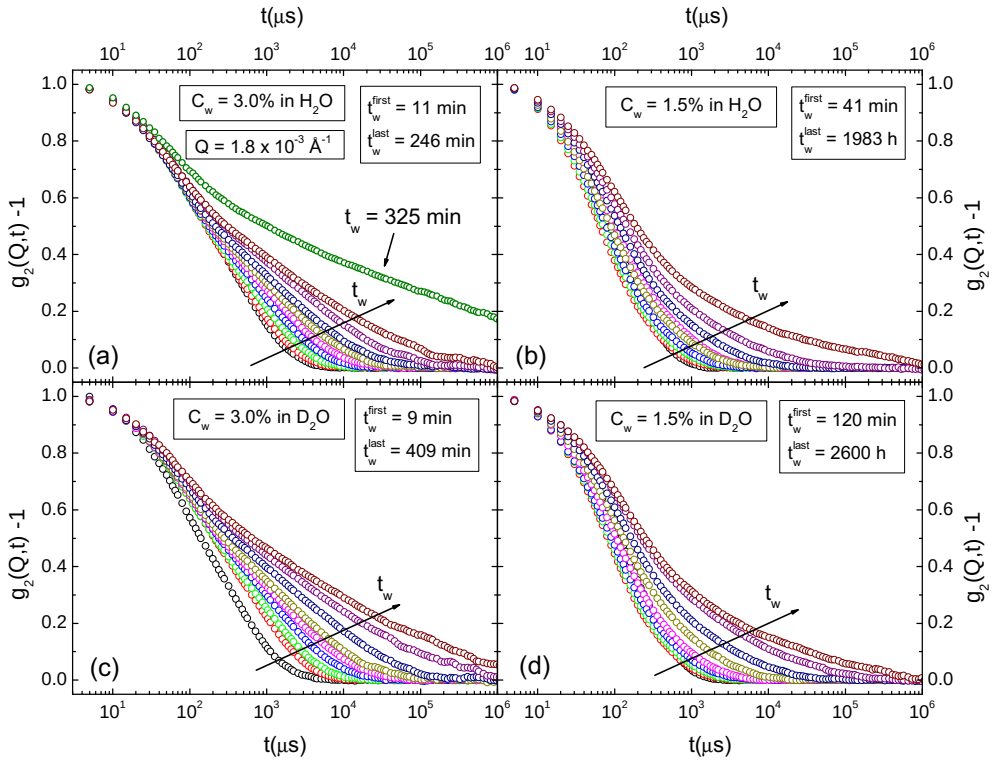

Figure 4.1. Waiting time evolution of intensity correlation functions for the samples with $C_w = 3.0\%$ (left panels) and $C_w = 1.5\%$ (right panels) in H_2O (upper panels) and D_2O (lower panels) at $Q = 1.8 \times 10^{-3}$ Å^{-1}. The arrows indicate increasing waiting times. A non-ergodic curve is also shown in panel (a) at $t_w = 325$ min as indicated by an arrow.

a certain waiting time, the intensity starts to be uncorrelated and the normalized correlation function no longer varies between one and zero, *i.e.* part of the degrees of freedom of the system is frozen on the time scale of the measurement. Those uncorrelated curves appear for waiting times larger than the last reported in Fig. 4.1 (t_w^{last}). An example of such uncorrelated curve, measured at $t_w = 325$ min, is shown in Fig. 4.1 (a) pointed by an arrow. The point in which the correlation curves start to be uncorrelated (t_w^{last} in Fig. 4.1) defines the moment in which the sample becomes non-ergodic in the measured time window, *i.e.* time-averaged correlation functions are not equal to their ensamble-averaged values.

Because of this spontaneously evolution of the intensity correlation function towards longer delay times, it was essential to control the integration time of acquisition, in order to ensure that the sample does not age significantly during a single measurement. For this reason, the integration time was varied for each sample according to the aging velocity and the quality of the signal.

During the ergodic regime, depicted in Fig. 4.1, the intensity correlation function ($g_2(Q,t)$) decays following a two steps behavior, *i.e.* there exist two different relaxation processes. The first one, observed for short delay times (t), is the fast

relaxation and seems to be practically independent on waiting time for the sample with $C_w = 3.0\%$, while it increases slightly for $C_w = 1.5\%$. On the other hand the second relaxation time, observed for longer delay times, is strongly dependent on waiting time for both concentrations and solvents, and increases faster for higher concentrated samples. Therefore, a significative fitting expression must contain two contributions.

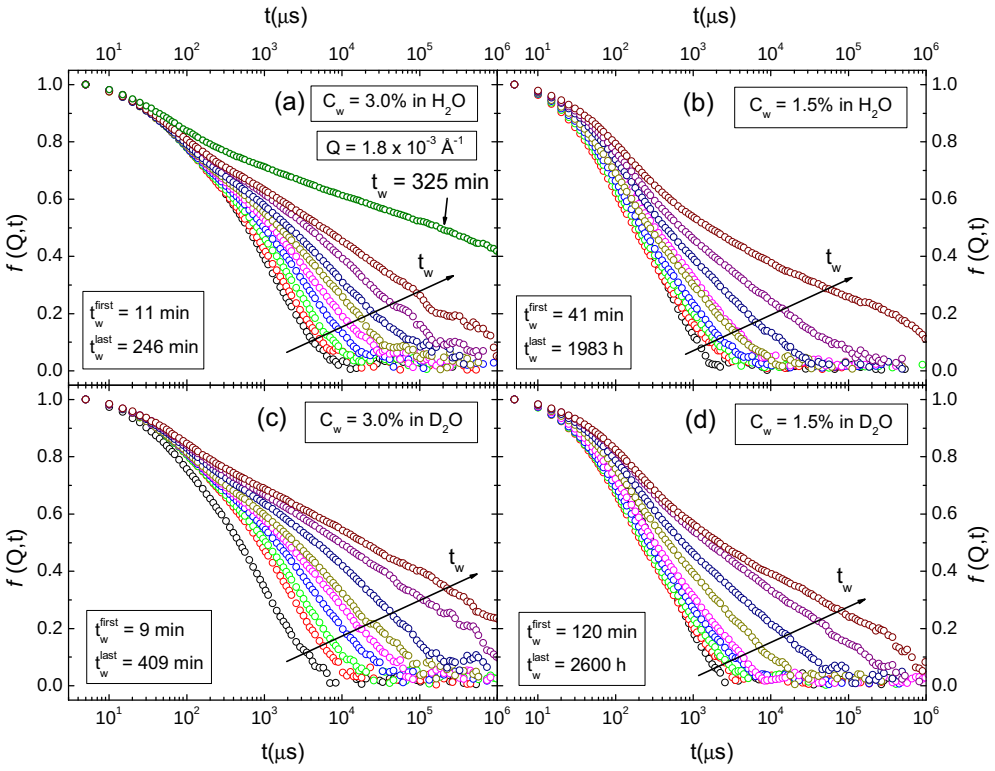

Figure 4.2. Waiting time evolution of the dynamic structure factor for the samples with $C_w = 3.0\%$ (left panels) and $C_w = 1.5\%$ (right panels) in H_2O (upper panels) and D_2O (lower panels) at $Q = 1.8 \times 10^{-3}$ Å^{-1}. The arrows indicate increasing waiting times. A non-ergodic curve is also shown in panel (a) at $t_w = 325$ min as indicated by an arrow.

A practical approach to describe the shape of the experimental correlation function is the sum of exponential functions. For a monodisperse system the decay of the time correlation function can be described by a single exponential of the form $g_1(Q,t) \sim \exp(-t/\tau)$, where the inverse of the relaxation time $\tau^{-1} = D_t q^2$ yields the translational diffusion coefficient D_t. This treatment describes very well the fast relaxation for Laponite data at short correlation times. However, for longer time scales, a large distribution of relaxation time arises and the corresponding time correlation function may be written as a superposition of many exponential decays in the form of a Fredholm equation of the first kind:

$$g_1(\mathbf{Q},t) = \int_0^\infty f(\tau) e^{-\frac{t}{\tau}} d\tau \tag{4.1}$$

where

$$\int_0^\infty f(\tau) d\tau = 1 \tag{4.2}$$

and $f(\tau)$ is the distribution of the relaxation times. Therefore, the corresponding time correlation function will be well described by a superposition of exponential decays. As predicted by theoretical models of glasses [86], the most portrayed relationship for correlation function data is composed by a sum of a single exponential and a stretched exponential decay:

$$g_2(\mathbf{Q},t) - 1 = b\left[a\exp\left(-\frac{t}{\tau_1}\right) + (1-a)\exp\left(-\left(\frac{t}{\tau_2}\right)^\beta\right)\right]^2, \tag{4.3}$$

were the parameters a and $(1-a)$ are the amplitude of the "fast" and "slow" relaxation modes respectively, b represents the coherence factor for the entire correlation curve, τ_1 is connected to the fast diffusive motion of particles in the sample, τ_2 is associated to the effective relaxation time related to a structural rearrangement and finally β, comprehended in the range $0 < \beta < 1$, is a measure of the distribution width of the slow relaxation times.

As seen in chapter 3 (see Eq. 3.36), from the measured intensity correlation function ($g_2(Q,t)$), one can obtain the dynamic structure factor ($f(Q,t)$) by using the Siegert relation:

$$f(\mathbf{Q},t) = \sqrt{\frac{g_2(\mathbf{Q},t) - 1}{b}}. \tag{4.4}$$

They can be fitted with the following expression

$$f(\mathbf{Q},t) = a\exp\left(-\frac{t}{\tau_1}\right) + (1-a)\exp\left(-\left(\frac{t}{\tau_2}\right)^\beta\right). \tag{4.5}$$

As an example, the dynamic structure factors associated with the correlation functions of Fig. 4.1 are shown in Fig. 4.2. From Figs. 4.1 and 4.2 it is possible to observe that the waiting time dependence of both relaxations was found to behave similarly in both solvents H_2O and D_2O for a fixed clay concentration. However, as displayed in the insets, the values of t_w^{last} for each sample are different, which indicate that the aging velocity is strongly affected by changing both clay concentration and solvent. This dependence will become more clear in the following sections.

4.1.2 Fast and Slow Relaxations

Laponite, like many other multidispersive systems, has a characteristic dynamic structure factor that can be well represented by a sum of a single exponential and a stretched exponential decay (Eq. (4.5)) where the first and second term carry the fast and slow relaxation parameters respectively.

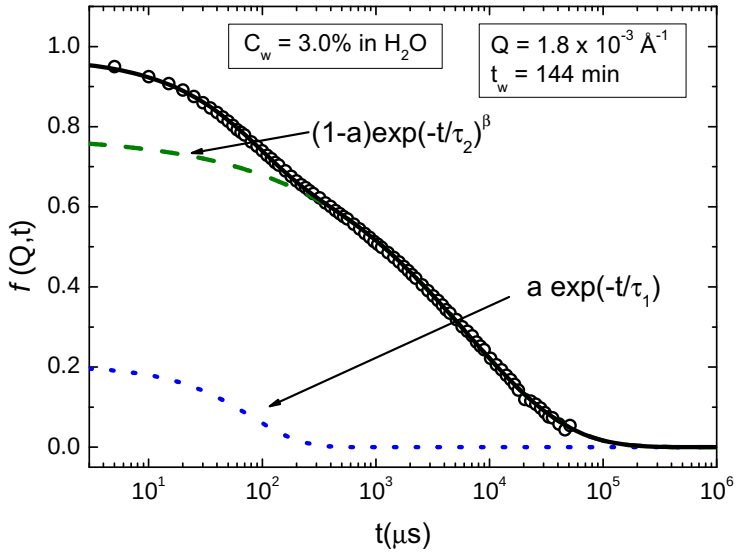

Figure 4.3. Dynamic structure factor of the sample with 3.0% in H_2O at $Q = 1.8 \times 10^{-3}$ Å^{-1} and waiting time $t_w = 144$ min (symbols) fitted with Eq. (4.5) (black full line). Blue dotted line represents the contribution of the first exponential term while green dashed line corresponds to the second exponential term.

Figure 4.3 shows an example, for a sample with $C_w = 3.0\%$ in H_2O at $t_w = 144$ minutes and $Q = 1.8 \times 10^{-3}$ Å^{-1}, of how each term of Eq. (4.5) contributes to the fitting of the dynamic structure factor. It is evident that, the first term ($a \exp(-t/\tau_1)$), displayed as a blue dotted line, gives the contribution of the fast relaxation process while the second term ($(1-a)\exp(-(t/\tau_2)^\beta)$), shown as a green dashed line, represents the slow relaxation of the system. The sum of these two contributions is shown in Fig. 4.3 by a black full line. The latter demonstrates that the double exponential expression (Eq. (4.5)) well describes the dynamic structure factor of Laponite systems. In the same way, Eq. (4.3) perfectly describes the intensity correlation functions of this system. Exactly like in H_2O, the same fast and slow relaxations were found in D_2O. In fact, the expression (4.3) was used to fit all data, regarding both H_2O and D_2O solvents, during the whole aging relative to the ergodic regime, obtaining always a low χ-square.

4.1.3 Waiting Time Dependence of Fitting Parameters

During the aging of the system the particles experience a strong change on their mobilities. This process is directly reflected on the time correlation functions that change their form as the time passes (Fig. 4.1). Therefore, each fitting parameter, obtained from Eq. (4.3), will be waiting time (t_w) dependent. In order to analyze this dependence we fitted, using expression (4.3), several time correlation curves acquired during the whole aging of the samples in the ergodic regime, *i.e.* up to when the sample become non-ergodic.

The parameters obtained by the fitting procedure are shown in Figs. 4.4 and 4.5 as a function of waiting time. As expected from Fig. 4.1, the fast relaxation time (τ_1) increases with t_w in different ways, depending mainly on clay concentration. In fact, Fig. 4.4 clearly depicts that τ_1 increases much faster for $C_w = 3.0\%$ compared with $C_w = 1.5\%$, which indicates that the aging velocity is directly proportional to clay concentration.

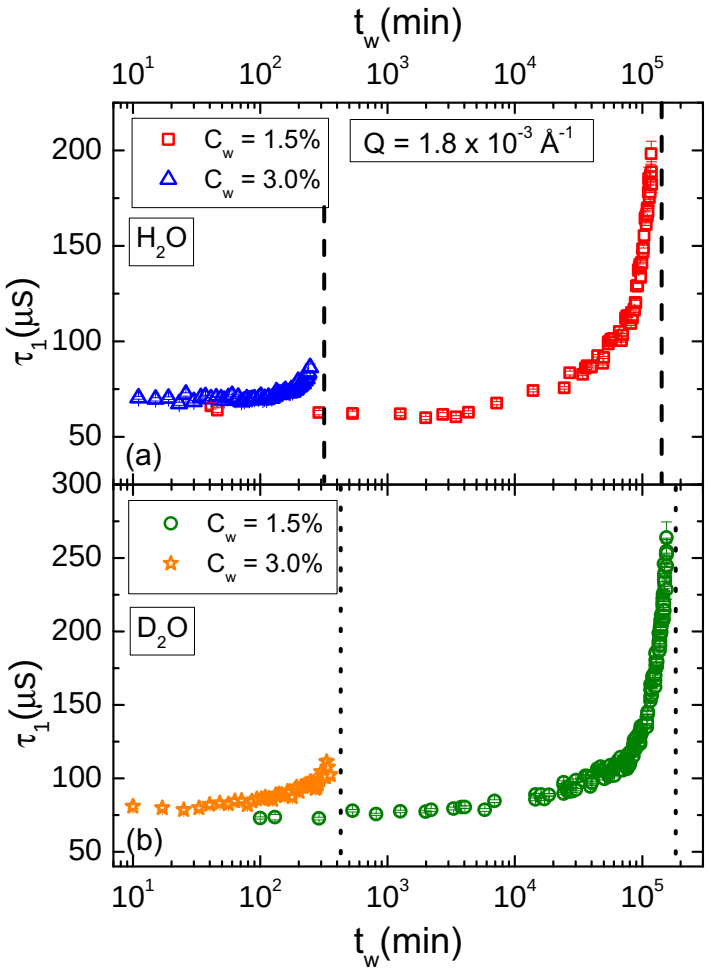

Figure 4.4. Waiting time evolution of parameter τ_1 for the samples with $C_w = 3.0\%$ (blue triangle and orange star symbols) and $C_w = 1.5\%$ (red square and green circle symbols) in (a) H_2O and (b) D_2O at $Q = 1.8 \times 10^{-3}$ Å^{-1}.

Figure 4.4 also shows that τ_1 departs from the same value for samples with different clay concentrations in a given solvent (H_2O or D_2O) and reaches higher values for low concentrated samples. In addition, Fig 4.4 shows that τ_1 has two clear differences between H_2O and D_2O solvents for a fixed clay concentration. Firstly, the initial values of τ_1 are slightly higher for D_2O compared to H_2O, and secondly, the waiting time evolution is different as can be observed by small shift between dashed (H_2O) and dotted lines (D_2O) *i.e.* the aging velocity changes. Since τ_1

is inversely related to the short-time translational diffusion ($D_t = 1/(\tau_1 Q^2)$), D_t depends on H/D isotopic substitution as it will be discussed later in this chapter.

On the other side the stretched exponential term describe the slow relaxation that depends both on the slow relaxation time (τ_2) and on the stretching parameter (β), therefore one can define a mean relaxation time τ_m from τ_2 and β. Assuming that the stretched exponential term is a weighted average of single exponentials with different relaxations, one has

$$\exp\left(-\left(\frac{t}{\tau_2}\right)^{\beta}\right) = \int_0^{\tau} f_{\tau_2,\beta}(\tau') \exp\left(-\frac{t}{\tau'}\right) d\tau', \tag{4.6}$$

where $f(\tau')$ is the distribution function of relaxation times. It can be shown that the mean relaxation time is given by:

$$\tau_m = \int_0^{\tau} \tau' f_{\tau_2,\beta}(\tau') d\tau' = \frac{\tau_2}{\beta}\Gamma\left(\frac{1}{\beta}\right), \tag{4.7}$$

where Γ is the Euler gamma function [54, 65]. An example of how τ_2, β and τ_m changes with waiting time is shown in Fig. 4.5 for the samples with $C_w = 3.0\%$ and $C_w = 1.5\%$ in H_2O and D_2O at $Q = 1.8 \times 10^{-3}$ Å^{-1}. The τ_2 parameter strongly increases with waiting time, while β decreases with t_w and generally depart from the same value (~ 0.8), in the whole studied clay concentration range, going down up to ~ 0.2. Similarly to τ_2, τ_m increases exponentially with t_w [54].

The significant growth with waiting time of both τ_2 and τ_m (clearly evident in Fig. 4.5 (a) and (c)) can be well described, for all studied clay concentrations and isotopic substitutions, by the general expression [54, 87]:

$$\tau_{2,m} = \tau_{2,m}^0 \exp\left(\frac{B}{1 - \frac{t_w}{t_w^{\infty}}}\right), \tag{4.8}$$

that describes also their divergency for a certain value of $t_w = t_w^{\infty}$ where the curve approaches a vertical asymptote, displayed in Fig. 4.5 by a dotted line for the case of D_2O and by a dashed line for the case of H_2O. This divergency is determined by the infinity waiting time parameter (t_w^{∞}) that corresponds to the time that the sample takes to reach the non-ergodic regime (arrested state). On the other hand the B parameter measures how fast τ_m approaches the divergency [54, 65].

From Fig. 4.5 it is clear that, for a fixed clay concentration, Laponite suspensions in D_2O solvents have a slower aging velocity compared to H_2O. As can be observed by the fact that the t_w^{∞} for H_2O samples (dashed lines) occurs before the t_w^{∞} for D_2O (dotted lines). The role of concentration and isotopic influence on the aging is better discussed in the following section.

4.1.4 Concentration and Isotopic Dependence of B and t_w^{∞}

In order to better investigate the concentration and isotopic dependence of the aforementioned parameters, that contain important dynamic informations, we prepared several samples in a clay concentration range of $(1.5 - 3.5\%)$, that covers gel and glass arrested states, in both H_2O and D_2O solvents. For each sample the whole aging of the system in the ergodic regime has been followed by measuring the

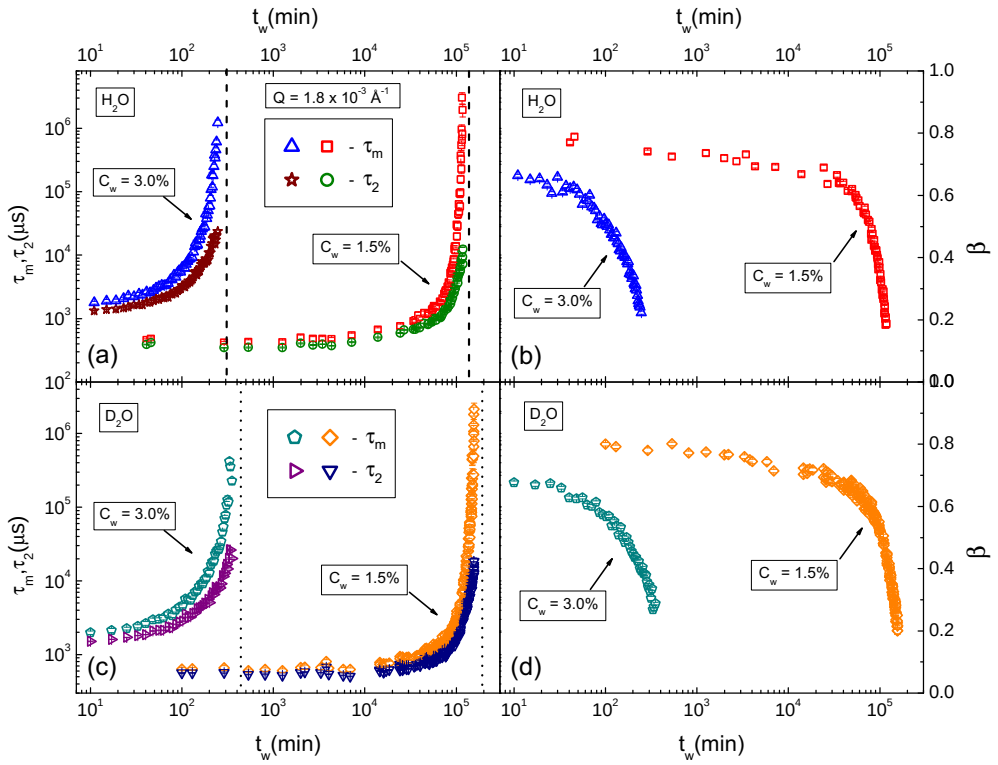

Figure 4.5. Waiting time dependence of τ_2, τ_m (left panels) and β (right panels) for the samples with $C_w = 3.0\%$ and $C_w = 1.5\%$ in H_2O (upper panels) and D_2O (lower panels) at $Q = 1.8 \times 10^{-3}$ Å^{-1}. Dashed and dotted lines represent the asymptote in which τ_2 and τ_m diverge.

correlation functions with DLS. Each curve has been fitted using Eq. (4.3), and the behavior of the parameters as a function of waiting time (t_w) and clay concentration (C_w) has been studied.

Figure 4.6 shows the values of τ_m as a function of t_w for all prepared samples in H_2O (a) and D_2O (b) at $Q = 1.8 \times 10^{-3}$ Å^{-1}. The figure clearly shows that the aging velocity strongly depends on clay concentration and that isotopic effects of D/H substitution also plays an important role. In fact, apart from $C_w = 2.3\%$ and $C_w = 3.5\%$, all the curves regarding D_2O solvent are shifted towards larger waiting times respect to H_2O for a fixed clay concentration. Besides, in agreement with what has been found by Ruzicka *et al.* in salt free water [54], Fig. 4.6 indicates that the shape of the curves seems to change by decreasing clay concentration in a similar way for both solvents.

To better visualize this concentration dependence, each curve has been fitted with Eq. (4.8) (represented by full lines in Fig. 4.6) and the parameters t_w^∞ and B have been studied as a function of clay concentration (C_w). By following the rigorous sample preparation procedure described in chapter 3 we could ensure a good sample reproducibility, which means in this case that similar values of t_w^∞ and B are found

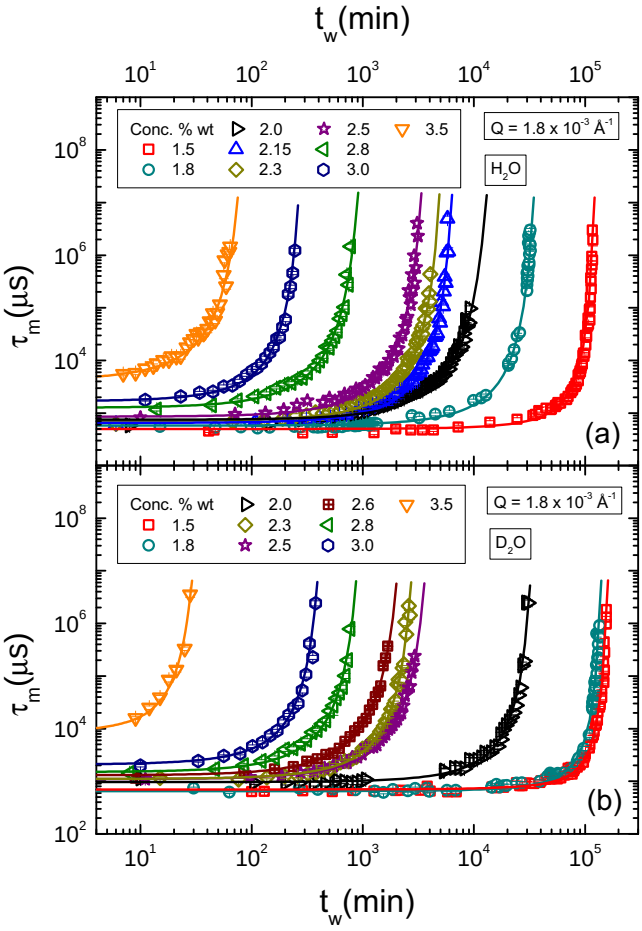

Figure 4.6. Mean relaxation parameter (τ_m) as a function of t_w for all the samples of Laponite dispersed in (a) H_2O and (b) D_2O at $Q = 1.8 \times 10^{-3}$ Å^{-1}. The clay concentrations are displayed in the legend. Full lines represent the fitting using Eq. (4.8).

for samples with the same clay concentrations and solvent. Figure 4.7 depicts a characteristic decreasing dependence of t_w^∞ on Laponite concentration for both type of solvents (H_2O and D_2O). Since the divergence waiting time (t_w^∞) well represents the time in which the sample makes the ergodic to non-ergodic transition, it is possible to conclude that more the sample is concentrated faster is the mechanism involved in the formation of arrested state. For instance, to obtain an equilibrium gel structure, that is formed in the clay concentration range of $1.0 < C_w < 2.0\%$ in salt free water ($C_s = 10^{-4}$ M) are necessary, as already found previously [14], waiting times in the order of thousands hours, *i.e.* a couple of months. On the other hand a Wigner glass, found for $2.0 \leq C_w \lesssim 3.0\%$ (see Ref. [14]), can be obtained much faster, with a time scale ranging from few to hundred hours. For concentrations higher than 3.0%, the aging process is so high that few minutes are enough for the sample to reach the arrested state whose nature has not been fully investigated yet.

For clay concentrations higher than $C_w = 3.5\%$, the samples evolve so quick that the structure arrests during stirring.

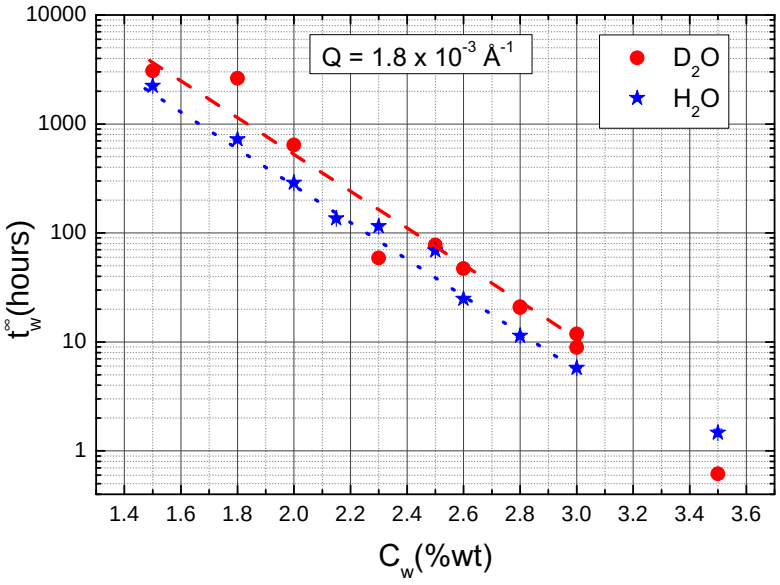

Figure 4.7. Clay concentration dependence of the divergence waiting time t_w^∞ for samples prepared in H_2O (blue stars) and D_2O (red circles) at $Q = 1.8 \times 10^{-3}$ Å^{-1}. The dotted and dashed lines are only guide for eyes.

Despite of the clay concentration dependence of the divergence waiting time, it is worth to observe a considerable difference between aging velocities, regarding samples with the same clay concentrations in both solvents (H_2O and D_2O), that is evident from Fig. 4.7. A slower aging behavior of samples prepared in D_2O solvent respect to H_2O is found for most of the samples prepared in this work. In the gel and Wigner glass region ($1.5 \leq C_w \lesssim 3.0\%$) it was possible to differentiate two t_w^∞ dependences on C_w that can be observed by the red dashed line for D_2O and blue dotted line for H_2O. The explanation for this slowing down of the aging with isotopic substitution might be associated with small differences between physical properties of D_2O and H_2O. The most probable reason for this difference is the higher dynamic viscosity of D_2O compared to H_2O. In fact the dynamic viscosity of D_2O is $\sim 20\%$ higher than that of H_2O, which, according to the Stokes-Einstein relation (Eq. (3.47)), reduces significantly the mobility of particles in the system, increasing the time that the particles need to reach the arrested state.

The B parameter, shown in Fig. 4.8 as a function of C_w, present a discontinuity (step behavior) for both solvents H_2O and D_2O. For Laponite in salt free water, this discontinuity is found at $C_w \sim 1.8\%$, and well represents the transition between gel and Wigner glass [54]. B presents a discontinuity (step behavior) between two different constant values for low and high clay concentrations, in agreement with previous results in H_2O solutions [54]. By making H/D isotopic substitutions Fig.

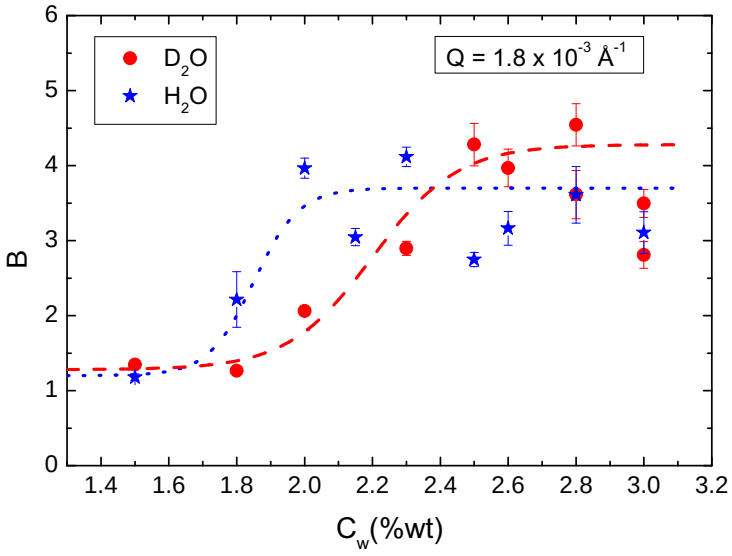

Figure 4.8. Clay concentration dependence of the B parameter for samples prepared in H_2O (blue stars) and D_2O (red circles) at $Q = 1.8 \times 10^{-3}$ Å^{-1}. The dotted and dashed lines are only guide for eyes.

4.8 shows the same behavior as in the case of H_2O with only a slight shift of the discontinuity in B towards high clay concentrations. Therefore, independently of this small shift behavior, displayed in Fig. 4.8, the transition between two different arrested states is probably unchanged for both solvents.

4.1.5 Scaling Laws

The existence of two well divided regions for the B parameter as a function of clay concentration, where B remains almost constant at low- and high-values (Fig. 4.8), indicate the possibility of a scaling law. In order to investigate this possibility, the waiting time axis of each sample was divided by its own divergence time (t_w^∞).

Figure 4.9 (right panels) shows the scaling behavior for the parameters τ_m and β reported in left panels as a function of t_w for all the samples of Laponite dispersed in D_2O. The collapse of all the curves on two master curves, one for low and other for high concentration, is impressive. This happens not only for the case of H_2O, as expected [54], but also for D_2O, giving a clear indication that the picture of a gel and glass state remains valid for both solvents. It is important to stress that the curve corresponding to the sample $C_w = 2.0\%$ in Fig. 4.9 is placed in the middle of the two master curves since its B parameter has an intermediate value between low and high values (see Fig. 4.8).

Clearly a direct evidence of this indication can be obtained only through a measure of the static structure factor evolution with waiting time as it will be discussed in section 4.4.

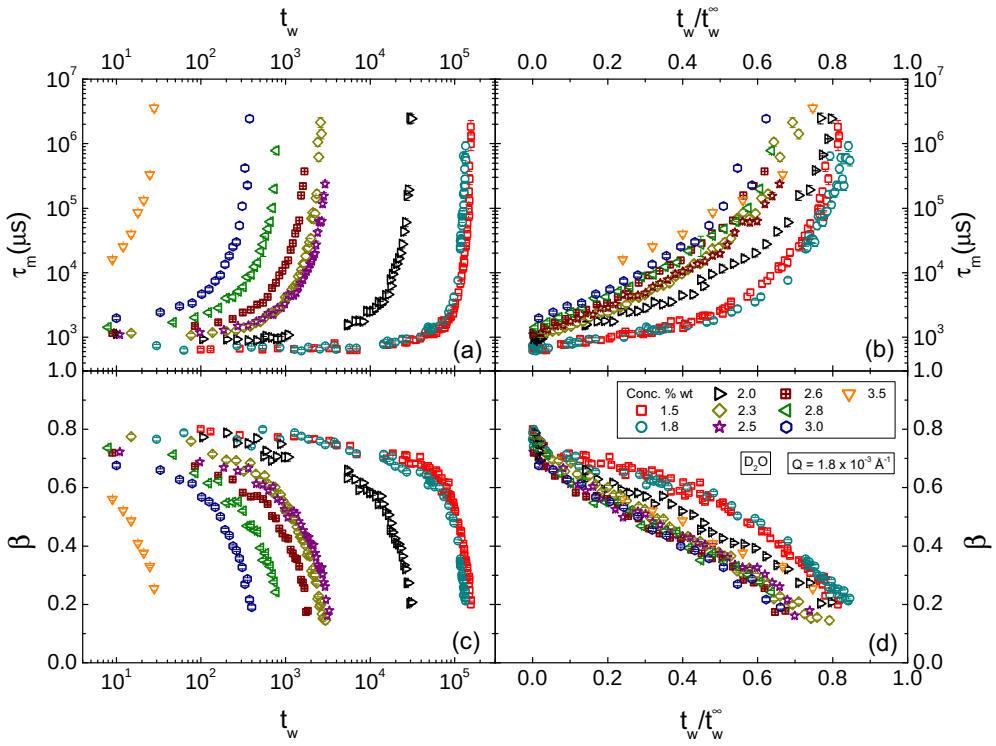

Figure 4.9. Aging evolution of (a) τ_m and (c) β for all the samples of Laponite dispersed in D_2O at $Q = 1.8 \times 10^{-3}$ Å^{-1}. Right panels represent the same parameters reported in the left panels in function of the scaled waiting time (t_w/t_w^∞).

4.1.6 Q-dependence of the Characteristic Parameters

The five channels DLS setup used in this work permits the simultaneous acquisition of intensity correlation functions at five different Q-values and allowed to perform the first systematic investigation (in function of clay concentration and isotopic substitution) of the Q-dependence of aging phenomenon in Laponite systems. During the alignment of this setup (described in chapter 3), the angular position of each channel was fixed at $\sim 30°$, $50°$, $70°$, $90°$ and $110°$. The knowledge of the laser wavelength, the refractive index of the solvent and the angles of each channel, and the use of the expression $Q = 4\pi n/\lambda \sin(\theta/2)$ permits to calculate the value of the exchanged momentum that is $Q = 6.2 \times 10^{-4}$, 1.1×10^{-3}, 1.5×10^{-3}, 1.8×10^{-3} and 2.1×10^{-3} Å^{-1} for each angle respectively. Figure 4.10 shows, as an example, the correlations curves for a "young" sample ($t_w = 11$ min) with $C_w = 3.0\%$ in H_2O at different Q-values. The curves maintain their forms but are shifted towards high delay times (slow dynamics) for small Q. This behavior characterizes a strong Q-dependence of the relaxation times.

Following the same data analysis procedure described previously, all correlation curves, at different waiting times for the five channels, were fitted using Eq. (4.3). Figure 4.11 shows the waiting time evolution of the characteristic parameters at five

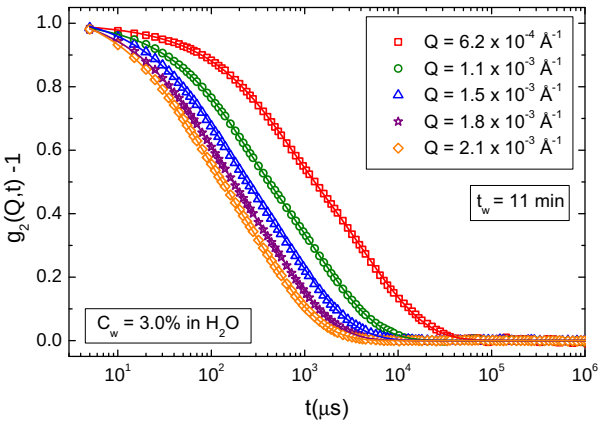

Figure 4.10. Intensity correlation functions for the sample with $C_w = 3.0\%$ in H_2O at $t_w = 11$ min and five different Q-values displayed in the legend. Full lines are the fitting curves obtained through Eq. (4.3).

different Q-values. As previously deduced from the correlation functions shown in Fig. 4.10, both relaxation times τ_1 and τ_2 have a strong dependence on the exchanged momentum, increasing for smaller Q. This behavior persists during the whole waiting time evolution measured for each sample in the ergodic regime. As clearly evidenced in Fig. 4.11 (b), the β parameter does not show any Q-dependence during the aging, decaying linearly with the same rate for all exchanged momentum. Since τ_m depends on both τ_2 and β, we expect τ_2 and τ_m to have the same Q-dependence.

Another important point to be emphasized here is the different waiting times in which each Q perceives the ergodic to non-ergodic transition. Figure 4.11 shows that the last parameter obtained in the ergodic regime at $Q = 6.2 \times 10^{-4}$, 1.1×10^{-3}, 1.5×10^{-3}, 1.8×10^{-3} and 2.1×10^{-3} Å^{-1} was acquired at $t_w = 171$, 209, 235, 246 and 265 minutes respectively. This is related to the fact that looking at smaller Q-values corresponds to investigate larger spatial scales (larger structures) which get stuck earlier respect to smaller scales probed at higher Q-values. Despite this difference, the waiting time evolution of τ_m has the same exponential increasing behavior, described by Eq. (4.8), for all Q-values and diverges at a very similar waiting time as shown in Fig. 4.11 (d). In fact, Fig. 4.12 (a) clearly shows that the divergence waiting time (t_w^∞) is quite similar for the five studied Q-values, having a mean value of 367 minutes and a standard deviation of 22 minutes. For this reason the picture of t_w^∞ in function of clay concentration shown in Fig. 4.7 for $Q = 1.8 \times 10^{-3}$ Å^{-1} remains unchanged for the other Q-values probed by DLS. On the other hand the B parameter seems to follow the same trend presented by t_w^∞, fluctuating around a mean value of 3.3 with a standard deviation of 0.5 (Fig. 4.12 (b)). However, this fluctuation has been found to be strongly reduced for decreasing clay concentrations. Independently on the Q-value the discontinuity behavior found in Fig. 4.8 is maintained at the same t_w, changing only the height of the step.

The real exchanged momentum dependence of Laponite suspensions during aging can be understood by investigating the characteristic parameters obtained through

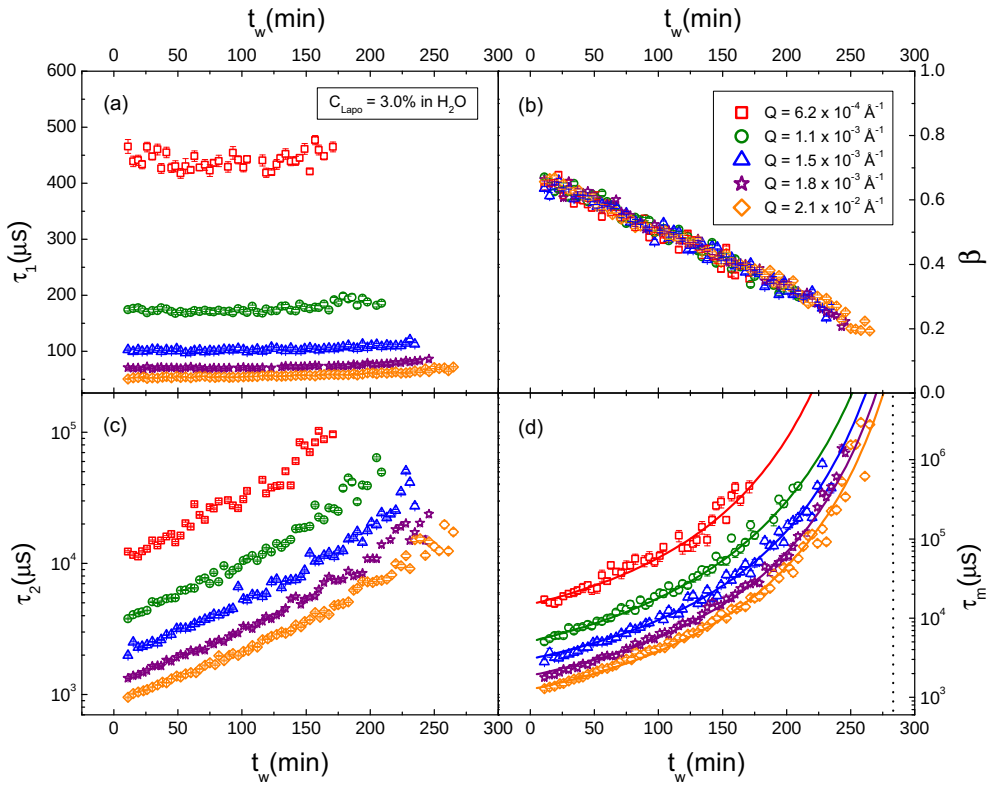

Figure 4.11. Waiting time dependence for the five measured Q-values of (a) τ_1, (b) β, (c) τ_2 and (d) τ_m for the sample with $C_w = 3.0\%$ in H_2O. Full lines in (d) represent the fitting curves obtained through Eq. (4.8). Dotted line in (d) represents the vertical asymptotic in which the mean relaxation times diverge.

Eq. (4.3) as a function of Q for each waiting time. As an example, the parameters τ_1, τ_2 and τ_m shown in Fig. 4.11 are plotted in Fig. 4.13 as a function of Q at four different waiting times spaced of ~ 52 minutes. The aging behavior is evident, once again, τ_1 does not change significantly with waiting time while τ_2 and τ_m strongly increase with t_w.

As already mentioned, τ_1, τ_2 and τ_m maintain a strong Q-dependence during the whole aging, changing their values with the evolution of waiting time. On the contrary, the β parameter, as evident in Fig. 4.11 (b), remains always unchanged with Q, decreasing only with t_w. The Q-dependence of the parameters τ_1, τ_2 and τ_m was found to be well described, for all acquired data during whole measured waiting times, by a power law expression:

$$\tau_1, \tau_2, \tau_m = a \cdot Q^{n\tau_1, n\tau_2, n\tau_m}, \tag{4.9}$$

as clearly shown in Fig. 4.13 by solid lines that represent the fitting curves of data obtained through Eq. (4.9).

Right panels of Fig. 4.13 show the waiting time dependence of the power law

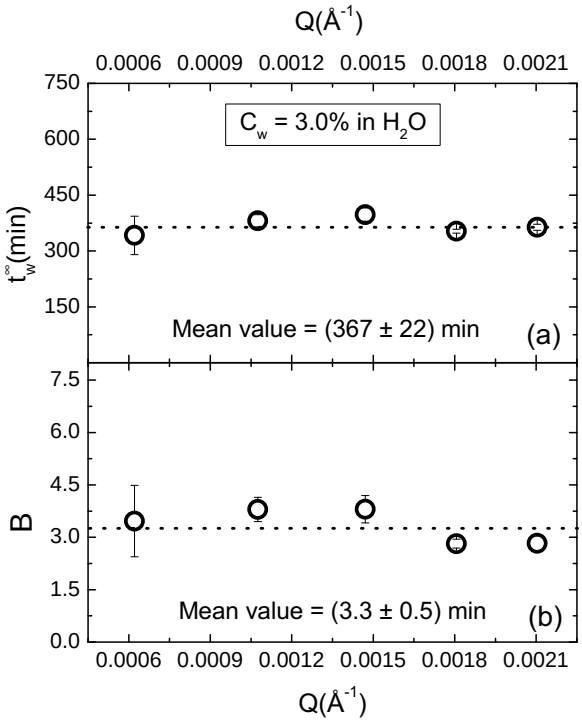

Figure 4.12. (a) t_w^∞ and (b) B parameter as a function of Q for the sample with $C_w = 3.0\%$ in H_2O. The horizontal dotted line represents the position of the mean value.

exponents, $n\tau_1$ (d), $n\tau_2$ (e) and $n\tau_m$ (f), for the same sample shown as an example. It is possible to observe that all these exponents are waiting time invariant and have a mean value of (1.71 ± 0.04), (2.15 ± 0.23) and (2.22 ± 0.35) for $n\tau_1$, $n\tau_2$ and $n\tau_m$ respectively. From this figure one can note that the noise of $n\tau_1$, $n\tau_2$ and $n\tau_m$ is increased for increasing waiting times. This behavior is more pronounced for $n\tau_m$ and can be evidenced by the increasing of the standard deviations obtained during the complete aging, that are 0.04, 0.23 and 0.35 for $n\tau_1$, $n\tau_2$ and $n\tau_m$ respectively. This behavior is related to the increasing of fluctuations for the parameters τ_1, τ_2, τ_m and β at large waiting times (see Fig. 4.11). In fact while t_w increases, the mobility of the particles decreases due to the "cages" formed by their neighbours and a part of the degrees of freedom of the system starts to become unchanged on the time scale of the measurements. During this stage, the scattered intensity starts to become uncorrelated and the fluctuations of the characteristic parameters initiate to increase.

In addition to the waiting time invariance of the power law exponents shown in Fig. 4.13, we found that these exponents remain unchanged for all the studied samples in both solvents. Figure 4.14 shows the mean values of $n\tau_1$, $n\tau_2$ and $n\tau_m$, calculated over the whole waiting time, as a function of clay concentration dispersed both in H_2O and D_2O. It is evident that the power law exponents do not depend on Laponite concentration, remaining constant around a mean value 1.67/1.68, 2.08/2.11 and 2.07/2.17 for $n\tau_1$, $n\tau_2$ and $n\tau_m$ in D_2O/H_2O respectively. The values

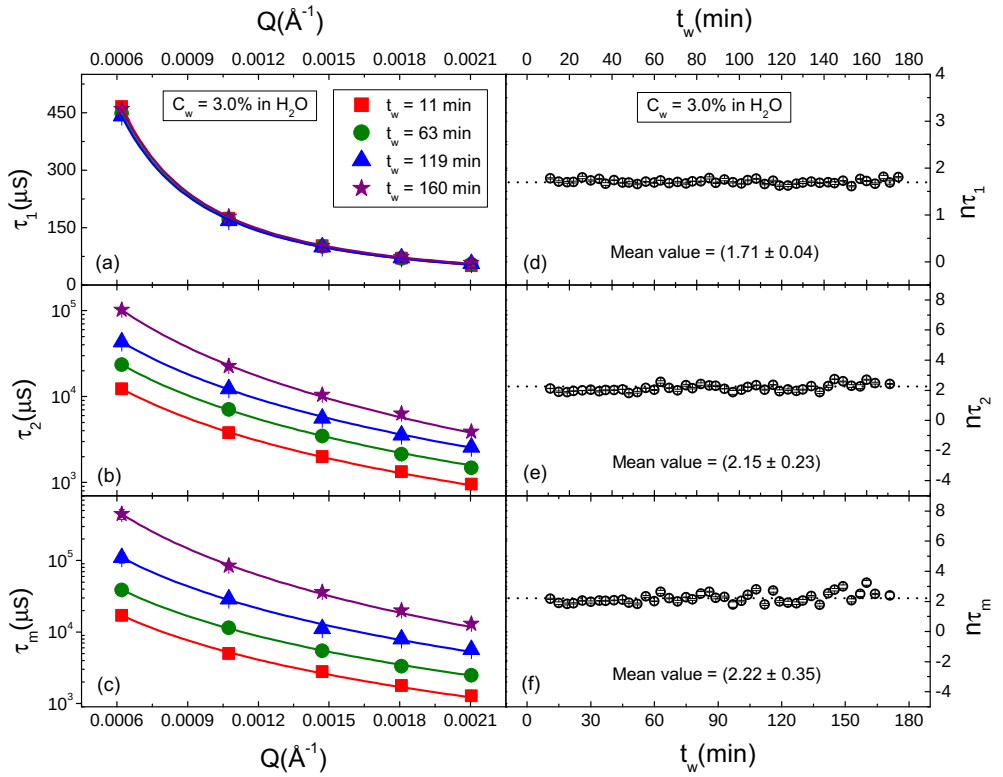

Figure 4.13. Q-dependence of characteristic parameters (a) τ_1, (b) τ_2 and (c) τ_m for sample with $C_w = 3.0\%$ in H_2O at four different waiting times displayed in the legend. Full lines in (a), (b) and (c) represent a power law fitting curves obtained using Eq. (4.9). Waiting time dependence of the power law exponents (d) $n\tau_1$, (e) $n\tau_2$ and (f) $n\tau_m$. The horizontal dotted lines represent the position of the mean value displayed in the inset of each panel.

of the power law exponents found for the sample with $C_w = 3.5\%$ is significantly different from the others. This can be due to the very fast aging of this concentration, which gives consequently to a considerable error due to big fluctuations of τ_1, τ_2, τ_m and β even at short waiting times or to the existence of a different regime since for this concentration the sample has been supposed to be in a nematic order [50].

The presence of a Q-dependence of the relaxation times determines the characteristic diffusion process present in the system. As well known, when dynamic properties scales as $\propto Q^{-2}$ particles motion is described by Brownian motion. In the case of glassy system, the diffusion of particles can be described as a "cage" diffusion process with the presence of two relaxation times. The first one, τ_1, characterizes the short-time diffusion of a particle in the suspending medium. At short delay times, the particle diffuses "freely" within the "cages" formed by the surrounding particles. This diffusion depends weakly on waiting time, as shown in Fig. 4.11 (a), and was found to scale as $\tau_1 \propto Q^{-2}$ at short waiting times for few concentrated samples (in the glass concentration range) in H_2O solvent [58, 88, 89, 90]. Although

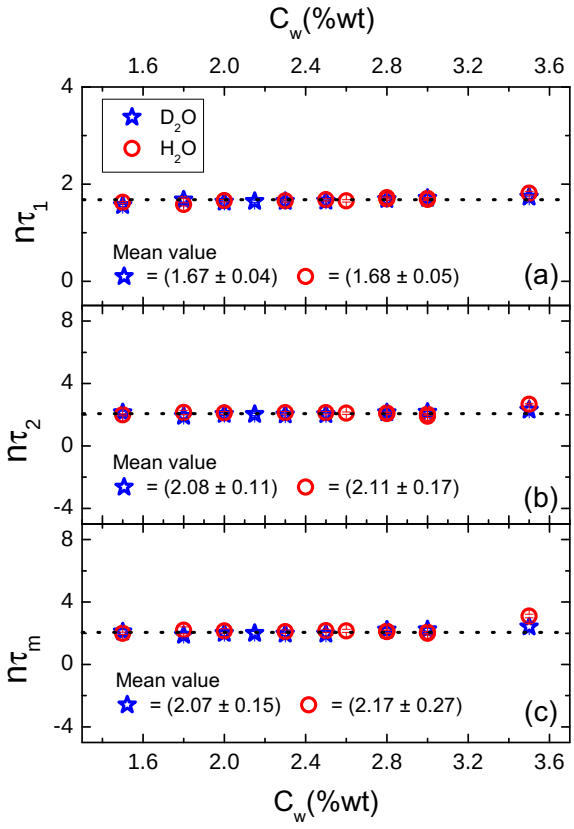

Figure 4.14. Clay concentration dependence of the power law exponents: (a) $n\tau_1$, (b) $n\tau_2$ and (c) $n\tau_m$. The horizontal dotted lines represent the position of the mean value displayed in the inset of each panel.

the lower values of the exponent $n\tau_1 \sim 1.7$ found (see Fig. 4.14 (a)), the short-time dynamics can be still represented by a Brownian diffusion process. The second relaxation process, that occurs for long time delay, can be interpreted by the structural rearrangement of the system, *i.e.* the escape of particles from the "cages". As shown previously, τ_2 increases dramatically with t_w, indicating that it becomes more and more difficult for a particle to "escape" from the formed "cages". In agreement to the mean value exponent $n\tau_2 \sim 2.1$ reported in Fig. 4.14 (b), this characteristic relaxation time has been also found to scale as $\tau_2 \propto Q^{-2}$ at short waiting times in the case of H_2O [88, 90, 91], a feature again reminiscent of classical diffusion. However, this slow diffusive motion is complex as it is characterized by a broad distribution of relaxation times, leading to the stretched behavior of the slow exponential decay in the correlation functions (Eq. (4.3)). For this reason a systematic investigation for several concentrated samples at several waiting times, as reported in this work, is essential. Besides, dynamical effects of a charged colloidal systems during aging have never been systematically exploited by making H/D isotopic substitution in the solvent.

The evidences presented in Fig. 4.11 (b) that the stretching parameter β, which

measures the distribution width of the slow relaxation time, is Q-independent has been also reported by Abou *et al.* [88]. This parameter depends only on the waiting time and this explains the reason why τ_m scales as $\tau_m \propto Q^{-2}$, exactly like τ_2.

By treating the system as a "cage" diffusion process, it follows immediately that at short waiting times the particles are able to escape from the "cages" after a characteristic time that strongly depends on t_w. If this characteristic time is lower than the time scale of the measurements, the system is defined ergodic. As the system ages, the escape from the "cages" become slower and slower. The particles are subsequently constrained by the "cages", resulting in the ergodicity breaking within the observation time scale. After the ergodicity breaking of the system, *i.e.* waiting times longer than t_w^{∞}, the particles are no longer escaping from the "cages" during the measurement time scale, and consequently the Q-dependence should not be described by $\propto Q^{-2}$. In fact, the works of Schosselet *et al.* and Pujala *et al.* report that in the non-ergodic regime the slow relaxation time (τ_2) scales as $\propto Q^{-1}$ and no longer represents the diffusive motion of the particles [90, 91]. During the non-ergodic regime the normalized correlation function does not decay to zero and exhibits a pseudo plateau. This indicates that conventional DLS experiments do not probe large enough time scales to measure the longest relaxation time of the system and the results are no longer reliable since only ensemble average measurements make sense.

4.1.7 Dynamics Light Scattering Results in VH Configuration

Dynamic light scattering is a powerful technique widely used to probe dynamic properties of colloidal systems. The translational and rotational diffusion of Laponite particles can be investigated by means of polarized and depolarized light scattering. As explained in chapter 3, when the laser light (vertically polarized) impinges on the sample it is scattered by the suspended particles that can change or not the original polarization. The total electric field scattered by the particles is composed by two components, a vertically polarized component (E_{VV}), with amplitude proportional to the average between the polarizabilities parallel and perpendicular to the optical axis ($\alpha = (\gamma_{\parallel} + 2\gamma_{\perp})/3$), and a horizontal depolarized component (E_{VH}) proportional to the intrinsic particle anisotropy ($\beta = \gamma_{\parallel} - \gamma_{\perp}$) [69]. Here β is called optical anisotropy or the anisotropic part of the polarizability and for spherical particles $\gamma_{\parallel} = \gamma_{\perp}$ and $\beta = 0$.

A depolarized (VH) time correlation function can be obtained by selecting only the horizontal polarized scattered light through an optical polarizer. This correlation function (g_2^{VH}) contains informations about translational and rotational diffusion of the particles. On the other hand, the polarized (VV) time correlation function, analyzed up to this point, also contains informations about translational and rotational degrees of freedom, however, the rotational contribution to g_2^{VV} is proportional to $\frac{4}{3}\frac{I_{VH}}{I_{VV}}$. Since the VV intensity is much higher compared to VH, g_2^{VV} mainly reflects the translational diffusion of the particles. In fact, by measuring the photon counts for VV and VH configurations, we obtain a signal of 58k counts/second for VV and about 300 counts/second for VH. Thus, contribution of rotational motion to VV correlation is lower than 0.01 and can be considered negligible.

To compare the waiting time dependence of the characteristic parameters obtained

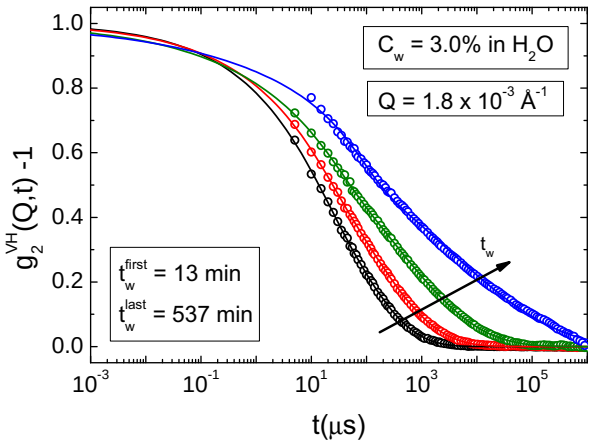

Figure 4.15. Waiting time evolution of depolarized (VH) intensity correlation functions for the sample with $C_w = 3.0\%$ in H_2O at $Q = 1.8 \times 10^{-3}$ Å^{-1}. Full lines represent the fitting curves obtained through Eq. (4.3).

from g_2^{VV} and g_2^{VH}, we prepared a sample with $C_w = 3.0\%$ in H_2O and divided the final suspension in two different vials. One was measured in VV configuration by means of a standard single angle DLS setup (at 90°), and the other in VH configuration by using the already described five channels DLS setup with three optical polarizers selecting the horizontal polarization of the scattered light, *i.e.* I_{VH} at 30°, 90° and 110° and I_{VV} at 50° and 70°. The two parts of the sample were measured simultaneously in time periods equally spaced at same temperature (24° Celsius).

As an example, Fig. 4.15 shows the waiting time evolution of depolarized (VH) intensity correlation functions for the sample with $C_w = 3.0\%$ in H_2O at $Q = 1.8 \times 10^{-3}$ Å^{-1} (90°). Using the same analysis procedure explained previously we fitted all the polarized and depolarized correlation curves with the double exponential expression (Eq. (4.3)) that well describes also the g_2^{VH} as can be observed by the full lines in Fig. 4.15.

The comparison between the characteristic parameters obtained from g_2^{VV} and g_2^{VH} at $Q = 1.8 \times 10^{-3}$ Å^{-1} (90°) are shown in Fig. 4.16. Both the fast (τ_1) and the slow (τ_2) relaxations are found to have roughly the same aging behavior in both modes with the difference that VV has always higher values, as expected. On the contrary, the β parameter presents different evolutions with t_w, departing from smaller values and decaying slowly for the depolarized (VH) signal. τ_m shows only a small difference between (VV) and (VH), which consequently make the divergence waiting time (τ_w^∞) and the B parameter to be slightly different in VV and VH modes. In fact Fig. 4.17 shows that the values of t_w^∞ and B are always overestimated in VH mode. This difference might be caused by the fact that rotational degree of freedom starts to play a role in VH signals, giving an important contribution to the depolarized intensity correlation functions.

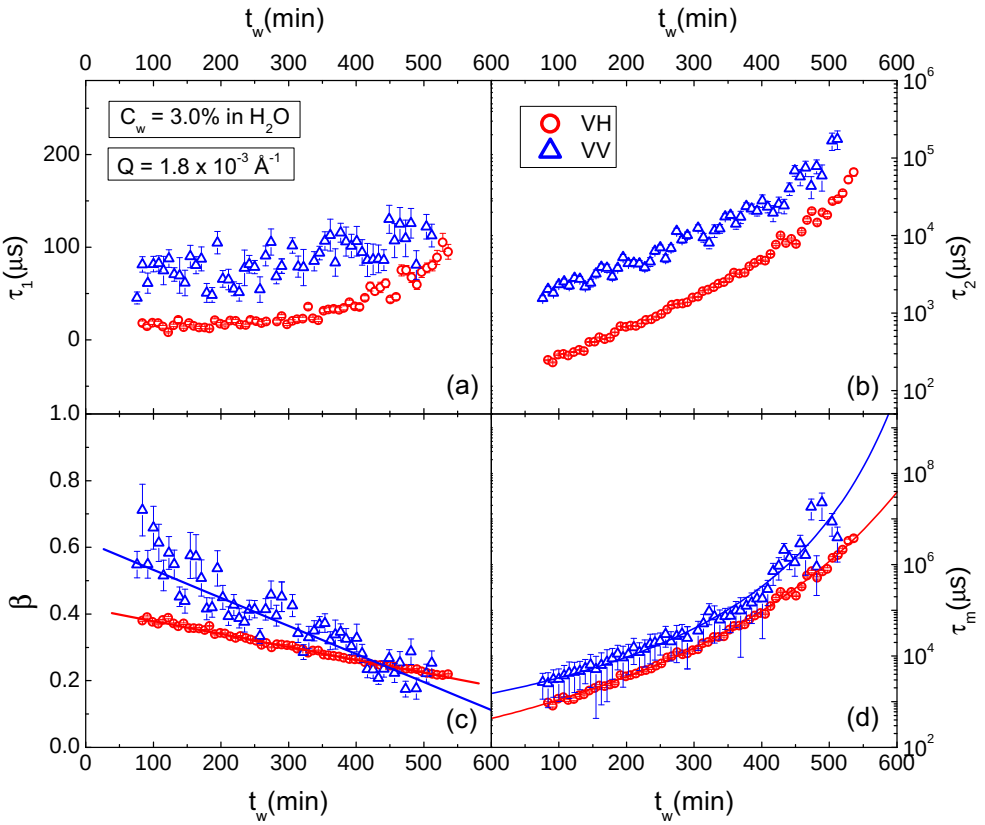

Figure 4.16. Comparison between the waiting time evolution of (a) τ_1, (b) τ_2, (c) β and (d) τ_m acquired in a VV and VH configuration for the sample with $C_w = 3.0\%$ in H_2O at $Q = 1.8 \times 10^{-3}$ Å^{-1}. Full lines in (b) and (d) represent the fitting curves obtained through linear and Eq. (4.8) expressions respectively.

4.1.8 Rotational and Translational Diffusion Coefficients

Polarized (VV) intensity correlation functions have been recorded for a large number of clay concentrations (C_w) and waiting times (t_w) at five different exchanged momentum (Q). On the other hand depolarized (VH) signals were collected at three different angles (30°, 90° and 110°) during the aging of two samples with $C_w = 3.0\%$ and $C_w = 2.8\%$ in H_2O.

At small Q-values considered here ($6.2 \times 10^{-4} \leq Q \leq 2.1 \times 10^{-3}$ Å^{-1}), the relaxation rates in VV and VH modes can be expressed as $1/\tau_{VV} = D_t Q^2 + \mathcal{O}(Q^4)$ and $1/\tau_{VH} = 6D_r + \mathcal{O}(Q^2)$ respectively, where D_t and D_r are respectively the translational and rotational diffusion coefficients [69]. Contributions of $\mathcal{O}(Q^4)$ to τ_{VV}, which arises from rotational diffusion and rotational-translational coupling, have no relevance for the considered small Q-values, as demonstrated before [69]. However, contributions to τ_{VH} of $\mathcal{O}(Q^2)$ comes from the translational degree of freedom, and can be expressed by $D_t Q^2$. Therefore, to compute the translational

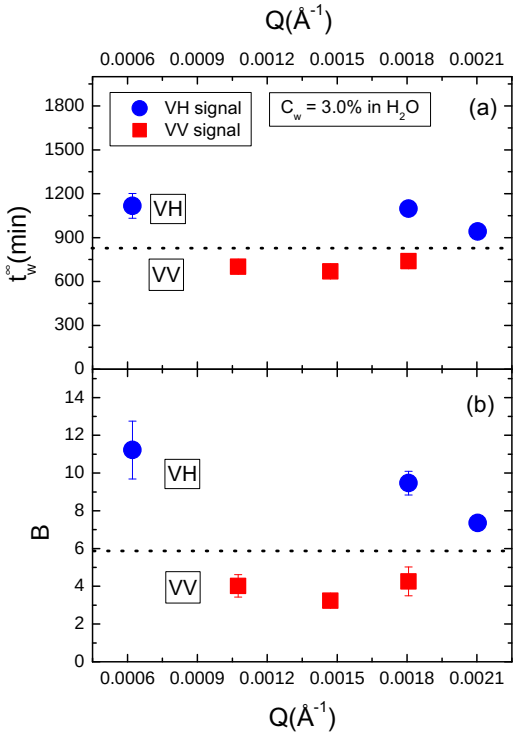

Figure 4.17. (a) t_w^∞ and (b) B parameter as a function of Q for the sample with $C_w = 3.0\%$ in H_2O acquired in a VV and VH configuration. The horizontal dotted line is dividing the data obtained through VH (above) and VV (below) configurations.

diffusion coefficient of suspended particles, one needs only the relaxation time from the polarized time correlation function. On the other hand, values of the rotational diffusion coefficient should be obtained by extracting the contribution of D_t from g_2^{VH}, *i.e.*

$$D_r = \frac{1}{6}\left(\frac{1}{\tau_1^{VH}} - \frac{1}{\tau_1^{VV}}\right). \tag{4.10}$$

The values of the polarized fast relaxation time τ_1^{VV} were obtained by fitting the VV time correlation functions with Eq. (4.3) (see Fig. 4.10). To ensure that the fast relaxation time is not getting any contribution from the exponentially growth of τ_2^{VV}, we used the Siegert relation (Eq. (4.4)) to obtain the dynamic structure factors ($f^{VV}(Q,t)$), and fitted them with Eq. (4.5). From this expression τ_1^{VV} and τ_2^{VV} are completely decoupled (as shown in Fig. 4.3), and give separated contributions to the fast and slow motions respectively. We found that the characteristic parameters obtained from $f^{VV}(Q,t)$ and $g_2^{VV}(Q,t)$ follow the same waiting time dependence and have a good quantitative agreement deviating only slightly for longer waiting times. Therefore, we used directly the fast relaxation times, obtained through g_2^{VV}, to calculate the short-time translational diffusion coefficient, *i.e.* $D_t = 1/(\tau_1^{VV}Q^2)$.

Figure 4.18 shows the aging dependence of D_t for the sample with $C_w = 3.0\%$ in H_2O at five scattering wave numbers. It is evident that the translational degree

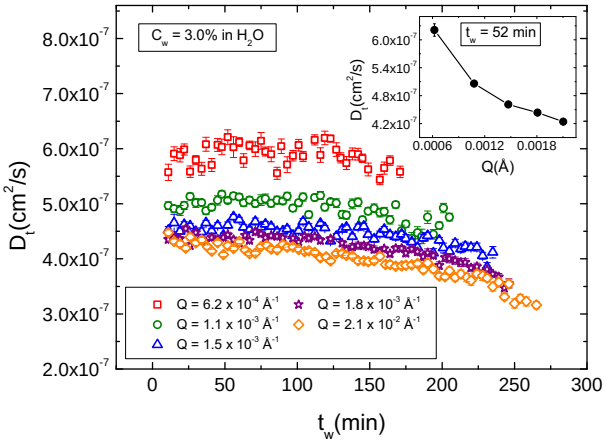

Figure 4.18. Waiting time dependence of the translational diffusion coefficient for the sample with $C_w = 3.0\%$ in H_2O at five scattering wave numbers. The inset shows the observed Q-dependence of D_t for $t_w = 52$ min.

of freedom decreases linearly with waiting time for all Q-values. This decreasing dependence is explained by the fact that the mobility of the particles during aging is continuously reduced due to the "cages" formed by nearest neighbors. The figure also shows the existence of a Q-dependence of D_t, as evidenced in the inset at an early stage ($t_w = 52$ min).

The aspect ratio of a particle describes the proportional relationship between its width and height. By using the mean height ($\langle t \rangle \sim 1$ nm) and diameter ($\langle d \rangle \sim 25$ nm) of Laponite discs, the mean aspect ratio ($p = \langle t \rangle / \langle d \rangle = 0.04$) of platelets is so small that the ultrathin disc limit ($t \to 0$) can be applied as a reasonable approximation. In this limit, the orientationally averaged single-disc translational (D_t^0) and rotational (D_r^0) diffusion coefficients can be written as

$$D_t^0 = \frac{D_t^{0,\parallel} + 2D_t^{0,\perp}}{3} = \frac{k_B T}{12\eta \langle R \rangle} \tag{4.11}$$

$$D_r^0 = \frac{3k_B T}{32\eta \langle R \rangle^3}, \tag{4.12}$$

where η is the solvent viscosity and $\langle R \rangle$ is the mean radius of the disc. Considering the mean radius of Laponite and the viscosity of the solvents H_2O and D_2O at room temperature, Eqs. (4.11) and (4.12) give $D_t^{0,H_2O} = 3.0 \times 10^{-7}\ cm^2/s$, $D_r^{0,H_2O} = 2.2 \times 10^5\ s^{-1}$, $D_t^{0,D_2O} = 2.4 \times 10^{-7}\ cm^2/s$ and $D_r^{0,D_2O} = 1.7 \times 10^5\ s^{-1}$. Here D_t^0 and D_r^0 correspond to the theoretical translational and rotational diffusion coefficients of a single Laponite disc in a solvent, H_2O or D_2O, as indicated in the superscripts. Although the experimental values of D_t shown in Fig. 4.19 have the same order of magnitude of D_t^{0,H_2O}, differences are expected due to the many particles interactions present in Laponite suspensions. In addition, the experimental translational coefficient D_t presented in Fig. 4.19 might be slightly affected for

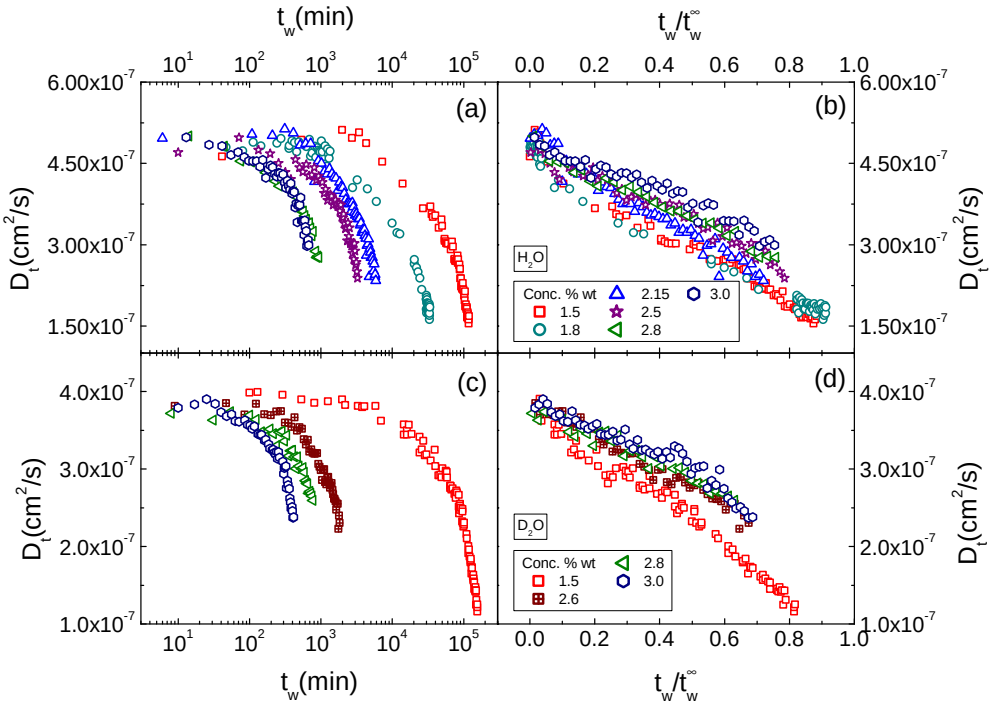

Figure 4.19. Aging evolution of the translational diffusion coefficient for different concentrated samples in (a) H_2O and (c) D_2O at $Q = 1.8 \times 10^{-3}$ Å^{-1}. Right panels show the same values of D_t, reported in left panels, in function of the scaled waiting time (t_w/t_w^{∞}).

longer waiting times, as already mentioned previously, due to the fact that the single exponential decay, that describes τ_1, starts to get contributions from the increasing of the slow relaxation time τ_2 (see Fig. 4.1) that renders the use of Stokes Einstein rigorously valid only for $t_w = 0$.

The aging dependence of D_t from samples with different clay concentrations in H_2O and D_2O is shown in left panels of Fig. 4.19. The values of the translational diffusion coefficient depart from roughly the same value for all concentrated samples ($\sim 5 \times 10^{-7}$ cm^2/s for H_2O and $\sim 4 \times 10^{-7}$ cm^2/s for D_2O) and decay linearly with different rates to a lower value. To better visualize this decay dependence, we reported in right panels of Fig. 4.19 the translational diffusion coefficients in function of the scaled waiting time (t_w/t_w^{∞}). Differently from the parameters associated with slow dynamics, *i.e.* τ_m and β, D_t does not scale in two distinct curves. It indicates that the two decays shown in Fig. 4.3 are really describing two different relaxation processes and the expression (4.3) well represents the system.

The difference between the theoretical values $D_t^{0,H_2O} = 3.0 \times 10^{-7}$ cm^2/s and $D_t^{0,D_2O} = 2.4 \times 10^{-7}$ cm^2/s, obtained through Eq. 4.11, is due to the fact that the viscosity of D_2O, at a fixed temperature, is significantly larger than that of H_2O. In fact, as expected, Fig. 4.19 shows that the experimental values of D_t in D_2O

is lower than in H_2O during the whole aging. Besides, it is clear from Fig. 4.19 (left panels) that the decay rate is lower in D_2O compared to H_2O, which is also related to the fact that D_2O has a higher dynamic viscosity. The lower values of translational diffusion coefficient of Laponite particles in D_2O compared to H_2O explain the slower aging velocity, observed in Fig. 4.7, for this solvent.

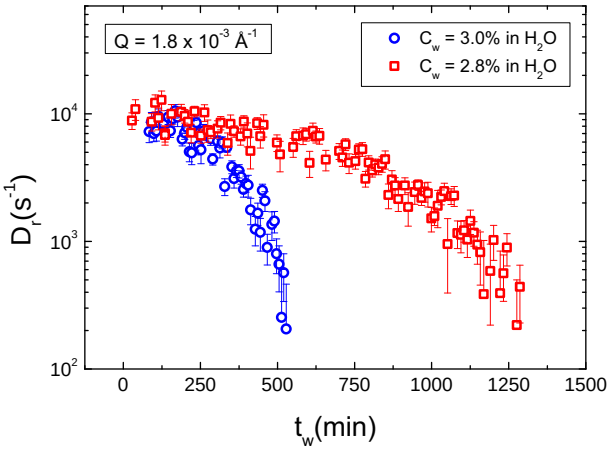

Figure 4.20. Waiting time evolution of the rotational diffusion coefficient for the two samples with $C_w = 3.0\%$ and $C_w = 2.8\%$ in H_2O at $Q = 1.8 \times 10^{-3}$ Å^{-1}.

Finally in Fig. 4.20 the waiting time dependence of the rotational diffusion coefficient obtained for two samples with $C_w = 3.0\%$ and $C_w = 2.8\%$ in H_2O at $Q = 1.8 \times 10^{-3}$ Å^{-1} is presented. To extract the contribution of D_t from g_2^{VH} we used the measurements on the same sample in VV and VH configurations at 90°, as described previously. Therefore, both polarized (g_2^{VV}) and depolarized (g_2^{VH}) time correlation functions were measured at the same scattering wave number ($Q = 1.8 \times 10^{-3}$ Å^{-1}) for time periods equally spaced. Both g_2^{VV} and g_2^{VH} were fitted using the same double exponential expression (Eq. (4.3)), and values of τ_1^{VV} and τ_1^{VH} were used to calculate the rotational diffusion coefficient through expression (4.12). We found that the values of D_r depart from $\sim 10^4$ s^{-1} and decay linearly with t_w up to $\sim 2 \times 10^2$ s^{-1} following different rates for both samples (see Fig. 4.20). Another important aspect to be noticed from the rotational diffusion coefficient is that the theoretical value $D_r^{0,H_2O} = 2.2 \times 10^5$ s^{-1}, estimated previously for a single disc, differs one order of magnitude from D_r at early waiting times $\sim 10^4$ s^{-1}. This probably arises from both hydrodynamic and eletrostatic interactions which restrict the rotational motion of the particles [92, 93].

4.2 X-ray Photon Correlation Spectroscopy Results

In this work we have used a five channels DLS setup as main technique to investigate the dynamic properties of Laponite system under aging at different Q-vectors accessible with visible light. The intensity correlation functions obtained through

this technique permit in fact to study the aging of the system at short Q-values, determined by $Q = 4\pi n/\lambda \sin(\theta/2)$, where λ is the laser wavelength (in our case $\lambda =$ 642 nm) and therefore $6.2 \times 10^{-4} < Q < 2.1 \times 10^{-3}$ Å^{-1}. Moreover the DLS setup permits to access the time window of $(10-10^6$ μs) in the ergodic regime *i.e.* where the ensemble- and time-average identity holds. When the non-ergodic regime is reached the intensity fluctuations start to become uncorrelated and conventional DLS no longer probes the system correctly since the sample data must be ensemble-averaged. At this point the X-ray Photon Correlation Spectroscopy (XPCS) technique plays a fundamental role due to the ensemble average measurements performed over a sequence of speckle patterns obtained by a 2D detector (see chapter 3). In addition, XPCS technique has also the advantage to enlarge the accessible time window to a DLS complementary range ($10^{-1} - 10^5$ s) at higher scattering vectors ($3.1 \times 10^{-3} < Q < 2.2 \times 10^{-2}$ Å^{-1}). Due to these advantages XPCS technique has emerged as an important tool to investigate the dynamical changes of nanometric colloidal systems under aging and gelation [94].

The time-resolved multi-speckle X-ray scattering experiments were performed at the Troika beamline ID10 of the European Synchrotron Radiation Facility (ESRF, Grenoble, France). For each measurement thousands of frames were recorded and subsequently analyzed. During several runs the consistency of the results was verified by checking and comparing the static structure factor profile, in order to ensure that samples were not suffering beam damage.

Figure 4.21 shows the aging evolution of the normalized ensemble-averaged time correlation function for three samples with $C_w = 3.0\%$ in H_2O (a) and D_2O (b) and $C_w = 4.0\%$ in D_2O (c) at $Q = 1.0 \times 10^{-2}$ Å^{-1}. As amply discussed, with aging, the sample slows down and the slow relaxation time (τ_2) increases with t_w up to reach a certain value that cannot be probed anymore at short delay times ($t < 1$ s, see Fig. 4.1). This time approximately corresponds to the ergodicity breaking that cannot be investigated by conventional time averaged DLS. During the non-ergodic regime τ_2 enters in the time window covered by the XPCS setup ($t > 0.05$ s, see Fig. 4.21) that correctly performs ensemble average. The black curves shown in Fig. 4.21, placed at constant $g_2(Q,t) - 1 \approx 0$, represent the time correlation functions for "young" samples ($t_w < 743$ min for (b) and $t_w < 480$ min for (c)) that have dynamics covering time scales $t < 0.05$ s which is faster than the accessible time window of XPCS. One clear example is that of the sample with $C_w = 3.0\%$ in D_2O: while Fig. 4.1 (c) shows the aging evolution during the ergodic regime (faster dynamics), with waiting times in the range of $0 < t_w \leq 679$ min, the correlation functions start to appear in Fig. 4.21 (b) only for $t_w \geq 743$ min (slower dynamics).

All the correlation functions obtained through XPCS at several scattering vectors (Q) and waiting times (t_w) were fitted by the Kohlrausch-Williams-Watts (KWW) modified exponential form:

$$g_2(\mathbf{Q},t) - 1 = b\left[\exp\left(-\left(\frac{t}{\tau_2}\right)^{\beta}\right)\right]^2. \tag{4.13}$$

This expression corresponds to the second exponential decay of Eq. (4.3), where b is the optical contrast, τ_2 the slow relaxation time associated with the structural rearrangement of the system and β is a measure of the distribution width of the slow

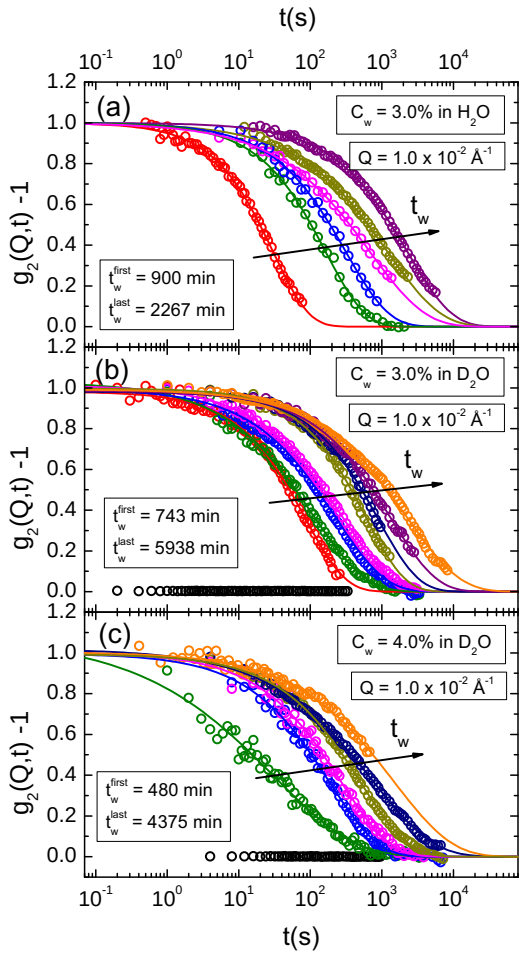

Figure 4.21. Aging evolution of the normalized ensemble-averaged time correlation function for three samples with $C_w = 3.0\%$ in (a) H_2O and (b) D_2O and (c) $C_w = 4.0\%$ in D_2O at $Q = 1.0 \times 10^{-2}$ Å^{-1}. Full lines correspond to the fitting obtained through Eq. (4.13).

relaxation time. Full lines shown in Fig. 4.21 represent the fitting curves obtained through Eq. (4.13). The obtained parameters (τ_2 and β) in function of t_w, for the samples with $C_w = 3.0\%$ in H_2O and D_2O and $C_w = 4.0\%$ in D_2O at $Q = 1.0 \times 10^{-2}$ Å^{-1}, are shown in Fig. 4.22.

Unlike the waiting time behavior found for τ_2 and β during the ergodic regime, shown in Fig. 4.5 (exponential growth and linear decay for τ_2 and β respectively), we found that in the XPCS regime τ_2 increases linearly and β remains roughly constant with t_w (Fig. 4.22). Figure 4.22 (a) and (c) shows that for the two solvents at $C_w = 3.0\%$ τ_2 increases following roughly the same rate and β remains practically unchanged. Hence, it becomes clear that the different aging velocity found during the ergodic regime by means of DLS (Fig. 4.7) cannot be observed during the non-ergodic regime probed by XPCS. However, by keeping the same solvent (D_2O) and changing only the clay concentration, τ_2 presents higher values for higher concentrated samples at the same waiting time and also mantains the stretching parameter β unchanged

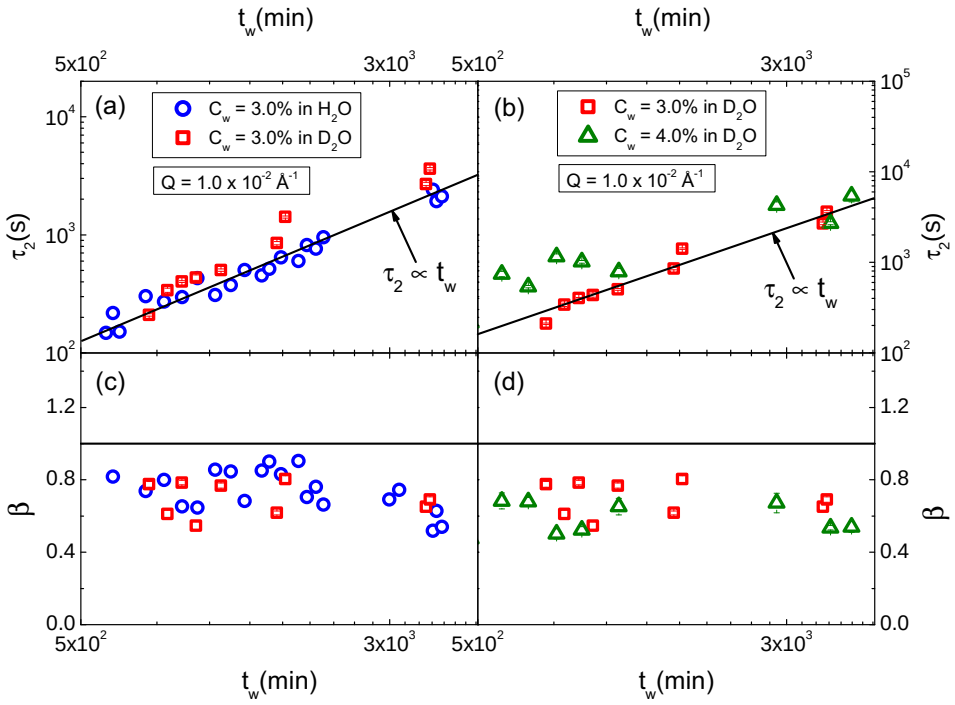

Figure 4.22. Comparison of the slow relaxation time (τ_2) and β parameter dependence on t_w between samples with $C_w = 3.0\%$ in both solvents H_2O and D_2O (left panels) and samples with different clay concentrations $C_w = 3.0\%$ and $C_w = 4.0\%$ in D_2O (right panels).

with t_w (see Figs. 4.22 (b) and (d)).

The linear behavior observed in Figs. 4.22 (a) and (b) for the structure relaxation time with t_w is in agreement with previous studies of the aging of Laponite suspensions [95, 90, 96, 97] that distinguish two distinct regimes. Tanaka *et al.* found a correspondence between the crossover from the cage-forming to the full aging regime and the ergodic to non-ergodic transition [95]. Therefore the full aging regime is not accessible by conventional DLS only because it occurs for long waiting times, when the system has a slow relaxation time out of the available time window ($t_{MAX}^{DLS} = 1$ s), but also because ensemble average measurements are necessary. The early stage of aging is characterized by a cage-forming process where τ_2 increases exponentially with t_w ($\tau_2 \propto \exp(t_w)$) until τ_2 becomes comparable to t_w, although never exceeding it. Subsequently the system enters into the late stage, called full-aging regime, where τ_2 evolves linearly with t_w ($\tau_2 \propto t_w$). The full lines showed in the upper panels of Fig. 4.22 depict the linear dependence of the slow relaxation time with waiting time during the full aging regime.

To explain this two-stage aging kinetics Tanaka and coworkers considered a simple model, based on experimental observations, for the relation between the viscosity and the structure relaxation time (τ_2) [95]. They expressed this aging

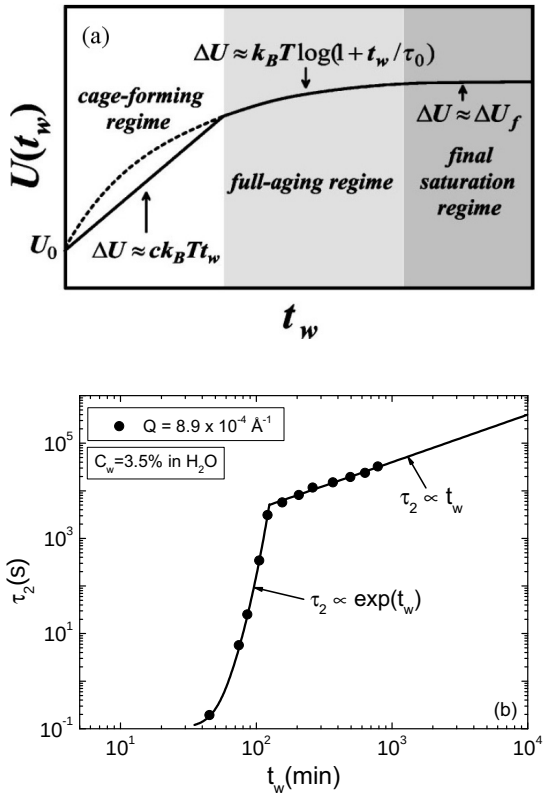

Figure 4.23. (a) Schematic figure representing the waiting time dependence of the effective barrier height $U(t_w)$ proposed by Tanaka *et al.* [95]. (b) Waiting time dependence of the structure relaxation time τ_2 reproduced from [96] for a sample with $C_w = 3.5\%$ in H_2O at $Q = 8.9 \times 10^{-4}$ Å^{-1}.

process in terms of the average barrier height U for particle motion, where τ_2 is often described as

$$\tau_2 = \tau_0 \exp\left(\frac{U}{k_B T}\right), \tag{4.14}$$

where τ_0 is the inverse of a typical attempt frequency. During aging, U is a function of waiting time and is expressed by $U(t_w) = U_0 + \Delta U(t_w)$, where U_0 is U at $t_w = 0$. The light scattering data indicated that during the ergodic regime (early times), $\Delta U(t_w)$ grows linearly with t_w as

$$U(t_w) = U_0 + c k_B T t_w. \tag{4.15}$$

After the ergodicity breaking of the system, *i.e.* waiting times longer than t_w^∞, the experiments indicate that $\Delta U(t_w)$ grows logarithmically with t_w as

$$U(t_w) = U_0 + k_B T \ln\left(1 + \frac{t_w}{\tau_0}\right). \tag{4.16}$$

Subsequently, at very late times, $\Delta U(t_w)$ may become constant and approach ΔU_f. The waiting time dependence of the effective barrier height $U(t_w)$ proposed

by Tanaka *et al.* is schematically shown in Fig. 4.23 (a).

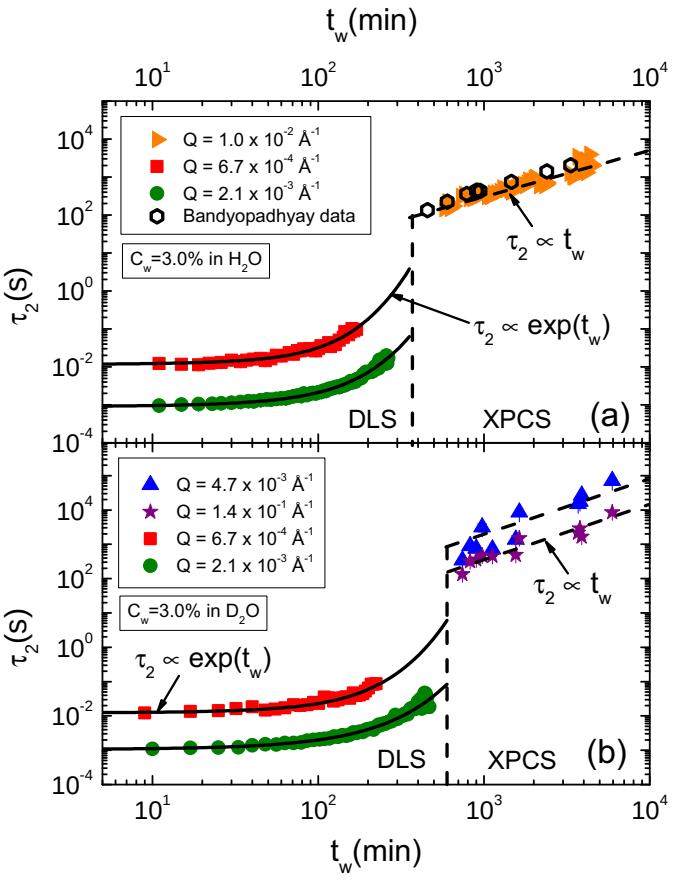

Figure 4.24. Joined results of τ_2 as a function of t_w obtained from DLS and XPCS, for the samples with $C_w = 3.0\%$ in H_2O (a) and D_2O (b) at different Q-values displayed in the legend, showing the characteristic picture of the two ergodic and non-ergodic regimes. Hexagon symbols in (a) represents the data by Bandyopadhyay *et al.* obtained through XPCS for a sample with $C_w = 3.0\%$ in H_2O at $Q = 1.4 \times 10^{-2}$ Å^{-1} [97].

This barrier high may be related to the size of the domains into the system according to the "droplet picture of spin glasses" that works properly during the non-ergodic regime [86, 95]. The linear growth of ΔU with t_w means a power-law increase of the domain size, while its logarithm growth indicates the slow logarithmically increase of the domain size with t_w.

Figure 4.24 shows the values of the structural relaxation time (τ_2) as a function of waiting time, for the sample with $C_w = 3.0\%$ in both H_2O and D_2O, obtained by DLS and XPCS techniques. Vertical dashed lines in Fig. 4.24 are placed exactly at the divergence waiting times ($t_w^{\infty} = 340$ and 600 min for $C_w = 3.0\%$ in H_2O and D_2O respectively), obtained through Fig. 4.7, and represent the ergodic to non-ergodic transition that separates DLS data (on the left side) from XPCS data (on the right side). This figure shows that DLS and XPCS are probing different aging behaviors of τ_2. In fact, as expected from Fig. 4.23 (a), the ergodicity breaking

determines that the dynamic properties of the system follow two distinct waiting time dependencies. As previous described, Fig. 4.24 perfectly depicts this transition where full lines represent the typical exponential growth of τ_2 observed by DLS during the ergodic regime (cage-forming process) and dashed lines describe the linear growth of τ_2 observed by XPCS after the ergodicity breaking of the system (full aging regime).

Figure 4.23 (b) shows the results by Bellour *et al.* reproduced from [96] for a sample with $C_w = 3.5\%$ measured by multispeckle DLS setup at $Q = 8.9 \times 10^{-4}$ Å^{-1}. By performing ensemble average Bellour and co-workers were able to follow the aging of the sample during very long waiting times and access the distinct trends that represent the two regimes described previously. Even obtaining separated time and ensemble averaged results by two different techniques at different times, our results are in good agreement with that of Bellour and co-authors. Besides, Fig. 4.24 (a) shows that our XPCS data are in perfect agreement with results obtained by Bandyopadhyay *et al.* through XPCS for a sample with $C_w = 3.0\%$ in H_2O at $Q = 1.4 \times 10^{-2}$ Å^{-1} [97].

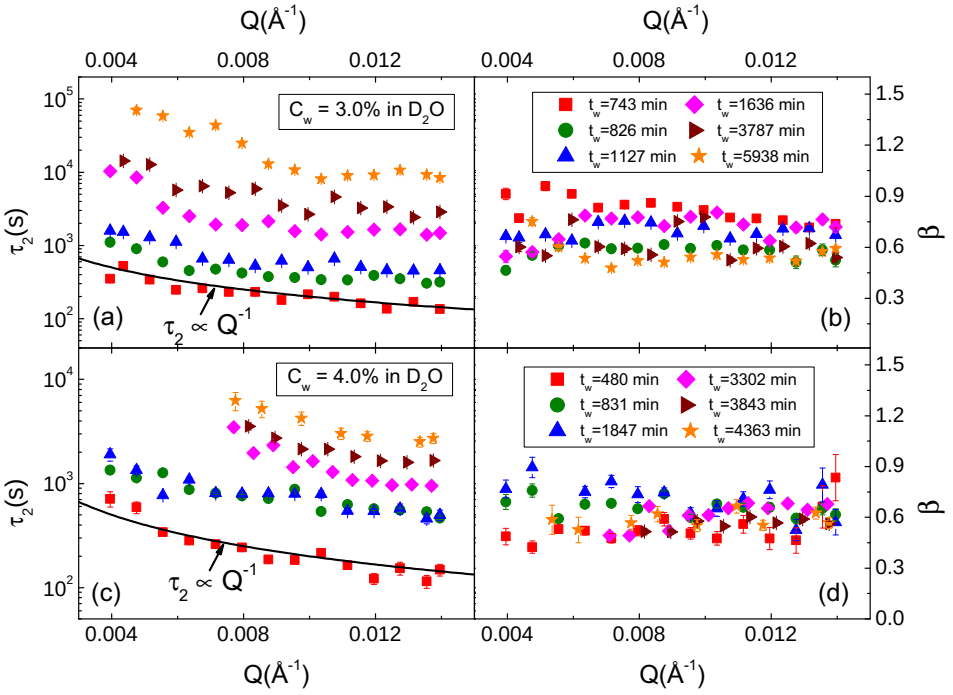

Figure 4.25. Q-dependence of the slow relaxation time τ_2 and β parameters obtained through Eq. (4.13) for the samples with $C_w = 3.0\%$ (upper panels) and $C_w = 4.0\%$ (lower panels) in D_2O at different waiting times displayed in the legends.

The ensemble average performed in the time-resolved multi-speckle X-ray scattering permits the acquisition of time correlation function at several scattering vectors. Figure 4.25 shows the Q-dependence of the τ_2 and β obtained through Eq. (4.13) at different waiting times, displayed in the legends, for samples with $C_w = 3.0\%$ (upper

panels) and $C_w = 4.0\%$ (lower panels) in D_2O. From this figure it is clear that the stretching parameter β obtained during the non-ergodic regime do not present any Q-dependence, exactly like in the ergodic regime. This Q-independence remained the same during all measured waiting times. On the other hand, in agreement to the results reported by Schosselet *et al.* and Pujala *et al.* [90, 91], the slow relaxation time τ_2 presents a Q^{-1} dependence and no longer represents the diffusive motion of the particles. This $\tau_2 \propto Q^{-1}$ behavior, evidenced by the full lines in Fig. 4.25 (left panels) for the lowest t_w, maintained the same dependence during all the experiment. At low Q-values a scale different from $\propto Q^{-1}$ may emerge due to the effects of a possible stray scattering produced by the aperture. Therefore from the DLS and XPCS data one can deduce that the Q-dependence of the relaxation times ($\tau_2 \propto Q^{-2}$ and $\tau_2 \propto Q^{-1}$ for DLS and XPCS respectively) depict the Brownian motion nature of Laponite discs during the ergodic regime and the reduced mobility of the particles when the non-ergodic regime is reached.

During XPCS measurements we prepared a set of five samples with different clay concentrations with $C_w = 1.5$, 2.5, 3.0 and 4.0% in D_2O and 3.0% in H_2O. However, the dynamics of the samples with $C_w = 1.5$ and 2.5% remained too fast ($t < 1$ s), during the whole available beamtime, to be probed with this XPCS setup. Therefore the dynamic properties of the samples with slow waiting time evolution (gel) could not be investigated by XPCS.

4.3 Neutron Spin Echo Results

In this work we also performed Neutron Spin Echo (NSE) experiments to extend the investigation of Laponite dynamics in a delay time and scattering vector range not accessible by DLS and XPCS. NSE spectroscopy is a quasielastic neutron scattering technique that determines the time-space correlation function on time-scales from subnanosecond to submicrosencond and length-scales from several angstroms to several hundred angstroms [79]. Thus, by using NSE it is possible to look at the dynamics of Laponite system on a more local range *i.e.* larger Q-values and shorter times.

NSE measurements were performed at the spectrometer IN15 of the Institute Laue-Langevin (ILL, Grenoble, France) using wavelengths of 22.5, 16 and 8 Å with corresponding scattering vectors of 0.02, 0.06 and 0.11 Å^{-1} respectively [98]. It gives a time range of $I(Q,t)$ that covers the region suitable for the fast dynamics of Laponite system ($3.7 \times 10^{-9} \leq t \leq 537 \times 10^{-9}$ s). Therefore, by joining DLS, XPCS and NSE a large time and Q ranges can be covered to give more insight on the role of H/D isotopic substitutions on the aging process present in Laponite dispersions. The scattering vector ranges covered by these three techniques are: from 6.7×10^{-4} to 2.1×10^{-3} Å^{-1} by DLS, from 3.1×10^{-3} to 2.2×10^{-2} Å^{-1} by XPCS and from 1.3×10^{-2} to 1.3×10^{-1} Å^{-1} by NSE. On the other hand the delay time scales are: from 3.7×10^{-9} to 5.4×10^{-7} s by NSE, from 5×10^{-6} to 1 s by DLS and for $t > 1$ s by XPCS.

In order to gain contrast with the neutron scattering technique, we used D_2O with 99.9% purity supplied by Euriso-Top. The background was measured on a D_2O buffer and sample spectra were corrected using the relative transmissions

following the standard procedures found elsewere in literature [99, 100, 101]. The intermediate scattering function $f(Q,t)$ was measured on five samples, with different clay concentrations, in order to cover both gel ($C_w < 2\%$) and Wigner glass ($C_w \geq 2\%$) arrested states of the system. In particular, since the gelation of Laponite, that takes place in a low clay concentrations, evolves very slowly (on time scales of weeks/months), the NSE beamtime was splitted into three different dates in order to follow the complete waiting time evolution from sol to gel/glass.

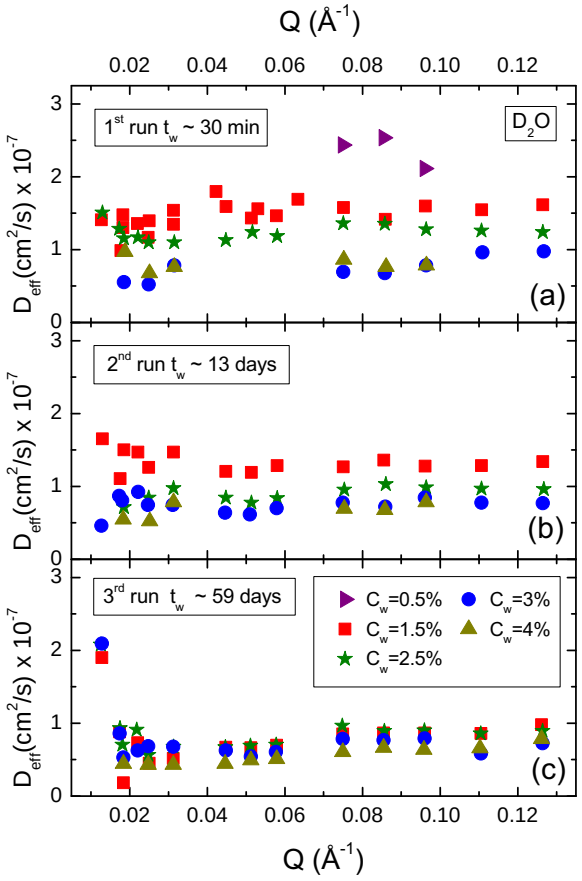

Figure 4.26. Effective diffusion coefficient as a function of scattering vectors Q obtained through NSE technique for the samples with $C_w = 0.5$, 1.5, 2.5, 3.0 and 4.0% in D_2O at three different waiting times: (a) $\sim$ 30 min, (b) $\sim$ 13 days and (c) $\sim$ 59 days.

The acquired dynamic structure factors ($f(Q,t)$) contain a superposition of exponential relaxations associated with the areas grouped together on the 2D detector. They can be fitted by the following expression

$$f(Q,t) = \exp\left(-\left(\frac{t}{\tau}\right)^{\beta}\right), \tag{4.17}$$

where the stretching parameter β represents the deviation of Eq. (4.17) from a single exponential decay [99]. For all measured dynamic structure factors the β

parameter was found to be always ~ 1. The effective diffusion coefficients (D_{eff}) were calculated using the expression $D_{eff} = 1/(\tau \cdot Q^2)$ and studied as a function of the scattering vector (Q) and waiting time (t_w).

Figure 4.26 shows the Q-dependence of D_{eff} for all the samples measured by NSE at three different waiting times acquired during our beam time at ILL. The first measurements were acquired about 30 minutes after each sample preparation, *i.e.* at the beginning of the aging phenomenon (Fig. 4.26 (a)). This figure reveals that the diffusion coefficients have no Q-dependence and that high concentrated samples have lower D_{eff}. The clay concentration dependence of D_{eff} at early stages is presumably caused by the lower mobility of high concentrated samples respect to low concentrated ones. The second run of experiments was measured after 13 days and is shown in Fig. 4.26 (b). According to the divergence waiting time (t_w^{∞}) data obtained through DLS, shown in Fig. 4.7, after 13 days only the samples with clay concentration higher than 2.0% in D_2O should be already in an arrested state. At this waiting time D_{eff} decreased for all the samples in agreement with the fact that with aging the relaxation times are slowed down. Moreover only the $C_w = 1.5\%$ sample has D_{eff} significantly higher respect to the others due to the fact that this sample is the only one supposed to be in an ergodic phase. Subsequently, for waiting times of about 59 days, Fig. 4.26 (c) shows that the effective diffusion coefficients decreased even more for all the concentrated samples, reaching a much slower dynamics. It seems that the effective diffusion coefficients are converging to the same final value ($D_{eff} \sim 0.5 \times 10^{-7}$ cm/s) for all the samples.

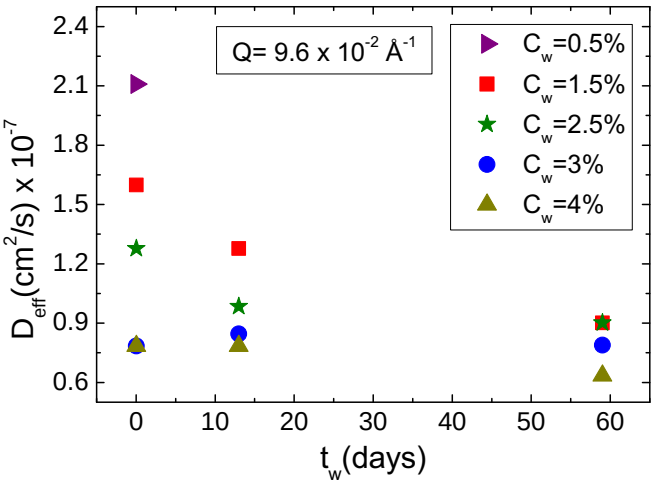

Figure 4.27. Aging evolution of the effective diffusion coefficient obtained through NSE technique for the samples with $C_w = 0.5$, 1.5, 2.5, 3.0 and 4.0% in D_2O at $Q = 9.6 \times 10^{-2}$ Å^{-1}.

The waiting time dependence of D_{eff} is more evident in Fig. 4.27 where D_{eff} as a function of t_w for all the samples at $Q = 9.6 \times 10^{-2}$ Å^{-1} is reported. This figure clearly shows that the decay rate of D_{eff} with t_w is higher for low concentrated

samples. D_{eff} remained almost unchanged for the two samples with $C_w = 3.0\%$ and 4.0% in D_2O as they were probably arrested or very close to arrest. On the contrary the effective diffusion coefficient decreases with waiting time at lower concentrations up to reach the arrested state at a value comparable with the highest concentrated samples (3.0% and 4.0%).

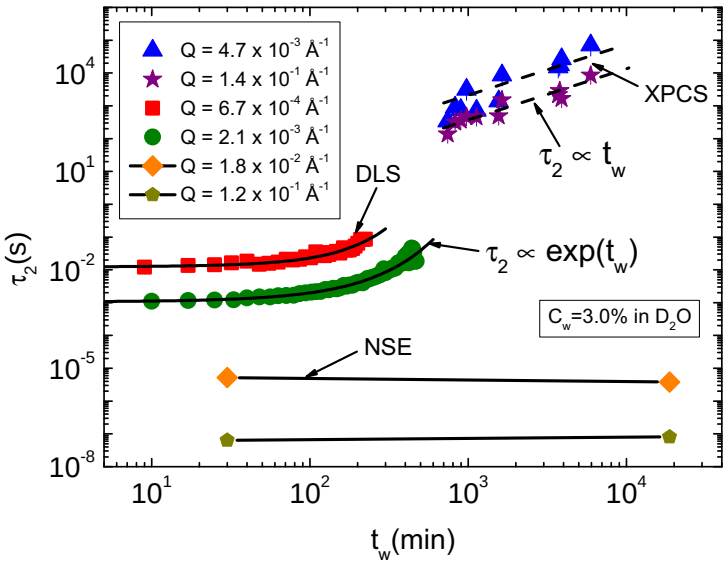

Figure 4.28. Joined results of τ_2 as a function of t_w obtained through DLS, XPCS and NSE, for the sample with $C_w = 3.0\%$ in D_2O at different Q-values displayed in the legend.

Figure 4.28 shows the structural relaxation time as a function of t_w obtained through DLS, XPCS and NSE. By comparing the values of τ obtained by these techniques, it becomes clear that NSE is probing a much faster dynamics compared to the slow relaxation time obtained from DLS and XPCS and shows no evidences of a big change with waiting time as observed for τ_2.

Therefore the mean relaxation time obtained from NSE is related to the fast diffusive motion of particles in the sample like τ_1 probed by DLS. To understand this relation the fast relaxation times obtained from NSE and DLS are shown in Fig. 4.29 as a function of scattering vector for the samples with $C_w = 1.5\%$ (upper panels) and $C_w = 3.0\%$ (lower panels) in D_2O at initial (left panels) and long (right panels) waiting times. This figure shows that the fast relaxation time obtained by DLS and the time probed by NSE scale as $\tau \propto Q^{-2}$. Actually, DLS measurements showed that τ_1 scale as $\propto Q^{-1.7}$, and the relaxation time obtained through NSE scales perfectly with $\propto Q^{-2}$. As discussed previously, this characteristic Q-dependence reflects the diffusive nature of the fast motion. Even when the non-ergodic regime is reached and the mobility of the particles is dramatically reduced by the constraining of neighboring "cages", so that the slow relaxation time τ_2 changes its Q dependence from Q^{-2} to a Q^{-1} behavior (see previous section), the fast relaxation time τ_1

remains $\propto Q^{-2}$, evidence of a still diffusive motion. This can be evidenced from Fig. 4.29 (d) where this Q^{-2} behavior is evident for a sample with $C_w = 3.0\%$ at $t_w = 59$ days that is surely arrested (see Fig. 4.7).

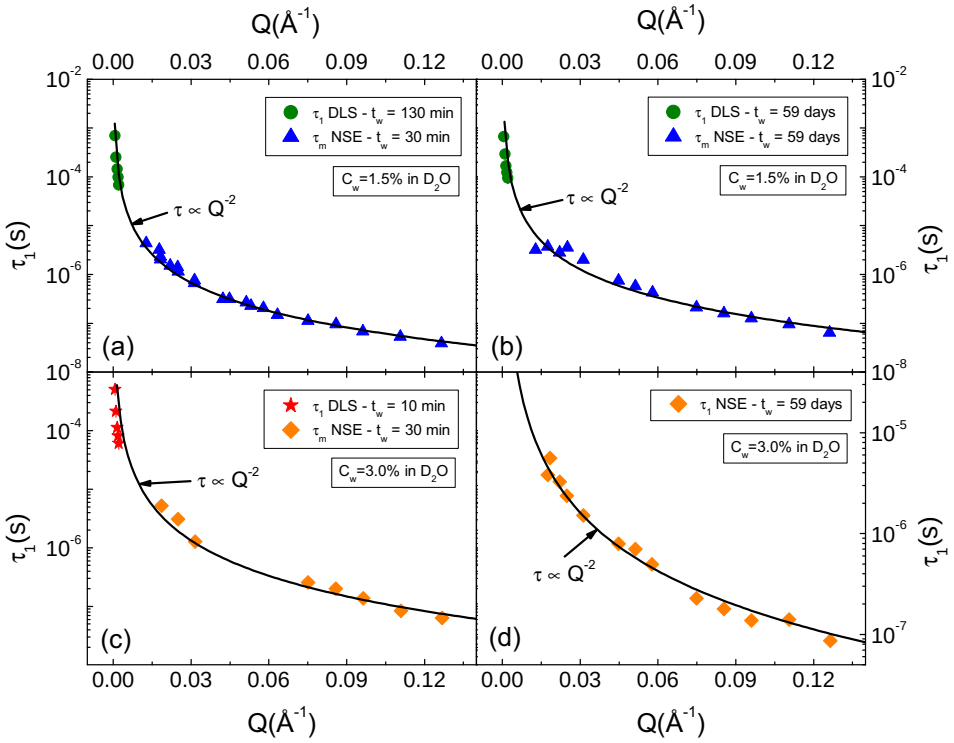

Figure 4.29. Q-dependence of the fast and mean relaxation times obtained respectively by DLS and NSE techniques for the samples with $C_w = 1.5\%$ (upper panels) and $C_w = 3.0\%$ (lower panels) in D_2O at initial (left panels) and long (right panels) waiting times. Full lines represent the Q^{-2} dependence of τ in the ergodic (a), (b) and (c) and non-ergodic regime (d).

4.4 Small Angle X-ray Scattering Results

As discussed in chapter 2, due to the anisotropic shape and competitive interactions present in Laponite discs, the suspension of particles age spontaneously with time up to form arrested states that characterize a complex phase diagram. In the past ten years this system has attracted the attention of many scientists, being studied by many different experimental techniques with the support of theory and simulations [14]. Until now most of these studies have been performed in aqueous solvent by changing the ionic strength of the solution and clay concentration. In order to comprehend the effects of H/D isotopic substitutions in the solvent on the dynamical properties of the system during aging we presented in the previous sections a systematic experimental study in Laponite dispersed in both H_2O and

D_2O solvents for several concentrations $1.5 \leq C_w \leq 3.5\%$ by means of three different dynamic scattering techniques that covers a wide range of scattering vector and time window. The results showed evidences that the aging velocity of the system is significantly affected by changing the solvents in the ergodic regime but that no further significative differences are found in the two solvents. Moreover DLS measurements have shown the existence of two different arresting mechanisms for low and high concentrated samples as already found in water suspensions [54, 14]. Thus the arresting mechanism during aging occurs similarly for both solvents. These results induce to speculate that also in the case of D_2O two different arrested states, of gel and glass respectively for low and high concentrations, can be found. In order to check this point, the static properties of Laponite system have been studied by means of Small Angle X-ray Scattering (SAXS) technique on low and high concentrations, expected in the gel and glass state, in both H_2O and D_2O solvents at increasing waiting times. SAXS measurements were performed at the high brilliance beam line ID2 at the European Synchrotron Radiation Facility (ESRF, Grenoble, France). This techquine permitted to explore an exchanged momentum range of $9.1 \times 10^{-3} < Q < 0.6$ nm^{-1} that corresponds to lengh scales of $10 - 690$ nm, ideal for Laponite systems. Although XPCS technique permits to follow both dynamics and static informations, a much better statistics is obtained through SAXS measurements.

For the measurements the scattering speckle patterns, similar to that shown in Fig. 3.11 (a), were recorded by a two-dimensional image-intensified Charged-Couple Device (CCD). In order to correctly measure the absolute scattering intensity as a function of Q the experimental data recorded by the CCD have been subtracted by both dark image and scattering intensity originated by the background, *i.e.* capillary and solvent. To obtain useful information regarding the structural rearrangement of the particles within the sample, the static structure factor $S(Q)$ is calculated by inverting Eq. 3.87 showed in chapter 3. From this expression it is clear that the structure factor is related to the absolute scattered intensity $I_s(Q)$ and the form factor $P(Q)$ that takes into account the contribution of the absolute scattering due to the shape of single particles. Therefore, to calculate the static structure factor it is necessary to obtain also the form factor $P(Q)$, that in our case is connected to the discoidal shape of Laponite particles.

4.4.1 Form Factor of a Thin Disc

To evaluate the form factor contribution a dilute isotropic suspension of N monodisperse discs per volume V is considered. The scattering intensity $I_s(Q)$ can be expressed by the product of the intensity of single particles $I_0(Q)$ and structure factor $S(Q)$ [102, 103, 104]. On the other hand, the scattering intensity of a single disc can be used to define the form factor through

$$I_0(Q) = V_p^2 \left(\bar{\rho} - \rho_m\right)^2 P(Q), \tag{4.18}$$

where V_p denotes the volume of the particles, $\bar{\rho}$ is the scattering length density of the particles, ρ_m is the respective quantity of the solvent and $P(Q)$ is normalized to unity at $Q = 0$. To obtain the form factor of Laponite suspension very diluted samples have been measured by SAXS, in order to suppress the interparticle interactions

and measure only the signal due to characteristic particle shape. Theoretically, the scattered field $F(Q, H, R, \theta)$ related to a thin disc is given by [102, 103, 104]:

$$F(Q, H, R, \theta) = \frac{\sin(QH\cos\theta)}{QH\cos\theta}\frac{2J_1(QR\sin\theta)}{QR\sin\theta}, \tag{4.19}$$

where θ is the angle between the normal to the disc plane and Q, $2R$ is the disc diameter, $2H$ is the thickness of the disc and J_1 is the first order Bessel function. To calculate the form factor all the possible angles θ should be averaged in such a way that

$$P(Q, H, R) = \int_0^{\frac{\pi}{2}} |F(Q, H, R)|^2 \, p(\theta) \sin\theta d\theta, \tag{4.20}$$

where $p(\theta)$ is the orientational distribution function that, if the discs are randomly oriented, gives $p(\theta) = 1$. Equation 4.19 shows that in the limit of $H \to 0$ the first factor on the right hand side becomes equal to unity. On the other hand, in the limit of large Q, Eq. 4.20 can be rewritten as an integral over the decaying Bessel function squared, which gives a constant divided by the remaining factor Q^2. In agreement to this theoretical calculation, the experimental $P(Q)$ showed to scale as Q^{-2} in a scattering vector range of $0.2 < Q < 2$ nm^{-1}.

4.4.2 Static Structure Factor

The measured static structure factor $S^M(Q)$ can be obtained inverting Eq. 3.87, *i.e.* dividing the measured scattered intensity $I_s(Q)$ by the experimental form factor $P(Q)$.

Figure 4.30 shows the waiting time evolution of the static structure factors acquired by SAXS for two samples in the low $C_w = 1.5\%$ (a) and high $C_w = 3.0\%$ (b) concentration regions prepared in D_2O solvent. A clear significative difference in $S^M(Q)$ is observed in both samples. At initial waiting times ($t_w < 615$ min for $C_w = 1.5\%$ and $t_w < 564$ min for $C_w = 3.0\%$), both low and high concentrated samples show a characteristic decreasing of intensity at low Q-values (represented by an arrow in Fig. 4.30 (b)). During this early stage the main difference between low and high concentrated samples is a small shift of the main peak. However, for longer waiting times a large difference arrises in the static structure factor of these samples. The $S^M(Q)$ is not changing significatively for high concentrated samples, Fig. 4.30 (b), characterized by a decrease in the intensity at low Q and a small shift of the main peak to higher Q-values (depicted by an arrow in Fig. 4.30 (b)). On the contrary, low concentrated samples show a dramatic change in $S^M(Q)$ at low Q-values as the sample evolves and approaches the non-ergodic regime. In this case a progressively increase of scattering is observed at low Q and a change in the shape of the curve is evidenced with the presence of a significant shift of the main peak towards higher Q-values (depicted by arrows in Fig. 4.30 (a)). These differences are similar to that found in H_2O solvents [68] and represent the clear evidence that the two samples are reaching the final non-ergodic regimes following different routes [54] and, furthermore, that the two final arrested states are actually different.

In order to understand the nature of these two distinct arrested states we recall Fig. 2.13 that shows the characteristic structure factors of gel and glass.

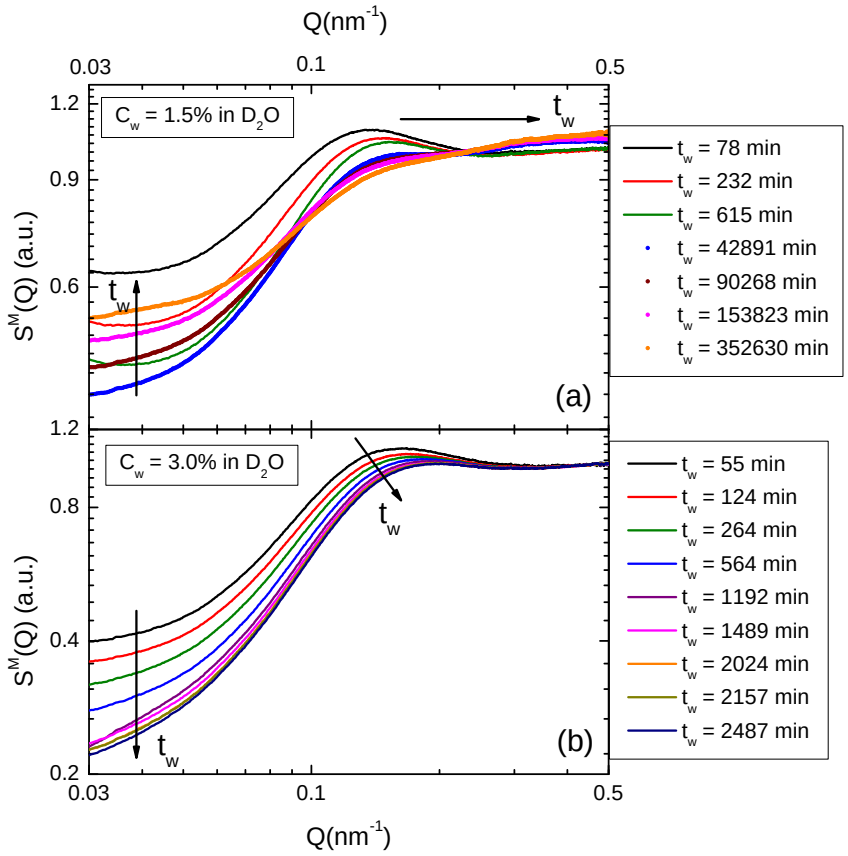

Figure 4.30. Waiting time evolution of the static structure factors for two samples with low $C_w = 1.5\%$ (a) and high $C_w = 3.0\%$ (b) clay concentrations in D_2O acquired by means of SAXS at different waiting times displayed in the legends. The arrows indicate the waiting time increasing direction (see text).

From this figure, it is clear that the static structure factor of a gel is generally described by an excess scattering at low Q, which reflects the correlation of the concentration fluctuations associated with the network structure and consequently indicates the formation of an inhomogeneous state. Therefore Fig. 4.30 (a) indicates the formation of a gel structure, while the homogeneous picture found in $S^M(Q)$ for high concentrated samples (Fig. 4.30 (b)) gives a hint to the formation of a glass. In addition, the position of the main peak, when the non-ergodic state is reached (long waiting times), for the high and low concentrated samples are located at $Q \sim 0.16$ nm^{-1} and $Q \gtrsim 0.4$ nm^{-1} respectively that correspond to length scales of ≈ 40 nm for high and $\lesssim 15$ nm for low clay concentrations. This indicates that the particles are mainly disconnected at high C_w and probably bonded in a T-configuration at lower C_w. In this sense the picture of a gel state at low concentrations and of a glass state at high Laponite concentrations is preserved also in D_2O solutions.

The waiting time behavior shown in Fig. 4.30 depicts the same characteristics reported by Ruzicka *et al.* [68] for Laponite in H_2O solvents. To better visualize the

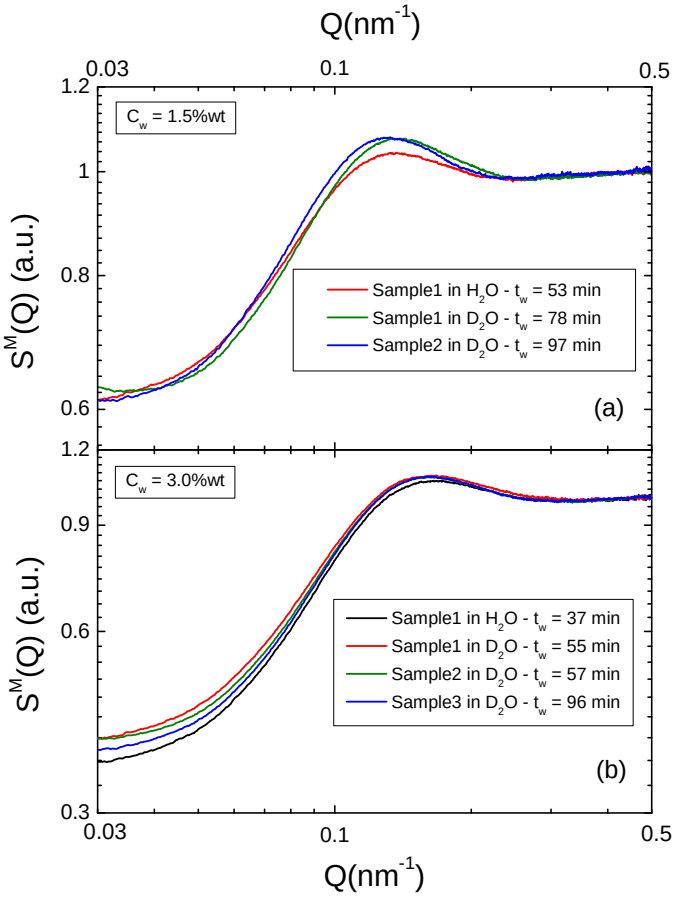

Figure 4.31. Comparison of the static structure factor acquired by SAXS for samples with low (a) $C_w = 1.5\%$ and high (b) $C_w = 3.0\%$ clay concentrations prepared in both H_2O and D_2O solvents at initial waiting times (displayed in the legends). Each curve represents distinct sample prepared at different times.

similarity between Laponite systems prepared in both H_2O and D_2O solvents, the static structure factors of different samples prepared with fixed clay concentrations $C_w = 1.5\%$ and $C_w = 3.0\%$ in H_2O and D_2O have been compared. This comparison is shown in Fig. 4.31 for initial waiting times displayed in the legends where each curve represents distinct samples prepared in both solvents with fixed clay concentrations $C_w = 1.5\%$ (a) and $C_w = 3.0\%$ (b). For both concentrations it is evident that $S^M(Q)$ is not dramatically changed by changing the solvent even if smal changes in the region of the main peak seem to be present especially for low concentrated samples. In addition to the similarity between H_2O and D_2O solvents, Fig. 4.31 also depicts a very good reproducibility of Laponite systems: very similar static structure factors are found for distinct samples with the same clay concentration and solvent.

Basing on all the experimental results observed during this work it is possible to elucidate that H/D isotopic substitution plays an important role only on the aging

velocity during the ergodic regime, preserving the same physical properties and arresting mechanisms present in Laponite in H_2O. Moreover a more comprehensive investigation and the comparison with the static structure factor, obtained with theory and simulations is necessary to verify and understand if and what modifications in the interaction potential are introduced with isotopic substitution.

Chapter 5

Conclusion

In this Thesis a study of dynamic and static properties of a charged colloidal system, Laponite, has been presented. For the first time a complete and systematic investigation of the aging dynamics of this system in a wide scattering vector (*i.e.* in a wide spatial range) and time window has been carried out. In particular the evolution with waiting time of the dynamics and static properties for clay concentrations in the range $C_w = (1.5 \div 3.5)\%$ both in H_2O and D_2O solutions has been followed with the use of conventional Light (DLS), Synchrotron X-ray (XPCS and SAXS) and Neutron (NSE) scattering techniques. This study is therefore also the first systematic investigation of the effect of H/D isotopic substitution on water molecules, fundamental for techniques, such as neutron scattering and nuclear magnetic resonance, that require the use of D_2O to get enough constrast.

A multi angle Dynamic Light Scattering (DLS) setup, that permits the simultaneous measurement of the dynamics at different Q, crucial for systems performing aging, has been built during this thesis. With this setup both polarized and depolarized intensity correlation functions were obtained in a scattering vector range of $6.2 \times 10^{-4} < Q < 2.1 \times 10^{-3}$ Å^{-1} and time window of $10^{-6} \div 1$ s. This technique permitted to investigate the behavior of the translational and rotational degrees of freedom as a function of C_w, t_w and Q during the ergodic regime of the system. To probe the system in a wider Q-range ($3.1 \times 10^{-3} \div 2.2 \times 10^{-2}$ Å^{-1}) and slower delay times ($10^{-1} \div 10^5$ s) X-ray Photon Correlation Spectroscopy (XPCS) technique at the European Synchrotron Radiation Facility (ESRF) in Grenoble was used. The measurements permitted, through the ensemble-averaged time correlation functions, to investigate a different region of the dynamics, not accessible by conventional DLS. To accomplish the dynamic study in a scattering vector range $1.3 \times 10^{-2} < Q < 1.3 \times 10^{-1}$ Å^{-1} and delay time $3.7 \times 10^{-9} \div 5.4 \times 10^{-7}$ s, not accessible by both DLS and XPCS, Neutron Spin Echo (NSE) measurements at the Institute Laue-Langevin (ILL) reactor in Grenoble were performed. Finally a study of the static structure factor ($S(Q)$) for high and low concentrated samples in both D_2O and H_2O solvents has been performed with Small Angle X-ray Scattering (SAXS) technique at ESRF in Grenoble. From the experimental data the following main results, discussed in this work, have been obtained:

- **The Q-dependence of the characteristic parameters for a very large Q and time ranges in a large concentration range ($C_w = (1.5 \div 3.5)\%$**

both in H_2O and D_2O solutions) during all the aging evolution.

- **The fast relaxation time τ_1 (DLS and NSE)**

  From DLS data the fast relaxation time was found to scale as $\tau_1 \propto Q^{-1.7}$. This behavior is very robust, since this dependence remained unchanged in the whole clay concentration and both solvents (H_2O and D_2O) during the whole waiting time related to the ergodic regime. This result makes clear that, during the ergodic regime, particle motion is mainly represented by diffusive processes and is not affected by clay concentration and H/D isotopic substitutions in the solvent.

  NSE results showed that the fast relaxation time scales as $\tau_1 \propto Q^{-2}$.

  The characteristic Q-dependence of τ_1 clarify that the diffusive nature of the fast motions remains unchanged during the whole aging in both ergodic and non-ergodic regimes.

  The fast relaxation time probed by DLS shows an increasing with waiting time. The change is order of magnitude smaller respect to the slow relaxation time but still significative.

- **The slow relaxation time τ_2 (DLS and XPCS)**

  DLS experiments showed that the slow relaxation time was found to scale as $\tau_2 \propto Q^{-2.1}$. Similarly to τ_1 this behavior is very impressive, since it also remained unchanged in the whole clay concentration in both solvents (H_2O and D_2O) during the whole waiting time related to the ergodic regime. Alike τ_1, this dependence of the slow relaxation time during the ergodic regime depicts the diffusive nature of the particles motion that is unaffected by clay concentration and H/D isotopic substitutions in the solvent.

  Moreover during the ergodic regime, probed by DLS, the slow relaxation time increases exponentially with t_w ($\tau_2 \propto \exp(t_w)$) until τ_2 becomes comparable to t_w.

  Subsequently, after ergodicity breaking, XPCS data shows that τ_2 changes regime and evolves linearly with t_w ($\tau_2 \propto t_w$).

  In addition, when the non-ergodic regime is reached, differently from τ_1, XPCS data revealed that the slow relaxation time changed its Q-dependence to $\tau_2 \propto Q^{-1}$. The fact that τ_2 changes its Q dependence from Q^{-2} to Q^{-1} reflects the transition from the approximately diffusive Brownian motion to a reduced mobility of the particles.

- **The stretching parameter β and mean relaxation time τ_m (DLS and XPCS)**

  The stretching parameter β has been found to be independent of Q for all samples during the whole aging (ergodic and non-ergodic regimes) probed by DLS and XPCS.

  This parameter depends only on waiting time, decaying linearly with t_w during the ergodic regime and remaining practically unchanged during the non-ergodic regime.

Following the same trend as τ_2 the main relaxation time was found to scale as $\tau_m \propto Q^{-2.1}$ and to increases exponentially with t_w ($\tau_m \propto \exp(t_w)$) during the ergodic regime probed by DLS. After the ergodicity breaking, since the β parameter remained practically unchanged, XPCS results presented the same phenomenology of τ_2, changing its Q dependency to Q^{-1} and evolving linearly with waiting time $\tau_m \propto t_w$.

- **The divergence t_w^∞ and B parameters (DLS)**

  The divergence waiting time t_w^∞ (time at which the system reaches the arrested state) and B (that describes how the system reaches the arrested state) parameters presented no Q-dependence for all clay concentrations and different solvents. These parameters have been found to depend only with clay concentration being t_w^∞ very sensitive to isotopic substitution in the solvent.

- **Same phenomenology of the dynamic and static properties for isotopic substitution in the solvent.**

  The experimental results observed during this work, permit to elucidate that H/D isotopic substitution plays an important role on the aging velocity during the ergodic regime, preserving the same physical properties and arresting mechanisms present in Laponite in H_2O.

  - **The divergence waiting time t_w^∞ (DLS)**

    Although the aging behavior is qualitatively similar, the dynamics of the system is slower in D_2O compared to H_2O. This is evident by the divergence waiting time t_w^∞ that is strongly affected by H/D isotopic substitution and is increased for D_2O solvents.

  - **The B parameter (DLS)**

    The B parameter presents a discontinuity (step behavior) between two different constant values at low and high clay concentrations, for both H_2O and D_2O, so that a scaling law of the slow relaxation parameters is found, with all the curves collapsing on two distinct master curves, one for low and another for high concentrations. This result, already found in Laponite water suspensions, indicates the existence, also in the case of D_2O, of two different routes to reach the arrested state. In fact H/D isotopic substitution determines only a slight shift of the discontinuity of B towards high clay concentrations. These results permit to speculate that, as for H_2O, also in the case of D_2O two different arrested states at low and high concentrations can be found.

  - **The static structure factor $S(Q)$ (SAXS)**

    SAXS measurements have confirmed the previous hypothesis and the evolution of the static structure factor ($S(Q)$) with waiting time has clarified that a **gel** at low and a **glass** at high Laponite concentrations in D_2O can be recognized. Moreover a comparison of the $S(Q)$ of samples in H_2O and D_2O solutions shows similar behaviors both at low and high concentrations, even if a comparison with the static structure factor

obtained with theory and simulations is necessary to verify and understand if and what modifications are introduced by isotopic substitution in the interaction potential.

Bibliography

[1] International union of pure and applied chemistry, Jul 2012.

[2] J.D. Shaw. *Introduction to Colloid and Surface Chemistry, 4^{th} Ed.* Butterworth Heinemann, 1992.

[3] T. Cosgrove. *Colloid Science: Principles, Methods and Applications.* Blackwell Publishing, 2005.

[4] S. Simovic, T.J. Barnes, A. Tan, and C.A. Prestidge. Assembling nanoparticle coatings to improve the drug delivery performance of lipid based colloids. *Nanoscale*, 4:1220–1230, 2012.

[5] G.M. Pajonk. Transparent silica aerogels. *J. Non-Cryst. Solids*, 225:307–314, 1998.

[6] M.C.D. Mourad, D.V. Byelov, A.V. Petukhov, D.A.M. Winter, A.J. Verkleij, and H.N.W. Lekkerkerker. Sol-gel transitions and liquid crystal phase transitions in concentrated aqueous suspensions of colloidal gibbsite platelets. *J. Phys. Chem. B*, 113:11604–11613, 2009.

[7] M.C.D. Mourad, A.V. Petukhov, G.J. Vroege, and H.N.W. Lekkerkerker. Lyotropic hexagonal columnar liquid crystals of large colloidal gibbsite platelets. *Langmuir*, 26:14182–14187, 2010.

[8] A.C.V. Coelho and P.S. Santos. Argilas especiais: O que são, caracterização e propriedades. *Quim. Nova*, 30:146–152, 2007.

[9] E. Balnois, S. Durand-Vidal, and P. Levitz. Probing the morphology of laponite clay colloids by atomic force microscopy. *Langmuir*, 19:6633, 2003.

[10] A. Mourchid, A. Delville, J. Lambard, E. Lécolier, , and P. Levitz. Phase diagram of colloidal dispersions of anisotropic charged particles: Equilibrium properties, structure, and rheology of laponite suspensions. *Langmuir*, 11:1942–1950, 1995.

[11] P. Levitz, E. Lecolier, A. Mourchid, A. Delville, and S. Lyonnard. Liquid-solid transition of laponite suspensions at very low ionic strength: Long-range electrostatic stabilisation of anisotropic colloids. *Europhys. Lett.*, 49:672–677, 2000.

[12] P. Mongondry, J.F. Tassin, and T. Nicolai. Revised state diagram of laponite dispersions. *J. Colloid Interf. Sci.*, 283:397–405, 2005.

[13] H. Tanaka, J. Meunier, and D. Bonn. Nonergodic states of charged colloidal suspensions: Repulsive and attractive glasses and gels. *Phys. Rev. E*, 69:31404, 2004.

[14] B. Ruzicka and E. Zaccarelli. A fresh look at the laponite phase diagram. *Soft Matter*, 7:1268–1286, 2011.

[15] B. Ruzicka, L. Zulian, E. Zaccarelli, R. Angelini, M. Sztucki, A. Moussaid, and G. Ruocco. Competing interactions in arrested states of colloidal clays. *Phys. Rev. Lett.*, 104:085701, 2010.

[16] B. Ruzicka, E. Zaccarelli, L. Zulian, R. Angelini, M. Sztucki, A. Moussaid, T. Narayanan, and F. Sciortino. Observation of empty liquids and equilibrium gels in a colloidal clay. *Nat. Materials*, 10:56–60, 2011.

[17] S.C. Glotzer and M.J. Solomon. Anisotropy of building blocks and their assembly into complex structures. *Nat. Materials*, 6:557–562, 2007.

[18] *Laponite - synthetic layered silicate - its chemistry, structure and relationship to natural clays.* Laponite technical bulletin, 2003. L204/01g, www.laponite.com.

[19] S.L. Tawari, D.L. Kochi, and C. Cohen. Electrical double-layer effects on the brownian diffusivity and aggregation rate of laponite clay particles. *J. Colloid Interf. Sci.*, 240:54–66, 2001.

[20] S. Jabbari-Farouji, H. Tanaka, G.H. Wegdam, and D. Bonn. Multiple nonergodic disordered states in laponite suspensions: A phase diagram. *Phys. Rev. E*, 78:061405, 2008.

[21] C. Martin, F. Pignon, J.-M. Piau, A. Magnin, P. Lindner, and B. Cabane. Dissociation of thixotropic clay gels. *Phys. Rev. E*, 66:02140l, 2002.

[22] H.Z. Cummins. Liquid, glass, gel: The phases of colloidal laponite. *J. Non-Cryst. Solids*, 253:3891–3905, 2007.

[23] H.C. Hamaker. The london-van der waals attraction between spherical particles. *Physica*, 4:1058–1072, 1937.

[24] R. J. Hunter. *Foundation of Colloid Science, Vol. I.* Clarendon Press, Oxford, 1986.

[25] W.B. Russel, D.A. Saville, and W.R. Schowalter. *Colloidal Dispersions.* Cambridge University Press, Cambridge, 1989.

[26] J.N. Israelachvili. van der waals dispersion force contribution to works of adhesion and contact angles on the basis of macroscopic theory. *J. Chem. Soc. Faraday Trans. II*, 69:1729, 1973.

[27] A.L. Loeb, J.Th.G. Overbeek, and P.H. Wiersema. *The electrical double layer around a spherical particle.* M.I.T. Press, Cambridge, Mass., 1961.

[28] O.Z. Stern. *Electrochemistry*, 30:508, 1924.

[29] R.B. Secor and J. Radke. Spillover of the diffuse double layer on montmorillonite particles. *J. Colloid Interf. Sci.*, 103:237–244, 1985.

[30] W. Sun, Y. Yang, T. Wang, H. Huang, X. Liu, and Z. Tong. Effect of adsorbed poly(ethylene glycol) on the gelation evolution of laponite suspensions: Aging time-polymer concentration superposition. *J. Colloid Interf. Sci.*, 376:76–82, 2012.

[31] S. Levine. Problems of stability in hydrophobic colloidal solutions i. on the interaction of two colloidal metallic particles. general discussion and applications. *P. R. Soc. London*, 170:145–165, 1939.

[32] S. Levine and G.P. Dube. Interaction between two hydrophobic colloidal particles, using the approximate debye-huckel theory. *T. Faraday Soc.*, 35:1125–1141, 1940.

[33] B. Derjaguin and L. Landau. Theory of the stability of strongly charged lyophobic sols and of the adhesion of strongly charged particles in solutions of electrolytes. *Acta PhysicoChim. URS*, 14:633, 1941.

[34] E.J.W. Verwey and J.Th.G. Overbeek. *Theory of the Stability of Lyophobic Colloids*. Elsevier, Amsterdam, 1948.

[35] R.J.F. Leote De Carvalho, E. Trizac, and J.-P. Hansen. Non-linear poisson-boltzmann theory for swollen clays. *Europhys. Lett.*, 43:369–375, 1998.

[36] D.G. Rowan, J.-P. Hansen, and E. Trizac. Screened electrostatic interactions between clay platelets. *Mol. Phys.*, 98:1369–1378, 2000.

[37] E. Trizac, L. Bocquet, R. Agra, J.-J. Weis, and M. Aubouy. Effective interactions and phase behaviour for a model clay suspension in an electrolyte. *J. Phys-Condens. Mat.*, 14:9339–9352, 2002.

[38] M. Dijkstra, J.-P. Hansen, and P.A. Madden. Gelation of a clay colloid suspension. *Phys. Rev. Lett.*, 75:2236, 1995.

[39] M. Dijkstra, J.-P. Hansen, and P.A. Madden. Statistical model for the structure and gelation of smectite clay suspensions. *Phys. Rev. E*, 55:3044–3053, 1997.

[40] S. Kutter, J.-P. Hansen, M. Sprik, and E. Boek. Structure and phase behavior of a model clay dispersion: A molecular-dynamics investigation. *J. Chem. Phys.*, 112:311–322, 2000.

[41] G. Odriozola, M. Romero-Bastida, and F.D.J. Guevara-Rodriguez. Brownian dynamics simulations of laponite colloid suspensions. *Phys. Rev. E*, 70(2):021405, 2004.

[42] B. Jonsson, C. Labbez, and B. Cabane. Interaction of nanometric clay platelets. *Langmuir*, 24:11406–11413, 2008.

[43] A.J. Liu and S.D. Nagel. Jamming is not just cool any more. *Nature*, 21:396, 1998.

[44] V. Trappe, V. Prasad, L. Cipelletti, P.N. Segre, and D.A. Weitz. Jamming phase diagram for attractive particles. *Nature*, 411:772, 2001.

[45] B.V. Derjaguin and L.D. Landau. *Acta Physicochem. USSR*, 14:633, 1941.

[46] E. Leutheuser. Dynamical model of the liquid-glass transition. *Phys.Rev. A*, 29:2765, 1984.

[47] W. Götze. *Liquids, freezing and glass transition.* North Holland, Amsterdam, 1991.

[48] W. Götze and L. Sjögren. β relaxation at the glass transition of hard sphere colloids. *Phys. Rev. A*, 43:5442, 1991.

[49] P.N. Pusey and W. Van Megen. Dynamic light scattering by non-ergodic media. *Physica A*, 157:705–741, 1989.

[50] A. Shahin and Y. Jashi. Irreversible aging dynamics and generic phase behavior of aqueous suspensions of laponite. *Langmuir*, 26:4219, 2010.

[51] E. Zaccarelli, S. Andreev, F. Sciortino, and D.R. Reichman. Numerical investigation of glassy dynamics in low density systems. *Phys. Rev. Lett.*, 100:195701, 2008.

[52] E. Zaccarelli. Colloidal gels: equilibrium and non-equilibrium routes. *J. Phys-Condens. Mat.*, 19:323101, 2007.

[53] A. Mourchid, E. Lécolier, H. Van Damme, and P. Levitz. On viscoelastic, birefringent, and swelling properties of laponite clay suspensions: Revisited phase diagram. *Langmuir*, 14:4718–4723, 1998.

[54] B. Ruzicka, L. Zulian, and G. Ruocco. Routes to gelation in a clay suspension. *Phys. Rev. Lett.*, 93:258301, 2004.

[55] J.-C.P. Gabriel, C. Sanchez, and P. Davidson. Observation of nematic liquid-crystal textures in aqueous gels of smectite clays. *J. Phys. Chem.*, 100:11139–11143, 1996.

[56] B.J. Lemaire, P. Panine, J.-C.P. Gabriel, and P. Davidson. The measurement by saxs of the nematic order parameter of laponite gels. *Europhys. Lett.*, 59:55–61, 2002.

[57] M. Kroon, W. G. Wegdam, and R. Sprik. Dynamic light scattering studies on the sol-gel transition of a suspension of anisotropic colloidal particles. *Phys. Rev. E*, 54:6541, 1996.

[58] D. Bonn, H. Tanaka, G. Wegdam, H. Kellay, and J. Meunier. Laponite: What is difference between gel and a glass? *Europhys. Lett.*, 45:52–57, 1999.

[59] J.C.F. Toledano, F. Sciortino, and E. Zaccarelli. Colloidal systems with competing interactions: from an arrested repulsive cluster phase to a gel. *Soft Matter*, 5:2390–2398, 2009.

[60] C.L. Klix, C.P. Royall, and H. Tanaka. Structural and dynamical features of multiple metastable glassy states in a colloidal system with competing interactions. *Phys. Rev. Lett.*, 104:165702, 2010.

[61] T. Nicolai and S. Cocard. Dynamic light-scattering study of aggregating and gelling colloidal disks. *J. Colloid Interf. Sci.*, 244:51–57, 2001.

[62] T. Nicolai and S. Cocard. Structure of gels and aggregates of disk-like colloids. *Eur. Phys. J. E*, 5:221–227, 2001.

[63] T. Nicolai and S. Cocard. Light scattering study of the dispersion of laponite. *Langmuir*, 16:8189–8193, 2000.

[64] B. Ruzicka, L. Zulian, and G. Ruocco. Ageing dynamics in laponite dispersions at various salt concentrations. *Phylosophycal Magazine*, 87:449–458, 2007.

[65] B. Ruzicka, L. Zulian, and G. Ruocco. More on the phase diagram of laponite. *Langmuir*, 22:1106–1111, 2006.

[66] H. van Olphen. *An Introduction to Clay Colloid Chemistry.* Interscience, London, 1977.

[67] S. Jabbari-Farouji, G.H. Wegdam, and D. Bonn. Gels and glasses in a single system: Evidence for an intricate free-energy landscape of glassy materials. *Phys. Rev. Lett.*, 99:065701, 2007.

[68] B. Ruzicka, L. Zulian, R. Angelini, M. Sztucki, A. Moussaid, and G. Ruocco. Arrested state of clay-water suspensions: Gel or glass? *Phys. Rev. E*, 77:020402, 2008.

[69] B.J. Berne and R. Pecora. *Dynamic light scattering.* Wiley, New York, 1976.

[70] P. Pusey. *Introduction to Scattering Experiments.* Elsevier Sciences B.V., 2002. in Neutrons, X-rays and Light: Scattering methods applied to Soft Condensed Matter, P. Lindner and T. Zemb eds.

[71] P. Pusey. Plenum Press, New York, 1977. In Photon Correlation Spectroscopy and Velocimetry, H. Z. Cummins and E. R. Pike eds.

[72] V. Degiorgio, R. Piazza, M. Corti, and J. Stavans. Dynamic light scattering study of concentrated dispersions of anisotropic spherical colloids. *J. Chem. Soc. Faraday Trans.*, 87(3):431–434, 1991.

[73] V. Degiorgio, R. Piazza, and R.B. Jonesi. Rotational diffusion in concentrated colloidal dispersions of hard spheres. *Phys. Rev. E*, 52:2707–2717, 1995.

[74] D. Kleshchanok, M. Heinen, G. Nagele, and P. Holmqvist. Dynamics of charged gibbsite platelets in the isotropic phase. *Soft Matter*, 8:1584–1592, 2012.

[75] F. Ianni, R. Di Leonardo, S. Gentilini, and G. Ruocco. Aging after shear rejuvenation in a soft glassy colloidal suspension: Evidence for two different regimes. *Phys. Rev. E*, 75:011408, 2007.

[76] O. Czakkel and A. Madsen. Evolution of dynamics and structure during formation of a cross-linked polymer gel. *Europhys Lett.*, 95:28001, 2011.

[77] A. Madsen, R.L. Leheny, H. Guo, M. Sprung, and O. Czakkel. Beyond simple exponential correlation functions and equilibrium dynamics in x-ray photon correlation spectroscopy. *New J. Phys.*, 12:055001, 2010.

[78] R. Bandyopadhyay, D. Liang, J.L. Harden, and R.L. Leheny. Slow dynamics, aging, and glassy rheology in soft and living matter. *Solid State Commun.*, 139:589–598, 2006.

[79] F. Mezei. *The Principles of Neutron Spin Echo*. Springer, Heidelberg, 1980. in Neutron Spin Echo: Proceedings of a Laue -Langevin Institut Workshop.

[80] A. Guinier and G. Fournet. *Small Angle Scattering of X-rays*. Wiley, New York, 1955.

[81] G. Porod. *Small Angle X-rays Scattering*. Ed. O.G.O. Kratky, Academic Press, London, 1982.

[82] P. Debye and A.M. Bueche. Scattering by an inhomogeneous solid. *J. Appl. Phys.*, 20:518, 1949.

[83] L.A. Feigin and D.I. Svergun. *Structure Analysis by Small Angle X-ray Scattering and Neutron Scattering*. Plenum Press, New York, 1987.

[84] A. Mourchid and P. Levitz. Long-term gelation of laponite aqueous dispersions. *Phys. Rev. E*, 57:4887, 1998.

[85] D.W. Thompson and J.T. Butterworth. The nature of laponite and its aqueous dispersions. *J. Colloid Interface Sci.*, 151:236, 1992.

[86] J.-P. Bouchaud, L.F. Cugliandolo, J. Kurchan, and M. Mezard. *Out of Equilibrium Dynamics in Spin-glasses and Other Glassy Systems*. World Scientific, London, 1998. in Spin Glasses and Random Fields, Vol. 12.

[87] B. Ruzicka, L. Zulian, and G. Ruocco. Ergodic to non-ergodic transition in low concentration laponite. *J. Phys-Condens. Mat.*, 16:S4993, 2004.

[88] B. Abou, D. Bonn, and J. Meunier. Aging dynamics in a colloidal glass. *Phys. Rev. E*, 64:021510, 2001.

[89] A. Knaebel, J.-P. Bellour, V. Munch, V. Viasnoff, F. Lequeux, and L. Harden. Aging behavior of laponite clay particle suspensions. *Europhys. Lett.*, 52:73–79, 2000.

[90] F. Schosseler, S. Kaloun, M. Skouri, and J.P. Munch. Diagram of the aging dynamics in laponite suspensions at low ionic strength. *Phys. Rev. E*, 73:021401, 2006.

[91] R.K. Pujala and H.B. Bohidar. Ergodicity breaking and aging dynamics in laponite-montmorillonite mixed clay dispersions. *Soft Matter*, 8:6120–6127, 2012.

[92] M. Watzlawek and G. Nagele. Self-diffusion coefficients of charged particles: Prediction of nonlinear volume fraction dependence. *Phys. Rev. E*, 56:1258–1261, 1997.

[93] J. Bergenholtz, F.M. Horn, W. Richtering, N. Willenbacher, and N.J. Wagner. Relationship between short-time self-diffusion and high-frequency viscosity in charge-stabilized dispersions. *Phys. Rev. E*, 58:R4088–R4091, 1998.

[94] G. Grubel, A. Madsen, and A. Robert. *X-Ray Photon Correlation Spectroscopy (XPCS).* Springer, 2008. in Soft-Matter Characterization.

[95] H. Tanaka, S.J. Farouji, J. Meunier, and D. Bonn. Kinetics of ergodic-to-nonergodic transitions in charged colloidal suspensions: Aging and gelation. *Phys. Rev. E*, 71:021402, 2005.

[96] M. Bellour, A. Knaebel, J.L. Harden, F. Lequeux, and J.-P. Munch. Aging processes and scale dependence in soft glassy colloidal suspensions. *Phys. Rev. E*, 67:031405, 2003.

[97] R. Bandyopadhyay, D. Liang, H. Yardimci, D.A. Sessoms, M.A. Borthwick, G.J. Mochrie, J.L. Harden, and R.L. Leheny. Evolution of particle-scale dynamics in an aging clay suspension. *Phys. Rev. Lett.*, 93:228302, 2004.

[98] B. Farago. Recent neutron spin-echo developments at the ill (in11 and in15). *Physica B*, 268:270–276, 1999.

[99] I. Sikharulidze, B. Farago, I.P. Dolbnya, A. Madsen, and W.H. deJeu. Surface and bulk elasticity determined fluctuation regimes in smectic membranes. *Phys. Rev. Lett*, 91:165504, 2003.

[100] B. Farago. Neutron spin echo study of well organized soft matter systems. *Physica B*, 386:688–691, 2006.

[101] B. Farago, J. Li, G. Cornilescu, D.J.E. Callaway, and Z. Bu. Activation of nanoscale allosteric protein domain motion revealed by neutron spin echo spectroscopy. *Biophyis. J.*, 99:3473–3482, 2010.

[102] O. Spalla. *General Theorems in Small-Angle Scattering.* Elsevier Sciences B.V., 2002. in Neutrons, X-rays and Light: Scattering Methods Applied to Soft Condensed Matter.

[103] A. Guinier and G. Fournet. *Small Angle Scattering of X-rays.* Wiley, New York, 1955.

[104] L.A. Feigin and D.I. Svergun. *Structure Analysis by Small-Angle X-ray Scattering and Neutron Scattering.* Plenum Press, New York, 1987.